

Syracuse University

**SURFACE**

---

Dissertations - ALL

SURFACE

---

December 2020

## **SPECTROSCOPIC STUDY OF ICES WITH ASTROPHYSICAL INTEREST**

Shahnewaz M. Emtiaz  
*Syracuse University*

Follow this and additional works at: <https://surface.syr.edu/etd>



Part of the [Physical Sciences and Mathematics Commons](#)

---

### **Recommended Citation**

Emtiaz, Shahnewaz M., "SPECTROSCOPIC STUDY OF ICES WITH ASTROPHYSICAL INTEREST" (2020).  
*Dissertations - ALL*. 1208.  
<https://surface.syr.edu/etd/1208>

This Dissertation is brought to you for free and open access by the SURFACE at SURFACE. It has been accepted for inclusion in Dissertations - ALL by an authorized administrator of SURFACE. For more information, please contact [surface@syr.edu](mailto:surface@syr.edu).

## ABSTRACT

In this thesis, I investigate the physical and chemical processes of simulated cosmic dust grains and planetary surface analogues in laboratory experiments performed at the Syracuse University Astrophysics and Surface Science Laboratory. I have studied the mid-infrared (Mid-IR) bands of thin films of pure CH<sub>4</sub> ices and of CH<sub>4</sub> ices mixed with N<sub>2</sub> and H<sub>2</sub>O in order to characterize the thermal evolution of ices in confined geometry and to improve the understanding of observations of ices present in interstellar space and in outer solar system bodies. Furthermore, I studied the self-diffusion of CO<sub>2</sub> isotopes in different thin-film arrangements. Mid-IR laboratory data of the morphological change of CH<sub>4</sub>, CH<sub>4</sub>-volatile mixture, and CO<sub>2</sub> during thermal processing will become a crucial component to analyze the data of James Webb Space Telescope (JWST) that is scheduled to be launched in 2021. The experimental data presented in Chapter 3, 4, and 5 fill the void of the experimental data on CH<sub>4</sub> ice to successfully interpret the remote sensing data obtained from spacecraft and ground-based observations. The study of diffusion of isotopes of CO<sub>2</sub> using IR features due to resonant coupling in the solid is presented in Chapter 6. It is the first experimental study of self-diffusion in CO<sub>2</sub> thin films and also the first study of using this method in thin films.

# **SPECTROSCOPIC STUDY OF ICES WITH ASTROPHYSICAL INTEREST**

By

**Shahnewaz M. Emtiaz**

M.S., Dhaka University 2011

B.S, Dhaka University 2009

DISSERTATION

SUBMITTED IN PARTIAL FULFILLMENT OF THE REQUIREMENTS

FOR THE DEGREE OF

DOCTOR OF PHILOSOPHY IN PHYSICS

Syracuse University

December 2020

Copyright © 2020 Shahnewaz M. Emtiaz  
All rights reserved.

## **ACKNOWLEDGEMENTS**

I would like to thank my Advisor, Gianfranco Vidali, for his consistent support, mentorship, and guidance throughout my Ph.D. study. He provided me with a remarkable learning opportunity for which I am ever grateful to him.

I would also like to all my previous and current lab partners, Jiao He, Francis Toriello, Tyler Hopkins, and under-graduate members, with whom I had the pleasure to work with on some of the most rewarding and exciting subject matter of my career thus far.

I am grateful to the committee members for assigning their valuable time for my Ph.D. oral defense. I also wish to convey my sincere gratitude to the committee members, Catherine A Cornwell, Gianfranco Vidali, Jennifer L Ross, Britton Plourde, Mitchell Soderberg, and Jiao He for taking the time to read the draft carefully and suggesting improvements.

Finally, I would like to thank my parents for always believing in me. I am indebted to my wife, Shahnaj Parvin, and my two little daughters, Sarah and Amira, for their love and sacrifice during my Ph.D. study.

# Contents

<b>List of Tables</b>	<b>viii</b>
<b>List of Figures</b>	<b>xiii</b>
<b>Preface</b>	<b>xiv</b>
<b>1 Introduction</b>	<b>1</b>
1.1 Background . . . . .	1
1.2 Interstellar Medium . . . . .	2
1.3 Ices in Space . . . . .	3
1.3.1 Interstellar dust . . . . .	3
1.3.2 Interstellar ice evolution . . . . .	3
1.3.3 Interstellar ice formation mechanisms . . . . .	5
1.3.4 Solar system ices . . . . .	7
1.4 Laboratory Simulation of Space Ices . . . . .	7
1.5 Thesis Outline . . . . .	9
<b>2 Experimental Setup</b>	<b>11</b>
2.1 General . . . . .	11
2.2 Main Chamber . . . . .	11
2.2.1 Cryocooler installation . . . . .	14
2.2.2 Sample and radiation shield . . . . .	14
2.3 Molecular Beamline . . . . .	15
2.4 Infrared Spectroscopy . . . . .	16
2.5 Fourier Transform Infrared Spectroscopy (FTIR) Setup . . . . .	17
2.6 Deposition of Gases . . . . .	18
2.7 Thermal Processing of Ice . . . . .	20

<b>3</b>	<b>Infrared Spectroscopic Study of Solid Methane: Nuclear Spin Conversion of Stable and Metastable Phases</b>	<b>21</b>
3.1	Abstract . . . . .	21
3.2	Introduction . . . . .	22
3.3	Experimental methods . . . . .	25
3.4	Results and Analysis . . . . .	26
3.4.1	FTIR absorption spectra of $\nu_3$ and $\nu_4$ modes . . . . .	28
3.4.2	The $\nu_3$ mode of methane ice grown at 6 K and 30 K . . . . .	31
3.4.3	Phase change from $II^*$ to $II$ . . . . .	31
3.4.4	Calculation of the Nuclear Spin Conversion (NSC) rate . . . . .	33
3.5	Summary . . . . .	34
<b>4</b>	<b>Infrared Spectroscopic Study of Crystalline Methane Solid and Methane Mixture with Polar and Non-polar Molecules</b>	<b>38</b>
4.1	Abstract . . . . .	38
4.2	Introduction . . . . .	39
4.3	Experimental Methods . . . . .	40
4.4	Results and Analysis . . . . .	40
4.4.1	Methane crystalline phases and deposition temperature . . . . .	42
4.4.2	Effect of thickness of $CH_4$ thin film on phase transition . . . . .	42
4.4.3	Effect on NSC of methane ice prepared with two different deposition methods . . . . .	44
4.4.4	Methane and water ice mixture with different ratios . . . . .	44
4.4.5	Segregation of water in $CH_4:H_2O$ ice matrix . . . . .	48
4.4.6	NSC in partially segregated $CH_4:H_2O$ ice mixture . . . . .	51
4.4.7	Methane and nitrogen ice mixtures with different ratios . . . . .	51
4.4.8	Diffusion of molecules in methane and nitrogen ice mixtures . . . . .	54
4.5	Astrophysical Implications . . . . .	54
4.6	Summary . . . . .	56
<b>5</b>	<b>Temperature Evolution of <math>CH_4 : N_2</math> Ice Mixture - an Application to trans-Neptunian Objects</b>	<b>58</b>
5.1	Abstract . . . . .	58
5.2	Introduction . . . . .	59
5.3	Experimental Methods . . . . .	61

5.4	Results and Analysis	62
5.4.1	Comparison between CH <sub>4</sub> and CH <sub>4</sub> : N <sub>2</sub> IR spectra	62
5.4.2	Diffusion of molecules in CH <sub>4</sub> and N <sub>2</sub> ice matrix	62
5.4.3	Diffusion of CH <sub>4</sub> and N <sub>2</sub> molecules in N <sub>2</sub> dominated ice matrix	64
5.4.4	2 <sup>nd</sup> transformation in CH <sub>4</sub> and N <sub>2</sub> ice matrix	65
5.4.5	Dependence of the 1 <sup>st</sup> transformation on the mixing ratio	68
5.4.6	Dependence of the 1 <sup>st</sup> transformation on ice thickness	68
5.4.7	Activation energy of the 1 <sup>st</sup> transformation	71
5.5	Summary	74
<b>6</b>	<b>Self-diffusion in <sup>12</sup>CO<sub>2</sub> and <sup>13</sup>CO<sub>2</sub> Thin Films</b>	<b>75</b>
6.1	Abstract	75
6.2	Introduction	76
6.3	Background Work	76
6.4	Experimental Methods	77
6.5	Results and Analysis	77
6.5.1	Self diffusion in layered ice	78
6.5.2	Slow heating up of <sup>12</sup> CO <sub>2</sub> and <sup>13</sup> CO <sub>2</sub> mixture	80
6.5.3	Temperature dependence of CO <sub>2</sub> diffusion	80
6.5.4	Dependence of CO <sub>2</sub> diffusion on the underlying surface	82
6.6	Discussion	83
6.7	Summary	84
<b>7</b>	<b>Conclusions</b>	<b>85</b>
7.1	Infrared Spectroscopic Study of Solid Methane: Nuclear Spin Conversion of Stable and Metastable Phases (Chapter 3)	85
7.2	Infrared Spectroscopic Study of Crystalline Methane Solid and Methane Mixture with Polar and Non-polar Molecules (Chapter 4)	85
7.3	Temperature Evolution of CH <sub>4</sub> :N <sub>2</sub> Ice Mixture - an Application to trans-Neptunian Objects (Chapter 5)	85
7.4	Self Diffusion in <sup>12</sup> CO <sub>2</sub> and <sup>13</sup> CO <sub>2</sub> Thin Film (Chapter 6)	86
	<b>Bibliography</b>	<b>97</b>

# List of Tables

1	Ice abundances with respect to H <sub>2</sub> O ice towards young stellar object NGC 7538 IRS 9, high-mass protostar W33A, and Comets; taken from [29] . . . . .	2
2	Parameters in the analysis of the R(0) and R(1) bands . . . . .	33
3	$\nu_4$ and $\nu_3$ band positions, shifts and FWHM of CH <sub>4</sub> :H <sub>2</sub> O with different mixing ratios	48
4	Band positions and shifts of pure methane and CH <sub>4</sub> :H <sub>2</sub> O=95:5 during NSC . . . . .	51
5	Band positions, FWHM and shifts of $\nu_4$ and $\nu_3$ modes of CH <sub>4</sub> :N <sub>2</sub> for various mixing ratios . . . . .	53
6	Data of CH <sub>4</sub> : N <sub>2</sub> ice mixtures in the 1 <sup>st</sup> transformation . . . . .	68

# List of Figures

1	Cartoon representation of the interstellar ice composition starting from the prestellar stage through the collapsing envelop, and into a protoplanetary disk. Adapted from [41, 16] . . . . .	4
2	Cartoon representation of a dust grain and of the main routes of interstellar ice processing that takes place in astrophysical environments; taken from [16] . . . . .	5
3	Comparison between observation and laboratory simulated CH <sub>4</sub> ice and ice mixture (a) $\nu_3$ stretching mode of solid CH <sub>4</sub> observed with ISO SWS (thick line) and KECK/ NIRSPEC (thin line), compared to a number of laboratory ice simulations (smooth gray line).(b) The CH <sub>4</sub> $\nu_4$ bending mode is fitted with the same laboratory ice, without scaling the peak optical depth. Best fits are obtained with H <sub>2</sub> O-rich ices. Note the poor fit of CO-rich ices to the CH <sub>4</sub> stretching mode.; taken from [13]	8
4	A schematics of the main apparatus. . . . .	12
5	Cryocooler schematics. a) 2D diagram with dimensions of the redesigned cryostat system, b) 3D model of the redesigned cryostat. . . . .	13
6	Sample, radiation shield and QMS setup. a) Front view of the sample and radiation shield that thermally isolates the cold part of the cooling column and sample from the UHV chamber. b) Side view of the setup. . . . .	15
7	Side view of experimental apparatus. Details are given in the text; courtesy Francis Toriello's thesis. . . . .	16
8	IR spectra of CO <sub>2</sub> and its vibrational modes. Main panel: IR spectrum of CO <sub>2</sub> showing absorbance maxima associated with varying modes of vibration. The inset figure shows the four theoretically possible vibrational modes of CO <sub>2</sub> : a) asymmetric stretch of CO <sub>2</sub> , b) vertical and horizontal bend, and c) symmetric stretch (st), which lacks change in dipole and consequently has no IR signature. . .	17
9	Optical path of Reflection Absorption InfraRed Spectroscopy (RAIRS) setup. . . .	18
10	A sample thermal processing experiment of CO <sub>2</sub> ice using RAIRS. Inset Figure courtesy Jaio He's thesis. . . . .	20

11	Energy diagram of rotational levels ( $J$ ) in solid $\text{CH}_4$ for different nuclear spin isomers ( $I$ ). Levels of nuclear-spin isomers are shown by bold solid lines. The rotation levels are coupled by the nuclear spin- nuclear spin interaction (connected by solid line) and nuclear spin- rotation interaction. In addition to these intramolecular magnetic interactions, the $J = 2$ and $J = 3$ levels are degenerate with respect to $I$ (outlined inside gray box). Adapted from [56, 82]. . . . .	23
12	FTIR spectra of solid methane in the $\nu_3$ and $\nu_4$ vibrational modes at a resolution of $1.0 \text{ cm}^{-1}$ . All the traces are from the same experiment at different time frames and temperatures. For each panel, the bottom one represents methane solid deposited at 6 K. The middle one shows the spectrum of the deposited methane solid heated to and annealed at 30 K. Finally, the top one represents 30 K annealed methane solid cooled down to 6 K. . . . .	24
13	FTIR spectra of solid methane in the $\nu_3$ and $\nu_4$ vibrational modes at a resolution of $1.0 \text{ cm}^{-1}$ right after deposition at 6 K, 10 K, and 13 K. See text for additional details. . . . .	26
14	Comparison of $\nu_3$ mode of solid methane, deposited at 30 K (left) and at 6 K (right); traces are recorded at 8 K for up to 300 minutes. . . . .	27
15	Illustration of the fitting method used in the analysis. Each absorption feature in the spectrum is fitted with two functions, a Lorentzian and a Gaussian. Out of four fitted curve, the two Lorentzian functions(green and yellow) represent $L_{0\leftarrow 0}$ and $R(0)$ peaks. Two Gaussian functions(blue and red) represent $Q(1)$ and $R(1)$ peaks, respectively. . . . .	27
16	The $\nu_3$ mode during a heating and cooling cycle in the 6 - 12 K temperature range. The three panels show the intensity map (top), the band area of the Gaussian and Lorentzian components (middle), and the temperature ramp (bottom). The horizontal color scale bar on top of the figure shows the relative strength on the 0-0.1 scale in the intensity plot. . . . .	29
17	As in Figure 16, but in the 6 - 30 K temperature range . . . . .	30
18	Temporal change of the integral intensities of $R(0)$ at different temperatures for methane deposited at 30 K. The dotted lines indicate the results of fitting with Eq. 3.1. For clarity's sake $I_\infty$ has been subtracted from each curve. . . . .	32

19	Temperature dependence of the relaxation rates of $R(0)$ and $R(1)$ for ice deposited at 6 K and at 30 K. Main plot: Blue stars and black triangles show the rates for $J = 0(R(0))$ between, respectively, 7.2 K and 8.5 K and between 8.5 K to 11.0 K for solid methane deposited at 6K. The red dots show the rates for solid methane deposited at 30 K. In the inset: green squares and cyan triangles show rates for $J = 1(R(1))$ for solid methane deposited at 30 K. Solid, dashed, and dash-dotted curves show fitting of data using Eq. 3.2 . . . . .	35
20	Temporal change of the integral intensity of $R(0)$ (red) and $R(1)$ (green) at 8 K for solid methane deposited at 30 K. The dotted lines indicate the results of fitted function for $R(0)$ with Eq. 3.1 for $R(0)$ and Eq. 3.4 for $R(1)$ ] . . . . .	36
21	Mid-IR vibrational modes of 100 ML methane ice ( $\nu_3$ (left) and $\nu_3$ (right)) deposited at 7 K, 10 K, 13 K, 16 K, 20 K, 22 K , and 30 K. The traces are displaced vertically for clarity. . . . .	41
22	Slow heating up experiment for 5-30 ML of methane ice deposited at 10 K. This diagram shows the relative temperature range for Phase II to Phase I transition of $\nu_3$ mode for different methane thin film coverage. The absorbance scale is on the right. . . . .	43
23	$\nu_3$ (left) and $\nu_4$ (right) modes of 100 ML of methane solid deposited at 6K. The top two panels show the temporal change of $\text{CH}_4$ ice deposited through a UHV leak valve (deposition from background gas) at a rate of 100 ML/min. The bottom two panels show the temporal change of $\text{CH}_4$ ice deposited through the molecular beamline at a rate of 1 ML/min. . . . .	45
24	$\nu_3$ (left) and $\nu_4$ (right) modes for a $\text{CH}_4:\text{H}_2\text{O}$ mixture with different concentrations. All the mixtures were deposited at 10 K. . . . .	46
25	Segregation of water ( $\text{H}_2\text{O}$ ) in $\text{CH}_4:\text{H}_2\text{O}$ (= 80:20) mixture for a cyclic heating up experiment in the temperature range of 10 to 30 K. The dotted IR trace represents the ice deposited at 10 K, while the solid black line is for the ice after it has undergone one round of heat cycling (from 10K to 30K and back down to 10K). . . . .	47
26	Temporal change of Nuclear Spin Conversion of solid methane at 7 K. The ice was prepared at 10 K (blue line), heated to 30 K, and rapidly cooled back down to 7 K (black line) to track the NSC for $\nu_3$ and $\nu_4$ vibrational modes over a time of 100 min. . . . .	49

27	Temporal change of Nuclear Spin Conversion of CH <sub>4</sub> :H <sub>2</sub> O (= 95:5) mixture at 7 K. The ice was prepared at 10 K, heated to 30 K, and rapidly cool back down to 7 K to track the NSC for $\nu_3$ and $\nu_4$ vibrational modes over a time period of 30 min. The top two panels show the temporal change at 7 K after cooling down from 30 K and the bottom two panels show the temporal change over 30 min. of ice deposited as 10 K . . . . .	50
28	FTIR spectra of solid methane in the $\nu_3$ and $\nu_4$ vibrational modes for CH <sub>4</sub> :N <sub>2</sub> mixture for various concentration at a resolution of 1.0 cm <sup>-1</sup> . All the mixtures were deposited at 10 K. This figure represents how the increase of N <sub>2</sub> in CH <sub>4</sub> :N <sub>2</sub> ice matrix distort the molecular symmetry of $\nu_4$ and $\nu_3$ mode of solid methane . . . . .	52
29	Diffusion process of N <sub>2</sub> in CH <sub>4</sub> :N <sub>2</sub> (= 80:20) mixture in a cyclic heating experiment in a temperature range of 10 to 20 K. The blue dotted line shape represents the ice mixture upon deposition and solid black line represents the ice that is taken to 20 K and then cooled back to 10 K. . . . .	55
30	IR spectra of $\nu_4$ (left) and $\nu_3$ (right) modes of 100 ML of pure methane (top) and CH <sub>4</sub> :N <sub>2</sub> = 80:20 (bottom) mixture in a temperature range of 10 to 20 K. The blue dotted line shape represents the ice mixture upon deposition and solid black line represents the heated up ice at 20 K. . . . .	63
31	IR Intensity map of $\nu_4$ (top) and $\nu_3$ (bottom) modes of 100 ML CH <sub>4</sub> :N <sub>2</sub> = 20:80 mixture for a slow heating up experiment between 10 and 40 K. . . . .	64
32	IR Intensity map of $\nu_4$ (top) and $\nu_3$ (bottom) modes of 100 ML CH <sub>4</sub> :N <sub>2</sub> = 20:80 mixture for a slow heating up experiment between 6 and 40 K. . . . .	65
33	IR intensity map of $\nu_3$ mode for the 1 <sup>st</sup> transformation of a CH <sub>4</sub> :N <sub>2</sub> mixture with different mixing ratios . . . . .	66
34	Fitting of the temperature of the 1 <sup>st</sup> transformation of CH <sub>4</sub> and N <sub>2</sub> mixture with different mixing ratios with a quadratic equation. Error bars represent uncertainties in establishing the transition temperature and the fraction of N <sub>2</sub> . . . . .	67
35	IR intensity map of the $\nu_3$ mode for 1 <sup>st</sup> transformation of a CH <sub>4</sub> and N <sub>2</sub> mixture with different film thickness . . . . .	69
36	Fitting of the 1 <sup>st</sup> transformation of CH <sub>4</sub> and N <sub>2</sub> mixture with different mixing ratios with an exponential decay curve. . . . .	70
37	Fitting scheme of $\nu_3$ mode in the isothermal experiment with a CH <sub>4</sub> :N <sub>2</sub> 70:30 mixture. . . . .	71

38	Temporal change of $\nu_3$ mode peak position for 16.4 K isothermal experiment. The blue dots represent the data and the broken red line represents the fitting function. . . . .	72
39	Arrhenius type plot for calculating the activation energy of 1 <sup>st</sup> transformation of a CH <sub>4</sub> and N <sub>2</sub> = 70:30 mixture. . . . .	73
40	Slow heating up experiment of 22 ML of <sup>12</sup> CO <sub>2</sub> / <sup>13</sup> CO <sub>2</sub> / <sup>12</sup> CO <sub>2</sub> (10 ML/2 ML/10 ML) layer/sandwich structured ice deposited at 10 K. The plot shows the morphological change and formation of several peaks (LO, TO, M, and S) of <sup>12</sup> CO <sub>2</sub> and <sup>13</sup> CO <sub>2</sub> . The inset shows IR traces of 20 ML <sup>12</sup> CO <sub>2</sub> deposited at 10 K and 30 K. . . . .	78
41	Slow heating up experiment of 100 ML of <sup>12</sup> CO <sub>2</sub> : <sup>13</sup> CO <sub>2</sub> =95:5 mixture ice deposited at 10 K. This plot shows the change of <sup>12</sup> CO <sub>2</sub> and <sup>13</sup> CO <sub>2</sub> asymmetrical stretching $\nu_3$ mode with rising temperature. The inset diagram shows the IR traces of 20 ML <sup>12</sup> CO <sub>2</sub> deposited at 10 K and 30 K. . . . .	79
42	Comparison of slow deposition experiment for 0.5, 1.0 ,and 5.0 ML <sup>13</sup> CO <sub>2</sub> deposited on top of 20 ML <sup>12</sup> CO <sub>2</sub> ice at 10 K (left panels) and 30 K (right panels). In both cases 20 ML <sup>12</sup> CO <sub>2</sub> ice was deposited at 10 K, heated up and annealed at 65 K for 30 min, and cooled back down to respective temperature before <sup>13</sup> CO <sub>2</sub> deposition. . . . .	81
43	Comparison of slow heating up experiment for 1 ML <sup>13</sup> CO <sub>2</sub> deposited at 10 K (left) and 30 K (right) on top of 20 ML <sup>12</sup> CO <sub>2</sub> ice as shown in Figure 42. This diagram shows the change of <sup>13</sup> CO <sub>2</sub> and <sup>12</sup> CO <sub>2</sub> asymmetric stretching mode $\nu_3$ between 10 K (or 30 K) and 85 K during the slow heating up process. . . . .	82

# Preface

Part of the content of Chapter 2 is taken from

Jiao He, **SM Emtiaz**, Adwin Boogert, Gianfranco Vidali; ‘The  $^{12}\text{CO}_2$  and  $^{13}\text{CO}_2$  Absorption Bands as Tracers of the Thermal History of Interstellar Icy Grain Mantles’. In: *Astrophys J.* 869.1 (2018), p. 41. doi: 10.3847/1538-4357/aae9dc.

The content of Chapter 3 is taken from

**Shahnewaz M. Emtiaz**, F. Toriello, J. He, G. Vidali; ‘Infrared Spectroscopic Study of Solid Methane: Nuclear Spin Conversion of Stable and Metastable Phases’; *The Journal of Physical Chemistry A* 0.0 (2020). PMID: 31891499, null. doi: 10.1021/acs.jpca.9b10643.  
url:<https://doi.org/10.1021/acs.jpca.9b10643>.

The content of Chapter 4 is taken from

**Shahnewaz M. Emtiaz**, F. Toriello, J. He, G. Vidali; ‘Infrared Spectroscopic Study of Crystalline Methane and Methane mixture with Volatiles of Astrophysical Importance’; in prep, 2020.

The content of Chapter 5 is taken from

**Shahnewaz M. Emtiaz**, F. Toriello, J. He, F. Chahili, G. Vidali; ‘Temperature evolution of  $\text{CH}_4:\text{N}_2$  ice mixture - an Application to trans-Neptunian Object’; in prep, 2020.

The content of Chapter 6 is taken from

**Shahnewaz M. Emtiaz**, J. He, G. Vidali; ‘Self-diffusion in  $^{12}\text{CO}_2$  and  $^{13}\text{CO}_2$  Thin Films’; in prep, 2020.

*To my father in heaven.*

# Chapter 1

## Introduction

### 1.1 Background

Ices are ubiquitous throughout the Universe. The structure and composition of ices of water and other volatiles hold key information on the physical, chemical, and biological processes relevant to a large number of natural systems. A number of properties such as morphology, phase transition, and segregation behavior can be explored when the molecules are locked into the solid-state under Ultra High Vacuum (UHV) condition. The importance of ices found in the interstellar medium (ISM) and planetary bodies is irrefutable. The process of condensation of gas-phase species on interstellar dust grains and subsequent reactions with molecules in the ices has gained great importance, since it affects star formation and enriches the chemical make-up of the interstellar medium. The study of the evolution of the ices found in astrophysical environments is important as icy grain mantles are the main reservoir for the volatile elements in star-forming regions across the universe, as well as the formation site of pre-biotic complex organic molecules (COMs) that are found in our Solar System. Our solar system is also full of ice-rich environments such as trans-Neptunian objects, satellites of larger planets, and comets. The ice composition of these objects has become one of the most important pieces of information to characterize the physical and chemical conditions in the early solar systems, thus helping finding the clue of origin of life. In addition to ISM and planetary bodies, ices are found in the Earth's atmosphere, mountain tops, and in the ocean depths. In fact, in the prebiotic evolution phase, there have been many ice ages on Earth, most of them long before humans made their first appearance.

This thesis focuses on the physical processes (i.e. phase transition, segregation, diffusion, etc) that happen in pure ices and key ice mixtures under simulated interstellar medium conditions as well as planetary surface conditions. It demonstrates the use of infrared spectroscopy as a probe of

the thermal history of the different astrophysical environments.

## 1.2 Interstellar Medium

The interstellar medium (ISM) is the birthplace of stars and planetary systems [10, 87]. Until the middle of 1960's, the region between the stars (the ISM) was considered to be very hostile for the existence of an appreciable number of molecules. This perception was proven wrong by the observation of molecules such as  $\text{NH}_3$ ,  $\text{H}_2\text{CO}$ , and  $\text{H}_2\text{O}$  [50]. The ISM is filled with gas (99% in mass) and dust (1% in mass). The gas is composed of hydrogen (H, 70%), helium (He, 28%), and a fraction of heavier elements; gas and dust are not distributed uniformly over the ISM. Therefore, there exist regions that are dominated by high densities and low temperatures. It is in the dense cloud regions of the ISM where star formation initiates. When such a dense cloud of gas and dust collapses gravitationally, first it does in clumps, then in dense cores, each of which can then start the further collapse and formation of a young star. The details of how this happens are not well understood [62]. One difficulty is that most regions where this process is underway already have formed stars nearby. Those stars affect subsequent nearby star formation through their stellar winds and shock waves when they explode as supernovae.

Species	NGC 7538 IRS 9	W33A	Comets
$\text{H}_2\text{O}$	100	100	100
CO	16	8	5-30
$\text{CO}_2$	22	13	3-20
$\text{CH}_4$	2	1.5	1
$\text{CH}_3\text{OH}$	5	18	0.3-5
$\text{H}_2\text{CO}$	4	6	0.2-1
HCOOH	3	7	0.05
OCS	-	0.2	0.5
$\text{NH}_3$	13	15	0.1-1.8
XCN	1	3.5	0.01-0.4

Table 1: Ice abundances with respect to  $\text{H}_2\text{O}$  ice towards young stellar object NGC 7538 IRS 9, high-mass protostar W33A, and Comets; taken from [29]

## 1.3 Ices in Space

More than 200 different molecules have been identified in the circumstellar and ISM [5]. The chemical species found in ISM is heterogeneous, ranging from atoms, diatomic molecules, to large organic carbon chain, radicals, and ions. It was initially thought that conditions within these dense molecular clouds, characterized by low temperatures (10–20 K) and pressures, were not conducive to chemistry. However, a combination of infrared, millimeter, and microwave spectroscopy has shown that this is not the case. In fact, these regions exhibit rich chemistry and are the birth sites for stars and planets. Considering the molecular abundance in ISM, van de Hulst [88] realized that condensation of gas-phase elements on cold dust particles lead to the formation of H<sub>2</sub>O, CH<sub>4</sub>, and NH<sub>3</sub> ices on dust grains. A sample overview of ice composition with respect to H<sub>2</sub>O ice towards three different astronomical objects is presented in Table 1 [29]. Comparing the ice composition variation and abundance between star formation stages and low- and high-mass protostellar environments provides information on the formation of ice components and chronicles ice evolution across star-formation.

### 1.3.1 Interstellar dust

Dust grain particles are also found in the ISM. Dust grains are submicron particles that makeup only around 1% of the total mass of the interstellar medium (ISM), but play a pivotal role in its chemistry. Interstellar dust grains are primarily made up of a mix of amorphous silicates and carbonaceous materials [22, 30]. A sample representation of an interstellar dust grain is shown in Figure 2 [16]. Out of these 200 molecules reported by astronomers, some molecules freeze out on dust grain surface at the cold temperatures of the dust grain (10–20 K), while others are formed in the ices in reactions with atoms and other molecules. Dust grain serves two main purposes in interstellar ice evolution. Firstly, the surface serves as a local 'meeting point' for molecules or atoms that become bound to the dust grain via electrostatic or van der Waals forces, a process called physisorption, or by forming chemical bonds with its surface (chemisorption). Secondly, the dust grain can accommodate a portion of the excess energy usually generated during surface-mediated association reactions, stabilizing the product, and thus allowing large polyatomic species to be efficiently synthesized.

### 1.3.2 Interstellar ice evolution

In the context of the ISM, the name 'ices' doesn't just refer to water ices (water being the most abundant molecule in ices), but encompasses all solids that consist of volatiles (molecules that are

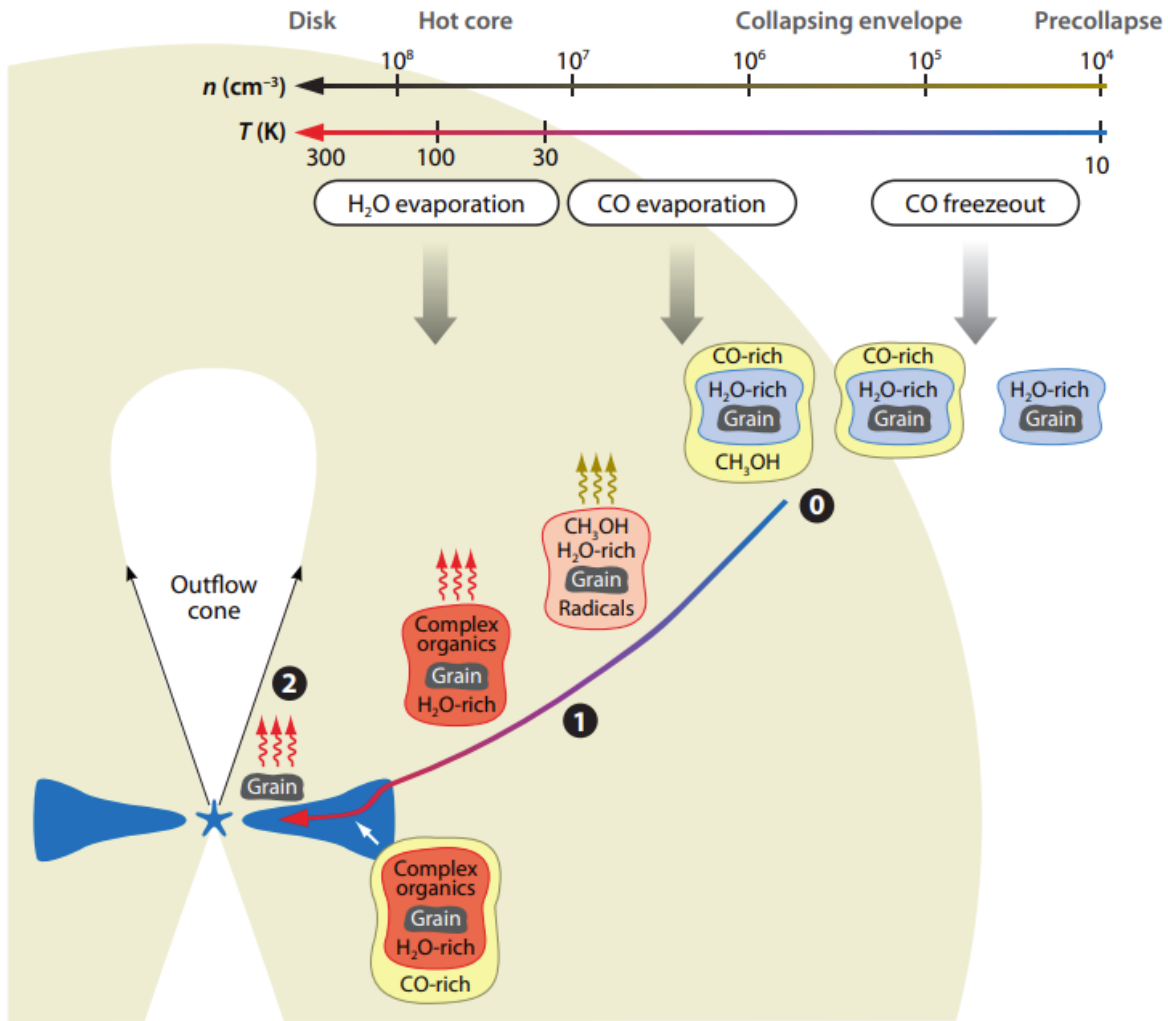


Figure 1: Cartoon representation of the interstellar ice composition starting from the prestellar stage through the collapsing envelop, and into a protoplanetary disk. Adapted from [41, 16]

in gaseous or liquid form at room temperature and atmospheric pressure). Among the observed interstellar molecules, at least 50 species contain six or more atoms and at least one carbon atom; these species are called Complex Organic Molecules (COMs) [41]. One should keep in mind that the term 'complex' directly relates to the ISM, as for molecular complexity on Earth most of the COMs are considered to be rather simple species. Herbst and van Dishoeck [41] modeled the steps of interstellar ice evolution which are shown in 1. In the ISM, as a cloud get denser, water is formed on the grain from hydrogen and oxygen. In the densest clouds, the  $\text{H}_2\text{O}$ -dominated ice mantle becomes covered with the gas-phase freeze out of CO, yielding a CO-rich ice mantle. In the protostellar phase, the radiation from the forming star heats the surrounding parent cloud (now

called "hot-core") to 100K, leading eventually to the sublimation of the ice mantle. This process gives rise to active hot-core chemistry which takes place both in the ice and in the gas-phase following the release of atoms and molecules from the ice. Eventually, ices and bare dust grains will settle in the mid-plane of the protoplanetary disks where planets and comets are formed.

### 1.3.3 Interstellar ice formation mechanisms

Over the last several decades, significant progress has been made regarding the understanding of the formation (and subsequent destruction) of molecules within interstellar space. Current astrophysical models indicate that gas-phase chemistry alone cannot account for the variety and richness of molecules observed in star-forming regions [41]. During the lifetime of a molecular cloud ( $10^6$ – $10^8$  years) ices formed on dust grains undergo significant physical and chemical changes depending on the astrophysical environment [16]. A summary of some of the probable processing routes for interstellar ices is shown in the inset of Figure 1. The most important mechanisms that most likely dictate the interstellar ice formation mechanism are discussed below:

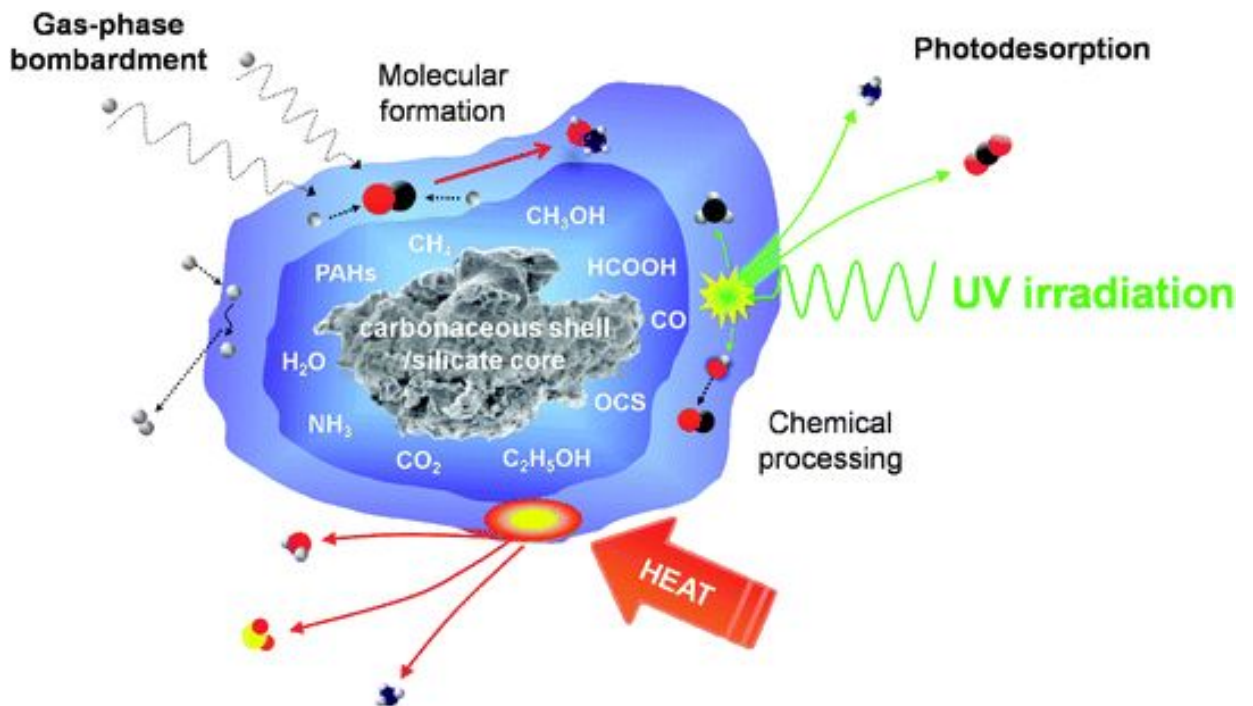


Figure 2: Cartoon representation of a dust grain and of the main routes of interstellar ice processing that takes place in astrophysical environments; taken from [16]

- **Atom and radical addition reaction** is the mechanism responsible for the most primitive solid-state interstellar ice chemical evolution on the dust grain surface. In this mechanism, the dust grain acts as a neutral body that catalyzes the chemical and physical interaction of atoms at the surface. At very low temperatures (10 K) atomic species such as H, D, N, C, and O form simple molecules via thermal hopping or quantum tunneling on the grain surfaces [85]. As the interstellar medium is abundant with hydrogen (H) atoms, hydrogenation is the most dominant atom addition reaction on the grain surface. H-addition or hydrogenation forms molecules such as H<sub>2</sub> (through H+H), H<sub>2</sub>O (hydrogenation of O/O<sub>2</sub>/O<sub>3</sub>), NH<sub>3</sub> (hydrogenation of N atoms), CH<sub>3</sub>OH (hydrogenation of CO), and CH<sub>4</sub> (hydrogenation of C atoms) [20, 85, 34, 86]. On the other hand, grain surface bound C, N and O atoms form more volatile species including CO<sub>2</sub>, N<sub>2</sub>, and O<sub>2</sub> in the regions where the H/H<sub>2</sub> ratio is much lower [86, 24, 87]. Some of the interactions, such as radical-molecule and radical-radical, often don't require any activation energy and therefore can easily take place even at low temperature (10 K).
- **Energetic processing** is the mechanism in which the primitive species discussed above undergo further processing by the exposure of UV radiation and cosmic rays. As opposed to the atom addition process, this requires energetic input. Laboratory studies have shown that simulated ice grains exposed to UV irradiation induce the formation of complex organics such as NH<sub>2</sub>CHO, OCN<sup>-</sup> and C<sub>2</sub>H<sub>5</sub>OH [6, 72]. The chemical composition of ices can be further modified by gas-phase ion and electron bombardment. For example, a highly energetic ion passing through the onion-layer structure of ices causes the dissociation of hundreds of molecules along its path.
- **Thermal processing** can induce sublimation of ices materials and changes in ice morphology and segregation/diffusion of species in the ice. The heat generated by newborn stars stimulates further surface chemistry prior to the evaporation of these icy mantles during cloud collapse [16]. Most of the temperature-induced processes in interstellar ices take place within the range of 10 to 100 K. The temperature in hot cores of massive young stellar object formation can rise to in excess of 100 K. At this temperature, sublimation of ices gives rise to the enrichment of the gas-phase with new molecules;. The release of radicals from ices spurs new reactions in the gas phase, driving a rich chemistry that leads to the formation of larger organics with carbon branched structures [20].

The main focus of this thesis is the evolution of the interstellar ice mantle on dust grains and the thermal processing of interstellar and planetary ices. Studies have shown that the sublimation

of the interstellar ices is not an instantaneous process and there is a need to understand the change in physical and chemical properties of ices during the thermal evolution; therefore, a detailed laboratory study of the changes due to thermal cycles up to thermal desorption of interstellar ices from dust grains is essential for understanding the processes associated with star formation. Because ISM ices are thin (typically 100 layers or less), at low temperature (down to 10K), and in a disordered or amorphous state of aggregation, their properties have been scarcely explored in standard chemical physics or solid-state physics investigations.

### **1.3.4 Solar system ices**

The outer Solar System is abundant with ice-rich bodies such as comets, Trans-Neptunian Objects, asteroids, and icy planetary satellites. Although water-ice is the predominant component, in solar system bodies heterogeneous ice distribution involves  $\text{CO}_2$ ,  $\text{NH}_3$ ,  $\text{CH}_4$ , and  $\text{SO}_2$ . The largest deposits of  $\text{CO}_2$  is on Mars,  $\text{SO}_2$  ice is found in the Jupiter system, and  $\text{N}_2$  and  $\text{CH}_4$  ices are common beyond the Uranian system [21]. The surfaces of icy planetary bodies can be transformed by their exposure to a variety of particle and photon sources. The resultant chemistry can be highly variable since it depends on trace impurities delivered to those surfaces of the solar system bodies. Photon and particle bombardment also desorb material from icy surfaces, weathering the surface and producing tenuous atmospheres. Within the upper layers of icy surfaces, photolysis, radiolysis, and reactions involving free radicals are expected to occur. These processes are crucial to influencing the survivability of the building blocks of the origin of life (i.e., amino acids) as well as the reaction products that may be signatures of biologically important parent molecules. In order to successfully interpret remote sensing data obtained from spacecraft and ground-based observations, a detailed understanding of the chemistry within these icy environments of the solar system is essential.

## **1.4 Laboratory Simulation of Space Ices**

Mid-infrared band profiles of interstellar ice hold an enormous amount of information that is key to understand the evolution of our solar system and beyond. Laboratory experiments play an integral role in the analysis of the observational data of ices. It has experimentally proven that IR ice bands can act as an excellent probe of the thermal history of the space environment. In order to simulate interstellar and planetary environments, one needs to keep in mind several key characteristics of these regions; extreme high vacuum, cryogenic temperature, and the presence of dust grains in various morphological states that are loci of surface interaction of molecules. Thus laboratory

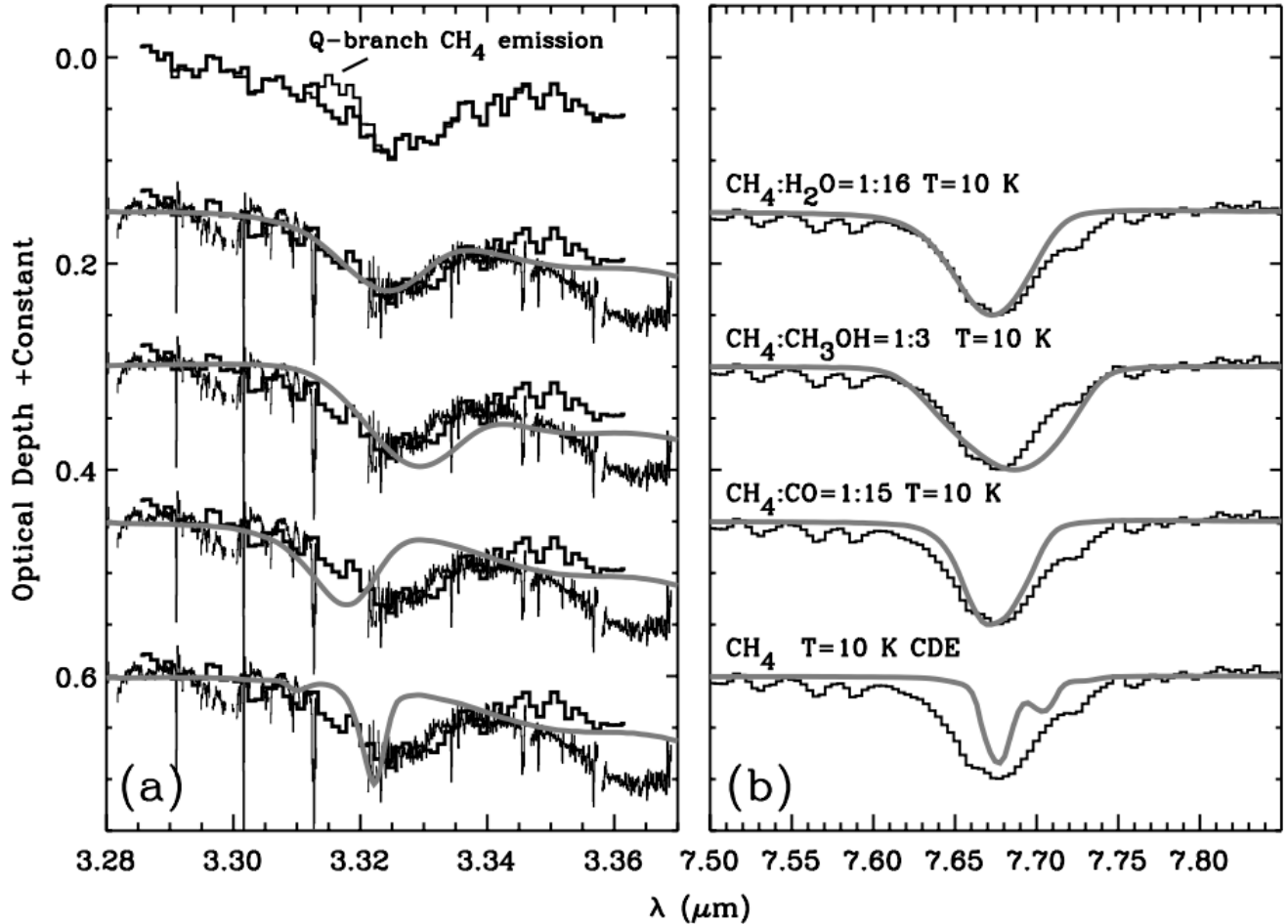


Figure 3: Comparison between observation and laboratory simulated  $\text{CH}_4$  ice and ice mixture (a)  $\nu_3$  stretching mode of solid  $\text{CH}_4$  observed with ISO SWS (thick line) and KECK/ NIRSPEC (thin line), compared to a number of laboratory ice simulations (smooth gray line). (b) The  $\text{CH}_4$   $\nu_4$  bending mode is fitted with the same laboratory ice, without scaling the peak optical depth. Best fits are obtained with  $\text{H}_2\text{O}$ -rich ices. Note the poor fit of CO-rich ices to the  $\text{CH}_4$  stretching mode.; taken from [13]

simulation of space ice requires the experiments to be performed under astrophysical conditions, using UHV conditions to reduce surface contamination by residual gas, by reducing the number of molecules reaching the sample over a given time period, low temperatures ( $<20$  K), and a suitable model dust grain surface. Interstellar  $\text{CH}_4$  is believed to form by atomic addition reaction of C and H atoms and mostly in a  $\text{H}_2\text{O}$  rich environment. Figure 3 shows a comparison between observation and laboratory data for pure  $\text{CH}_4$  and  $\text{CH}_4$  mixed with other molecules [13]. The main goal of laboratory simulation of ices is to probe how chemical processes depend on binding sites,

sticking probabilities, binding energies, desorption kinetics, and diffusion. Specifically, surface analysis techniques are used, since processes occur in thin films exposed to atoms and molecules from the gas-phase. Infrared spectroscopy is a very strong tool for the investigation of surfaces and adsorbed films. It has a distinct advantage over other surface analysis techniques as it provides highly specific molecular and structural information of the of ultra-thin adsorbate films on flat solid substrates. In our set-up it is used in-situ and in real-time; the geometry used (grazing incidence absorption and reflection) gives a sensitivity advantage over the more common studies in transmission. For astronomers, infrared spectroscopy is the fundamental tool to observe rich chemistry. Therefore, information from laboratory experiments can be rapidly applied to understand observations. Apart from identifying the frozen-out species, mid-IR absorption spectra in conjunction with calculations can be used to obtain information on the physical properties of the ice, such as morphology, phase changes, degree of mixing, and interactions among species.

The apparatus and methods we use to simulate properties of and processes in interstellar and planetary ices are discussed in Chapter 2.

## 1.5 Thesis Outline

This thesis presents the detailed laboratory-based research on thermal processing of simulated ices in ISM and planetary environments. It is aimed to increase our understanding of the physical and chemical processes that occur in space ices. The bulk of this thesis involves thermal heating of ices that mimics the one in prestellar cores and on surfaces of ice of outer solar system bodies. The summary of the chapters of this thesis is provided in the following;

- **Chapter 2** introduces the laboratory apparatus at Syracuse University Surface Science and Astrophysics Laboratory that I used to conduct all the experiments in this thesis. This ultrahigh vacuum setup is used to study the thermal processing of atoms and radicals on dust grain analogs at astronomically relevant cryogenic temperatures. The description of the apparatus and methods is indeed the main focus of the chapter. In this chapter, I also describe my contribution toward the development and upgrade of the apparatus for the research that I carried out.
- **Chapter 3** reports the discovery of a new metastable phase of methane ( $\text{CH}_4$ ) ice upon deposition at  $T < 7$  K. We found that after the deposition at 6 K and annealed to a higher temperature, a phase transition from the metastable phase to a stable crystalline phase takes place. We report new measurements of temporal changes of infrared spectra of methane ice

in the  $\nu_3$  and  $\nu_4$  bands due to nuclear spin conversion between 6.0-11.0 K for 6 K and 30 K deposited methane ice.

- **Chapter 4** I study the segregation/diffusion processes of  $\text{CH}_4$ ,  $\text{N}_2$ , and  $\text{H}_2\text{O}$  that form on dust grains during star formation. We report that  $\text{H}_2\text{O}$  segregates from a  $\text{CH}_4:\text{H}_2\text{O}$  mixture when the ice undergoes thermal processing between 10 and 30 K. On the other hand,  $\text{N}_2$  molecules diffuse in a  $\text{CH}_4:\text{N}_2$  mixture during thermal processing between 10 and 20 K. These findings are then related to processes in interstellar and planetary environments.
- **Chapter 5** investigates the thermal processing of a  $\text{CH}_4:\text{N}_2$  ice mixture that is present in cold outer solar system bodies. We found two transformations in  $\text{CH}_4:\text{N}_2$  ice when it is heated up slowly from 10 to 40 K. We calculated the activation energy for the 1<sup>st</sup> transformation and modeled it based on different mixing ratios and film thickness.
- **Chapter 6** introduces a completely new thin-film physical phenomenon in an isotopic mixture of  $\text{CO}_2$  which might be related to self-diffusion of molecules. Although self-diffusion of molecules has been studied in nano-particles, there is no prior study of the effect of resonant dipolar interactions and self-diffusion in the reduced geometry of thin films, as is appropriate for astrophysical applications.
- **Chapter 7** summarizes the most critical findings of this thesis. The application of the research findings to astrophysics is threefold. First, the results obtained from the experimental study can be compared with observational data of ISM and planetary ices to understand the physical processes that occur during the thermal processing in an astrophysical environment. Second, the data on the thermal evolution of ices and diffusion of guest molecules will be useful to modelers. Modelers have been using coupled rate equations to model ices; but the real breakthrough is to simulate processes at the atomic scale, using, for example, Monte Carlo codes. This research provides the necessary input for those simulations. Third, the study in this thesis opens a new route of experiments that can be used as a reference point for future observational data obtained by future ground-based and space telescopes, most notably the soon-to-be-launched James Web Space Telescope (JWST).

# Chapter 2

## Experimental Setup

### 2.1 General

A detailed description of the Syracuse University Laboratory of Astrophysics and Surface Science UHV apparatus is presented in the following sections. The description of the apparatus is highlighted in three sections, namely, the main chamber, the beamline, and the Fourier Transform Infrared Spectroscopy (FTIR) setup. The emphasis of this chapter is on the changes made in recent years.

### 2.2 Main Chamber

The experiments in this thesis were performed in an ultra-high vacuum (UHV) chamber. A schematic is shown in Figure 4.

The main chamber is pumped by a combination of several turbomolecular pumps, an ion pump, and a cryopump. Each time the Ultra High Vacuum (UHV) condition is violated, the whole chamber is baked at about 80 °C for at least 4-5 days to remove gases adsorbed on the chamber walls, mostly water vapor. A higher bake-out temperature is desirable, but due to temperature-sensitive parts of the main chamber, the highest bake-out temperature is always maintained  $\leq 100$  °C. Once cooled down to room temperature, the main chamber base pressure is  $(1-3)\times 10^{-10}$  torr. At this pressure, the background deposition on the cold finger is effectively insignificant. A Hi-den HAL/3F quadrupole mass spectrometer (QMS) is mounted vertically on a doubly differentially pumped Thermionic RN-1000 rotary platform. The rotary platform can be rotated by a stepper motor which is controlled by an Applied Motion ST10-S stepper motor controller. Thus, the QMS can either face the molecular beam to measure its composition or face the sample to measure the species desorbing from it. The QMS operates as a residual gas analyzer (RGA) when the partial pressure

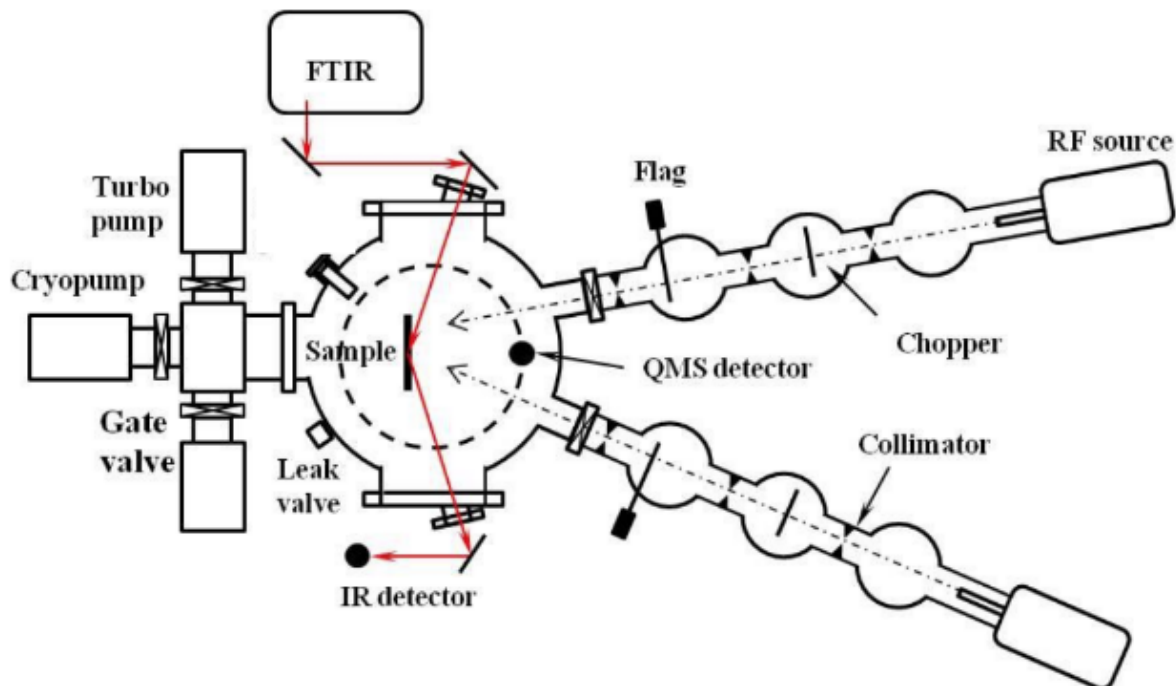


Figure 4: A schematics of the main apparatus.

of the molecules is measured to find out molecular composition under UHV condition. The QMS ion current can be read using client software provided by Hiden Analytical, or, alternatively, the ion pulse signal can be output to an external pulse counting device, such as a multichannel scaler (FastComTech MCS-4), for better time resolution. The QMS ionizer is surrounded by a stainless steel cap with a Teflon cone (see Figure 6) attached to it. The entrance of the ionizer and the cone are lined up so that most of the gas molecules that enter the cone go into the QMS ionizer. During the exposure stage, the QMS detector is moved away from the sample so that the detector does not block the molecular beam. During the Temperature Programmed Desorption (TPD) experiments, the sample is close to the cone entrance (see Figure 6), so that the cone fully covers the beam spot on the sample to increase the QMS signal while minimizing the noise due to the desorption from other cold parts of the sample holder. The sample holder is mounted on a Huntington XYZ 3-dimensional translation manipulator. The manipulator is sitting on a Thermionics RNN-600 rotary platform. Both the RNN-600 and the RNN-1000 rotary platforms are double differentially pumped by a turbomolecular pump and a rotary pump system. This configuration gives the sample the freedom of translation in three dimensions and rotation around the vertical axis.

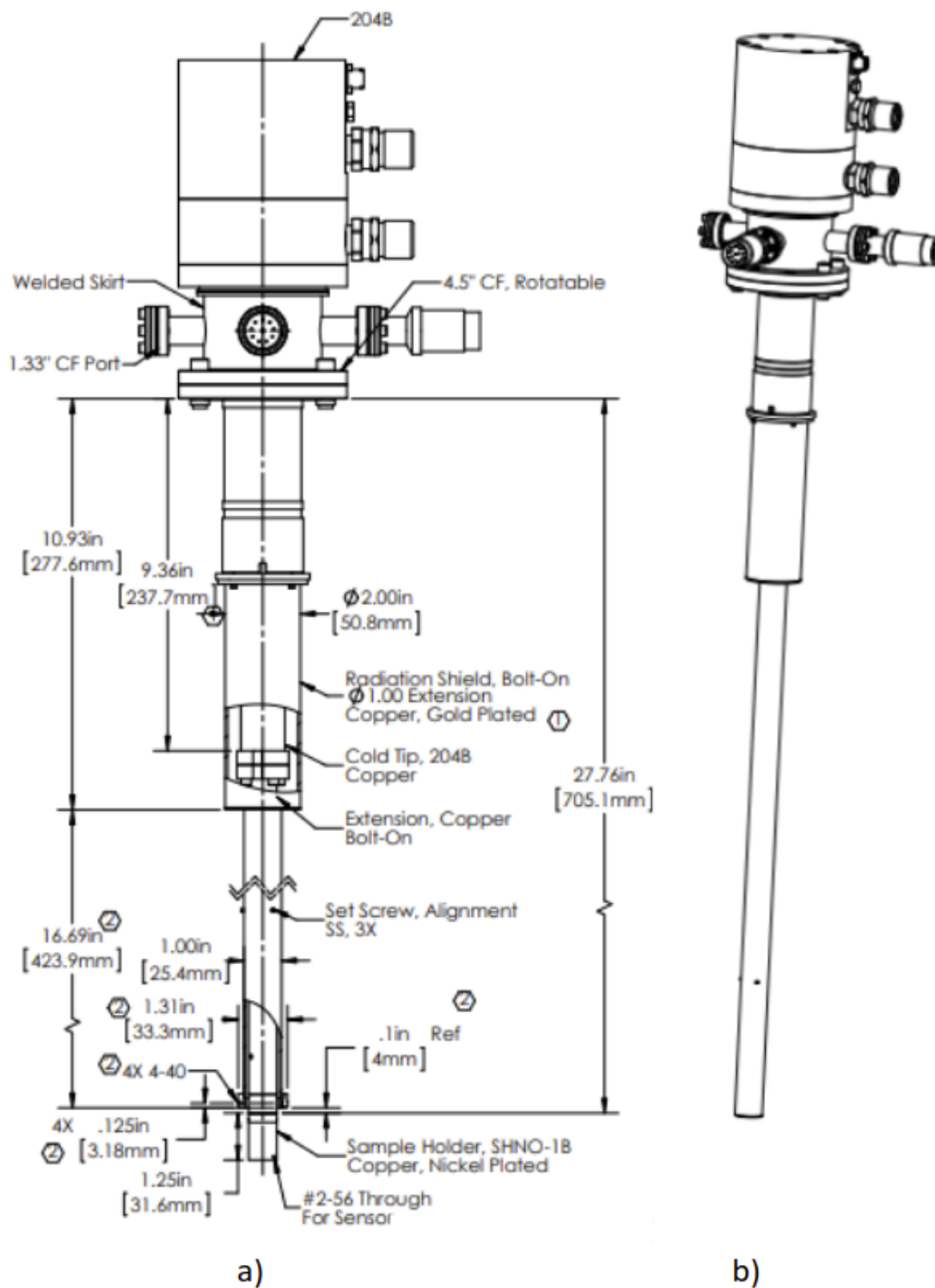


Figure 5: Cryocooler schematics. a) 2D diagram with dimensions of the redesigned cryostat system, b) 3D model of the redesigned cryostat.

### 2.2.1 Cryocooler installation

A continued upgrade of the apparatus is essential to keep up with the state of art research in the field of Astrochemistry. We inherited an ARS (Advanced Research System)-LT3B-Helitrans for cooling the cold finger to 8 K. This type of cooling system requires liquid helium which is not very convenient for long experiments as the ones presented in Chapter 3. Cooling to  $\leq 8$  K was essential for some of projects presented in this thesis (Chapter 3, 4, and 5). We installed an ARS DE204B cryostat which improved the cooling performance to 5 K. I collaborated with the ARS engineer to implement the cryostat installation. Some design issues were needed to be addressed to adapt the instrument to our apparatus in a timely manner. The custom-built ARS- DE204B has a cold finger 1.75 inch OD and the Huntington XYZ manipulator mentioned in the previous section has a 2 bellow with 2.0 inch ID. Thus, it was impossible to install the custom-built cryostat while keeping the existing apparatus set-up. The extended cold finger and cooling column radiation shield were designed and implemented to make sure the cryostat could be installed without altering the existing setup while keeping the efficient cooling performance of the sample. Figure 5 shows the 2D and 3D models of the cryostat that was installed in 2016.

### 2.2.2 Sample and radiation shield

A sample holder is mounted at the cold tip of the cryostat extended cold finger. The sample holder unit is a solid oxygen-free, high conductivity copper block in which the sample is housed. The sample is a 1 cm diameter copper disk which is mechanically polished and gold plated by an external vendor, Anoplate. Underneath the sample, there is a small cylindrical cavity in which a 50  $\Omega$  cartridge heater is installed. The heater is chosen to be powerful enough so as to have a linear temperature ramp at the sample up to 300 K. The temperature of the sample is measured by a Lakeshore DT-670 silicon diode that is pressed in a small cavity between the sample and sample holder. The temperature of the sample can be adjusted between 5 K and 300 K. This measurement is read and controlled with a precision of 50mK by a Lakeshore 336 Temperature controller in conjunction with a LabVIEW program.

There is a gold-coated copper radiation shield installed around the sample holder unit such that it covers all but the sample itself leaving the gold surface exposed (see Figure 6 left panel). While installing the closed cycle cryostat, a gold-coated radiation shield collar was installed to make sure the sample radiation shield could be housed with the cold finger radiation shield. The purpose of the shield is to isolate the thermal radiation so that the sample substrate can reach a lower temperature than that of the shield itself. This arrangement also prevents adsorption of gases on to the sample holder or cold finger itself. In this way, only the surface of the sample adsorbs the

deposited atomic and molecular gas species. The temperature of the radiation shield is monitored by the connected thermocouple wires. Figure 6 shows the front and side view of the sample and radiation shield arrangement.

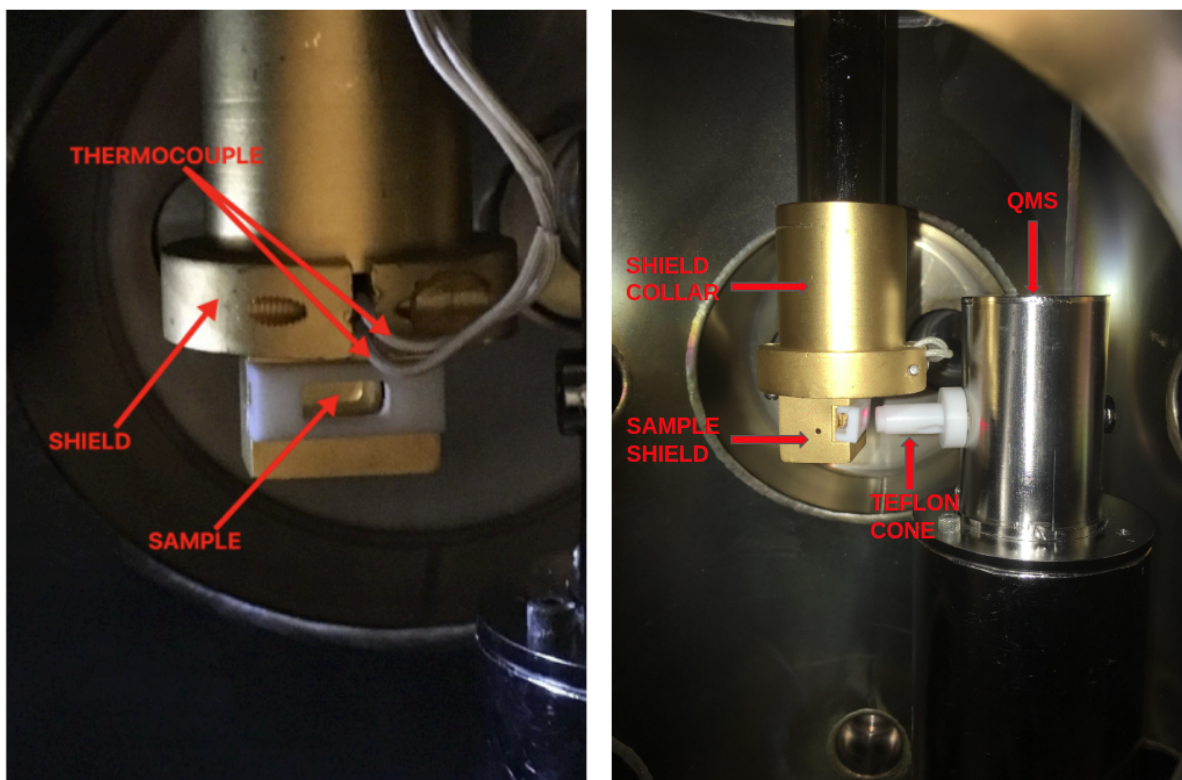


Figure 6: Sample, radiation shield and QMS setup. a) Front view of the sample and radiation shield that thermally isolates the cold part of the cooling column and sample from the UHV chamber. b) Side view of the setup.

### 2.3 Molecular Beamline

There are two triple-stage differentially pumped molecular beamlines connected with the main chamber (see Figure 7). These beamlines operate in a High Vacuum (HV) condition. Each beamline consists of three vacuum chambers that are individually pumped and connected to each other by stainless steel port and by a bellow to the UHV chamber. The first and second stages are pumped by diffusion pumps while the third stage is pumped by a turbomolecular pump. Collimators are installed between stages. These three collimators ensure that the molecular beam is well focused on a 3 mm diameter spot on the sample surface. A radio frequency dissociation source is mounted onto the first stage. An Alicat MCS-5 mass flow controller is used to control the gas flow. The

direct beam is measured by letting the QMS detector face the beamline and introducing gas into the beamline. Figure 7 shows the side view schematics of a molecular beamline.

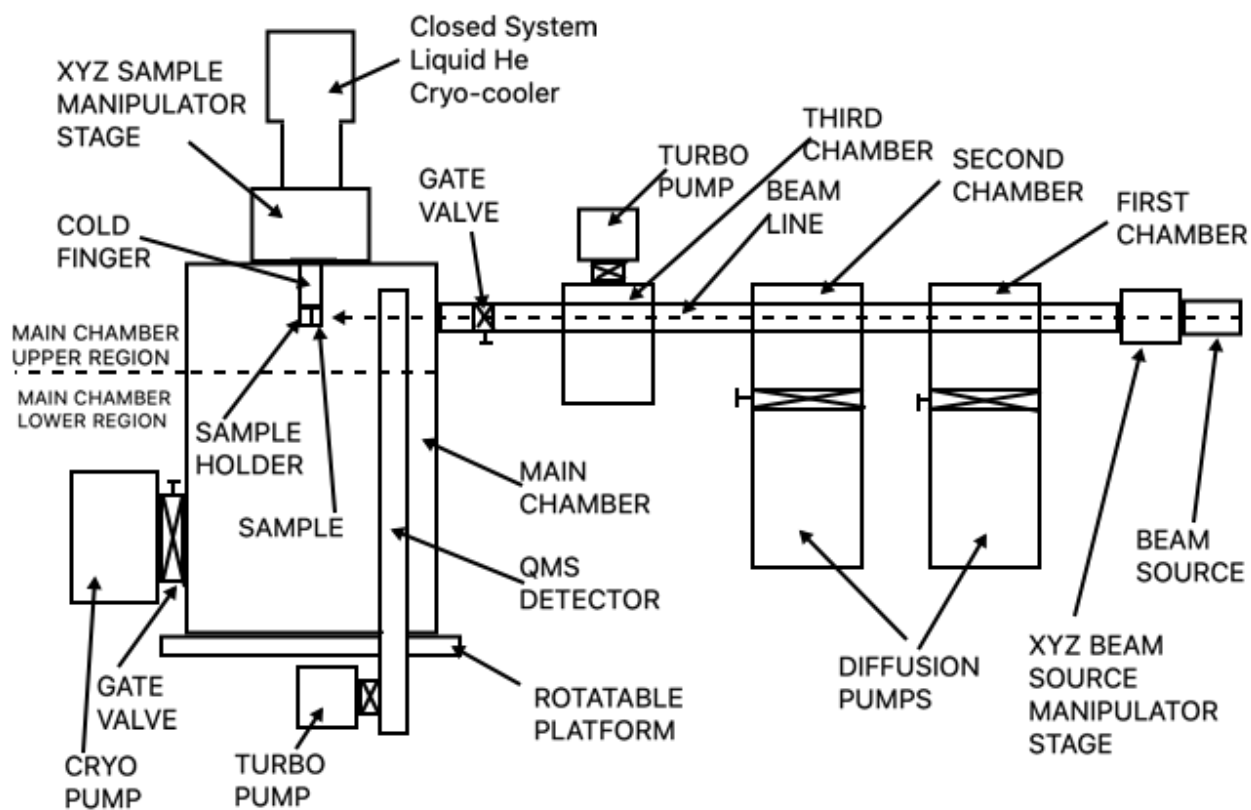


Figure 7: Side view of experimental apparatus. Details are given in the text; courtesy Francis Toriello's thesis.

## 2.4 Infrared Spectroscopy

Infrared (IR) spectroscopy is widely used to probe vibrational modes of molecules. Infrared light induces vibrational transitions in the molecular bonds, and by measuring the frequency and intensity of the absorbed infrared light, information such as chemical environment and structure can be explored. In IR spectroscopy, an infrared lamp produces electromagnetic radiation between the wavelengths of 700 nm to 1 mm. While astronomers use wavelength units (microns), laboratory spectroscopists use wavenumbers ( $\nu \propto 1/\lambda$ ), since vibrational excitations are usually given at characteristic frequencies in molecules. When a spectrum of a molecular species or ice mixture is

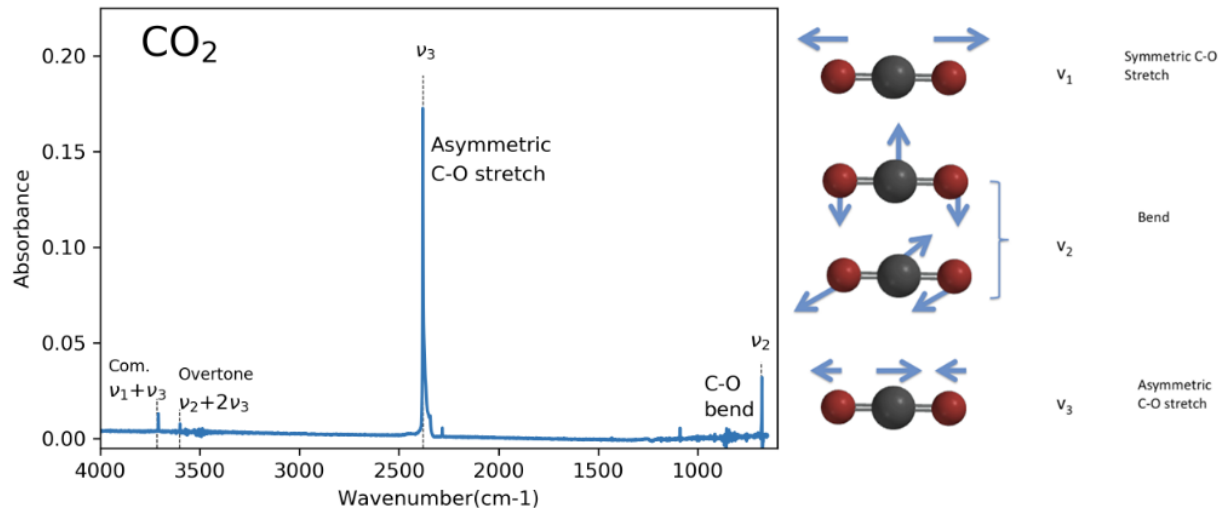


Figure 8: IR spectra of CO<sub>2</sub> and its vibrational modes. Main panel: IR spectrum of CO<sub>2</sub> showing absorbance maxima associated with varying modes of vibration. The inset figure shows the four theoretically possible vibrational modes of CO<sub>2</sub>: a) asymmetric stretch of CO<sub>2</sub>, b) vertical and horizontal bend, and c) symmetric stretch (st), which lacks change in dipole and consequently has no IR signature.

taken, the spectrometer scans through a range of wavelengths (frequencies). The detector measures the reduction of the frequency of the electromagnetic radiation absorbed by the sample, resulting in an absorbance peak on the spectrum. This peak occurs at this frequency due to the stretching and compressing of bonds in a molecule. Figure 8 shows a sample IR absorbance bands of CO<sub>2</sub> solid with different modes of vibration.

## 2.5 Fourier Transform Infrared Spectroscopy (FTIR) Setup

FTIR (Fourier Transform InfraRed) is now the standard method to obtain an IR spectrum over a wide range of wavenumbers. Infrared radiation is directed from the source through a series of gold-coated mirrors towards the surface of the sample (gold-coated copper disk) and the impinging photons interact with the surface molecules before reflecting from the sample plane. Gold is preferred for the coating as it has high reflectivity which ensures a strong FTIR signal. The incident and reflected IR beam are directed and focused on the detector through a series of gold-coated mirrors (Edmund), see Figure 9 for details. The raw signal is then Fourier transformed into the familiar frequency domain. The best sensitivity for FTIR measurements on the metallic surface is

obtained using a grazing incidence of the IR radiation.

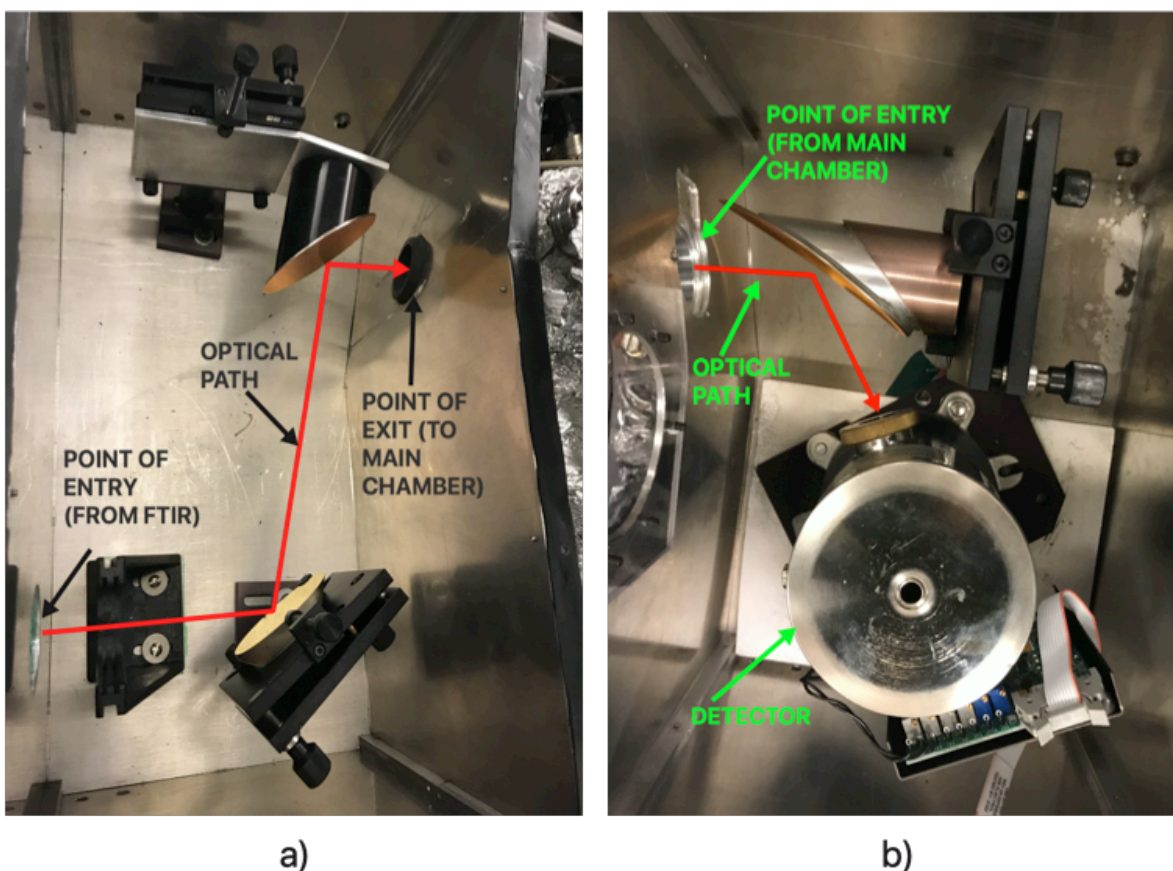


Figure 9: Optical path of Reflection Absorption InfraRed Spectroscopy (RAIRS) setup.

The observation of the vibrational modes of adsorbates on the metallic substrates is subject to *surface dipole selection rule*, the rule states that only those vibrational modes which give rise to an oscillating dipole perpendicular to the surface are IR active and give rise to an observable absorption band. MCT-A detector with a capability of detecting a range of near-IR and mid-IR ( $5000\text{-}650\text{ cm}^{-1}$ ) vibrational spectra of ices for IR radiation produced from Nicolet 6700 Fourier Transfer Infrared Spectrometer (FTIR) and incident at a grazing angle of  $\approx 80^\circ$  is used in the Reflection Absorption InfraRed Spectroscopy (RAIRS) configuration shown in Figure 4.

## 2.6 Deposition of Gases

Gas species can be deposited onto the sample through background deposition using two UHV precision leak valves activated by two stepper motors controlled by a LabVIEW program. For the

deposition of a single molecular species, the program first measures the base pressure of the chamber, and then calculates the target partial pressure based on a user set deposition rate. The pressure readings from the hot cathode ion gauge are corrected for the gas species in the LabVIEW program. A PID control loop is used to maintain the pressure at the target value. In the deposition of CH<sub>4</sub>, it takes about 20 s for the pressure to stabilize at the set value. The ice thickness during deposition is calculated by the program in real time. When the thickness reaches the set-point, the leak valve is closed quickly. Even after the valve is closed, the residual gas in the chamber continues being deposited on the sample, until it is pumped out. We correct for the additional amount deposited from the residual gas by closing the valve slightly before the target thickness is reached. The exact offset thickness is calculated from the deposition pressure and the pumping speed. After this correction, in the deposition of CH<sub>4</sub>, the relative uncertainty of thickness measured by the integration of pressure over time is usually less than 0.1%. For water deposition, the uncertainty is larger (1%) because of the difficulty in maintaining a stable water inlet pressure in the gas manifold.

In CH<sub>4</sub>:H<sub>2</sub>O co-depositions, as showed in Chapter 4, since the ion gauge can only measure the total pressure but not the partial pressure of each gas, we start with the deposition of one gas; CH<sub>4</sub> is deposited first because it is easier to control its deposition. Within 20 s of introducing CH<sub>4</sub>, the deposition rate is already stable. We tested the stability of pressure by fixing the valve position after 20 s, and found that the pressure does not change over time. The same is not true for water because of the instability of inlet pressure. After determining the stable valve position for CH<sub>4</sub>, we stop the PID loop for the CH<sub>4</sub> valve and fix the valve position. We then use a PID loop for the water leak valve to obtain a stable pressure during co-deposition. When the set time is reached, both leak valves are closed immediately. For the co-depositions in this study, the deposition is over 25 minutes, and therefore the uncertainty in CH<sub>4</sub> amount is about 20 s over 25 minutes, which is about 1%.

The impingement rate (IPR), which is the number of molecules deposited per unit surface area per unit time, is calculated as follows:

$$IPR = \frac{P}{\sqrt{2\pi m k_B T}} \quad (2.1)$$

where P is the chamber pressure after correction for the ion gauge gas specific ionization cross-section, m is the mass of gas molecule, T is the gas temperature (assumed to be room temperature), and  $k_B$  is the Boltzmann constant. It is assumed that the sticking of both CH<sub>4</sub> and H<sub>2</sub>O are unity at 10 K [35], and the pressure in the vacuum chamber is uniform. This is a fair assumption, because the leak valves openings do not face the sample or cold head directly. The IPR can be converted to units of monolayer per second (ML/s) by assuming 1 ML = 10<sup>15</sup> molecules/cm<sup>2</sup>. The absolute uncertainty of deposition is mostly due to the uncertainty in pressure measurement, and can be as

high as 30%, as this is the accuracy of a typical hot cathode ion gauge. In the experiments, the uncertainty in mixing ratio of the  $\text{CH}_4:\text{H}_2\text{O}$  mixtures is governed by the relative uncertainty, while that of the total thickness of the mixture is governed by the absolute uncertainty.

## 2.7 Thermal Processing of Ice

Thermal processing using IR spectroscopy is a strong tool to probe the temporal and thermal evolution of ice morphology. A schematic of a Thermal Processing experiment is shown in Figure 10. The IR spectra at regular intervals are collected with Omnic software and the temperature is recorded with the help of Lakeshore 336 temperature controller and a Labview program. Typically, a thermal processing experimental run consists of two stages. The first stage is the exposure stage, in which the sample surface is kept at relatively low temperature ( $\leq 10$  K) and a certain dose of molecules are sent to the sample surface using either a UHV leak valve (deposition from background gas) or the molecular beamline. The deposition dose calculation using the impingement rate is explained in the previous section. Once the pressure settles down to UHV condition after the exposure stage, the thermal processing stage is initiated. In this stage, the surface is heated up to thermally desorb species from the surface. A cartoon representation of  $\text{CO}_2$  thermal processing experiment is shown in Figure 10.

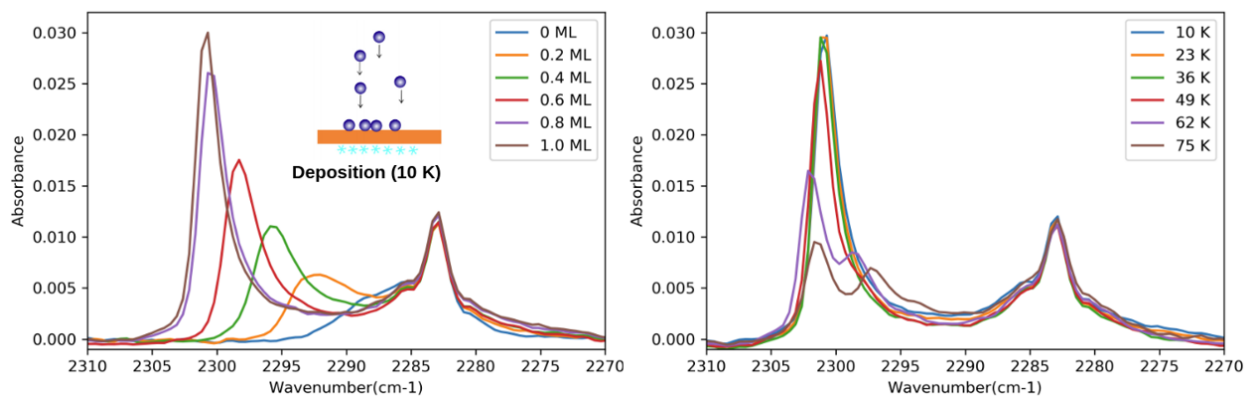


Figure 10: A sample thermal processing experiment of  $\text{CO}_2$  ice using RAIRS. Inset Figure courtesy Jaiio He's thesis.

## Chapter 3

# Infrared Spectroscopic Study of Solid Methane: Nuclear Spin Conversion of Stable and Metastable Phases

### 3.1 Abstract

Infrared spectroscopy was employed to study thin films of solid methane at low temperatures. We report new measurements of temporal changes of infrared spectra of methane ice in the  $\nu_3$  and  $\nu_4$  bands due to nuclear spin conversion upon rapid cooling from 30 K to 6.0-11.0 K. The relaxation rates of the nuclear spin were found to be a function of temperature. The activation energy associated with the relaxation has been determined over an extended temperature range. We also found a new metastable phase of methane ice upon deposition at  $T < 7$  K. After the deposition at 6 K and annealed to a higher temperature, a phase transition from the metastable phase to a stable crystalline phase takes place. We found that the relaxation has different activation energies below and above 8.5 K. From a quantitative analysis of the  $\nu_3$  and  $\nu_4$  IR bands, we suggest that the metastable phase is a crystalline phase with a degree of orientational disorder between the two known stable solid phases.

## 3.2 Introduction

Solid methane in the pure form is a representative of a non-polar molecular solid. Molecular solids are particularly interesting because, among other reasons, the interactions among molecules are easier to calculate. In the case of methane, there is an interest in knowing its state of aggregation in environments as diverse as at the bottom of oceans [70], in solar system bodies [84], in interstellar ices [14, 12, 59, 1], and in comets [11]. Molecules with two or more than two hydrogen atoms, such as H<sub>2</sub>, H<sub>2</sub>CO, H<sub>2</sub>O, NH<sub>3</sub> and CH<sub>4</sub>, can undergo the change of the nuclear spin, or nuclear spin conversion (NSC), while keeping the same parity of the wave-function [19, 63]. The case of CH<sub>4</sub> is particularly interesting because of the presence of three nuclear spin isomers; furthermore, the distribution of populations in the isomers can give clues to the origin and processing of CH<sub>4</sub> ice in comets [48]. The nuclear spin conversion has not been observed in the gas phase [83] and can be studied in laboratory timescales only in ices [17], whether in solid CH<sub>4</sub> [82] or CH<sub>4</sub> embedded in rare-gas [26, 81] or para-hydrogen matrices [55, 56].

At low pressure, there are two recognized and well documented solid phases. Phase I is the equilibrium phase at  $T > 20.4$  K. It is an fcc crystal with orientationally disordered CH<sub>4</sub> molecules. Phase II is stable below 20.4 K and consists of an fcc lattice with eight ferroorientational (orientationally ordered sublattices, six with dihedral symmetry  $D_{2d}$  and two sublattices of hindered rotators with octahedral symmetry  $O_h$ ). Thus, in the primitive cell, the six CH<sub>4</sub> that are orientationally ordered are subject to both the crystalline and orientational field, while at the location of the two virtually free rotators the octupolar orientational field vanishes [45, 90]. Methane has isomers with nuclear spin  $I=0$  (para),  $I=1$  (ortho) and  $I=2$  (meta). Constraints on the symmetry of the total wave function of CH<sub>4</sub> upon exchange of protons determine the pairing of nuclear spin states and rotational states, see Figure 11. Differently from the well known case of molecular hydrogen where the odd (ortho) and even (para) rotational states form almost independent populations of rotational levels due to the lack of an easy path to nuclear spin conversion, in methane, the close proximity in the energy of certain rotational levels and intermolecular magnetic interactions make the conversion possible in reasonable laboratory timescales.

There have been numerous studies of the NSC in CH<sub>4</sub> in noble gas matrices and in parahydrogen matrices (see [81] and [56] and references cited therein). Several techniques were used to measure the NSC in solid CH<sub>4</sub>: NMR [15], thermal conductivity [66], neutron scattering [32], and infrared spectroscopy [56, 82, 80]. The requirement on the symmetry of the wave function pins rotational levels to nuclear spins. This makes infrared spectroscopy a good tool to probe the spin populations of each isomer via measurements of ro-vibrational transitions. From the intensity of

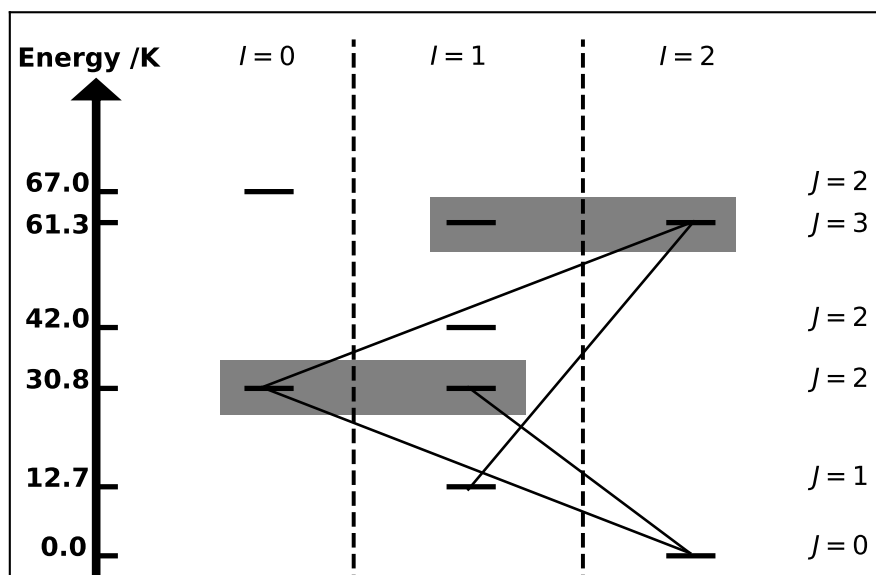


Figure 11: Energy diagram of rotational levels ( $J$ ) in solid CH<sub>4</sub> for different nuclear spin isomers (I). Levels of nuclear-spin isomers are shown by bold solid lines. The rotation levels are coupled by the nuclear spin- nuclear spin interaction (connected by solid line) and nuclear spin- rotation interaction. In addition to these intramolecular magnetic interactions, the  $J = 2$  and  $J = 3$  levels are degenerate with respect to  $I$ (outlined inside gray box). Adapted from [56, 82].

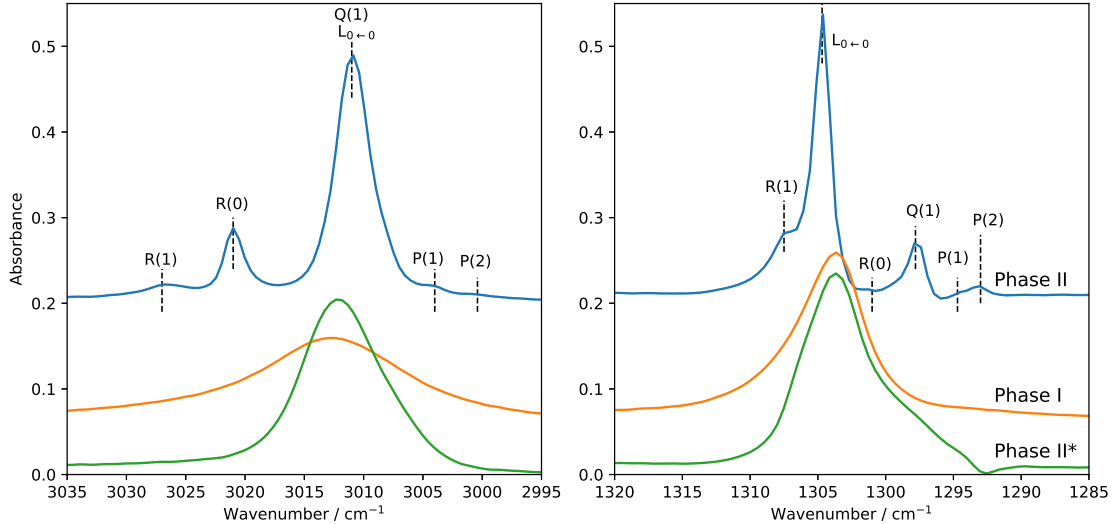


Figure 12: FTIR spectra of solid methane in the  $\nu_3$  and  $\nu_4$  vibrational modes at a resolution of  $1.0 \text{ cm}^{-1}$ . All the traces are from the same experiment at different time frames and temperatures. For each panel, the bottom one represents methane solid deposited at 6 K. The middle one shows the spectrum of the deposited methane solid heated to and annealed at 30 K. Finally, the top one represents 30 K annealed methane solid cooled down to 6 K.

the bands vs. time, the rate of conversion  $k$  at a given temperature  $T$  can be obtained:

$$I(t) = I_\infty + Ae^{-kt} \quad (3.1)$$

Previous IR experiments showed that cooling solid methane from Phase I to Phase II produces additional IR peaks in  $\nu_3$  (asymmetric stretching) and  $\nu_4$  (bending) bands [56, 82, 80]. These have been attributed to rotational transitions following nuclear spin conversion (NSC); they are usually labeled in the spectroscopic notation as P(J), Q(J), and R(J), see Figure 1 and Figure 2 in Sugimoto et al. [80]. Grieger et al. [32] found that their neutron scattering data and data from other sources could be best fitted with an expression that gives the rate of conversion in solid  $\text{CH}_4$  at the temperature  $T$  as:

$$R = A\left(1 + \frac{2}{e^{\frac{E}{T}} - 1}\right) + Be^{-\frac{C}{T}} \quad (3.2)$$

where  $E$  is the energy required for the transition  $J = 1 \leftarrow 0$  in one phonon process;  $A$ ,  $B$  and  $C$  are fitting parameters. In this equation, the thermally activated term was added to the one-phonon process evaluated by Nijman and Berlinsky [58]. The thermal activated term is an Orbach-type process of absorption/emission of a phonon through an intermediate state. Energies are given in units of K.

In solid methane, this measurement is a bit challenging because some energy levels are close and the transition can be rapid. As pointed out by Sugimoto et al. [82], the expression for the rate Eq.(3.1) might not capture the change of intensity, especially on a short timescale and for the R(1) band. Based on a simple model taking into account the occupation of the lowest rotational levels, they proposed to fit data in the 5-7 K range with a double exponential:

$$I_X(t) = I_{\infty,X} + A_{1,X}e^{-k_1t} + A_{2,X}e^{-k_2t} \quad (3.3)$$

where X stands for the R(0) transition. The characterization of solid methane must also include the characterization of kinetic pathways to its formation and transformation, since this aspect intervenes in the formation of methane in the natural world and opens the way to investigate the kinetics of ordering of low temperature molecular solids. This has applications also in space physics, where, depending on the environment, amorphous and crystalline ices are present, and the thermal history of ices is important to understand the chemical evolution of interstellar environments surrounding protostars.

In this contribution, we first look at the IR spectra of solid methane prepared under different conditions. We find there is a new metastable solid phase for solid methane deposited at low temperature ( $\sim 6$  K). Then we introduce a quantitative analysis method of the  $\nu_3$  and  $\nu_4$  bands to characterize the degree of disorder. We apply this analysis to the study of transitions between Phase I and Phase II, and between the metastable phase and Phase II. Finally, we show evidence of NSC in all these solids; we measure the rates of conversion and obtain characteristic energies for the transitions.

### 3.3 Experimental methods

A detailed description UHV apparatus is given in Chapter 2 of this thesis as well as prior published works [37]; here only the main features that are relevant to this study are summarized. Methane ices were grown on the sample disk by introducing methane through a stepper motor controlled UHV precision leak valve. A LabVIEW program controlled the rate of the deposition and the thickness of the deposit. In all experiments, 100 monolayer (ML, defined as  $10^{15}$  molecules/cm<sup>2</sup>) of ice were formed at a relatively high deposition rate of 100 ML per minute. This deposition dose was calculated using the impingement rate, see Chapter 2 for details. In most of the experiments, methane was deposited at 6 K or 30 K. The ice was then brought to the desired temperature (6, 7, 8, 9, 10, and 11 K) in less than 30 seconds. Spectra were measured and averaged every 20 seconds at a resolution of 1 cm<sup>-1</sup>. To measure the NSC, the IR spectra were continuously monitored at a fixed temperature for different lengths of time, depending on the features being measured. For

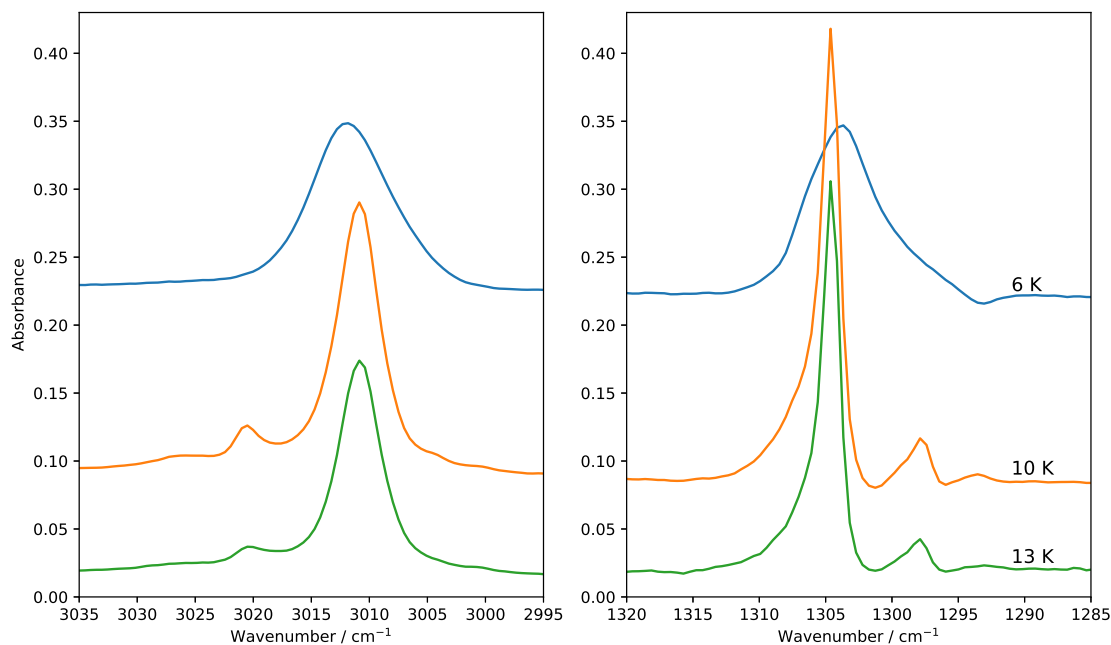


Figure 13: FTIR spectra of solid methane in the  $\nu_3$  and  $\nu_4$  vibrational modes at a resolution of  $1.0 \text{ cm}^{-1}$  right after deposition at 6 K, 10 K, and 13 K. See text for additional details.

example, the isothermal experiments in which the ice was brought and kept at 8 K and 11 K from the deposition temperature of 6 K, lasted approximately twelve and two hours, respectively. In other experiments, the ice was deposited at 6 K, annealed for several minutes, and then heated at  $0.3 \text{ K/min}$  to 30 K in one set and to 12 K in another, then annealed for another several minutes and cooled at  $0.3 \text{ K/min}$  back to 6 K.

### 3.4 Results and Analysis

We carried out two sets of experiments. In the first set, we studied the temperature dependence of IR absorption bands of pure methane deposited at 6 K and heated and cooled cyclically between 6 to 12 K (within Phase II) and between 6 to 30 K (from Phase II to Phase I). In the second set, we kept the same deposition temperature, coverage, and deposition rate and carried out isothermal experiments at temperatures between 6 to 11 K, all within Phase II. We verified that even when the  $\text{CH}_4$  ice is deposited at 6 K and kept at 6 K for as long as 18 hours, there is an insignificant change in the  $\text{CH}_4$  ice structure as seen from the IR spectrum. Therefore, the exact time the ice spent at 6 K does not affect our experimental results.

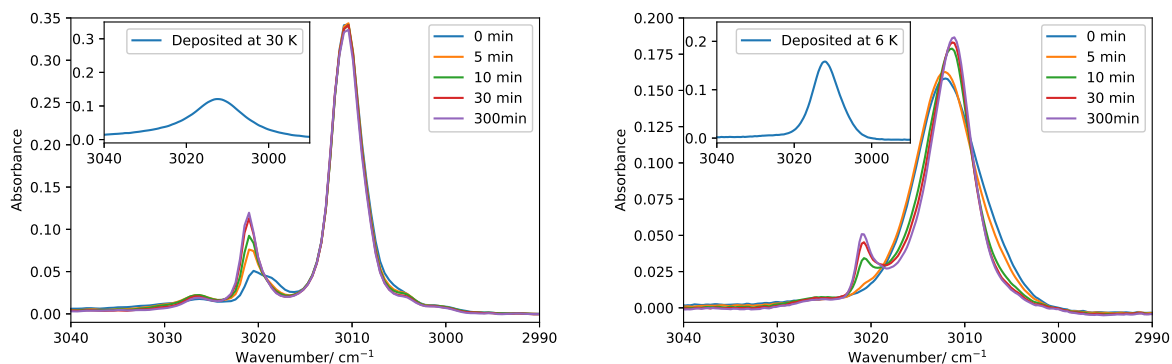


Figure 14: Comparison of  $\nu_3$  mode of solid methane, deposited at 30 K (left) and at 6 K (right); traces are recorded at 8 K for up to 300 minutes.

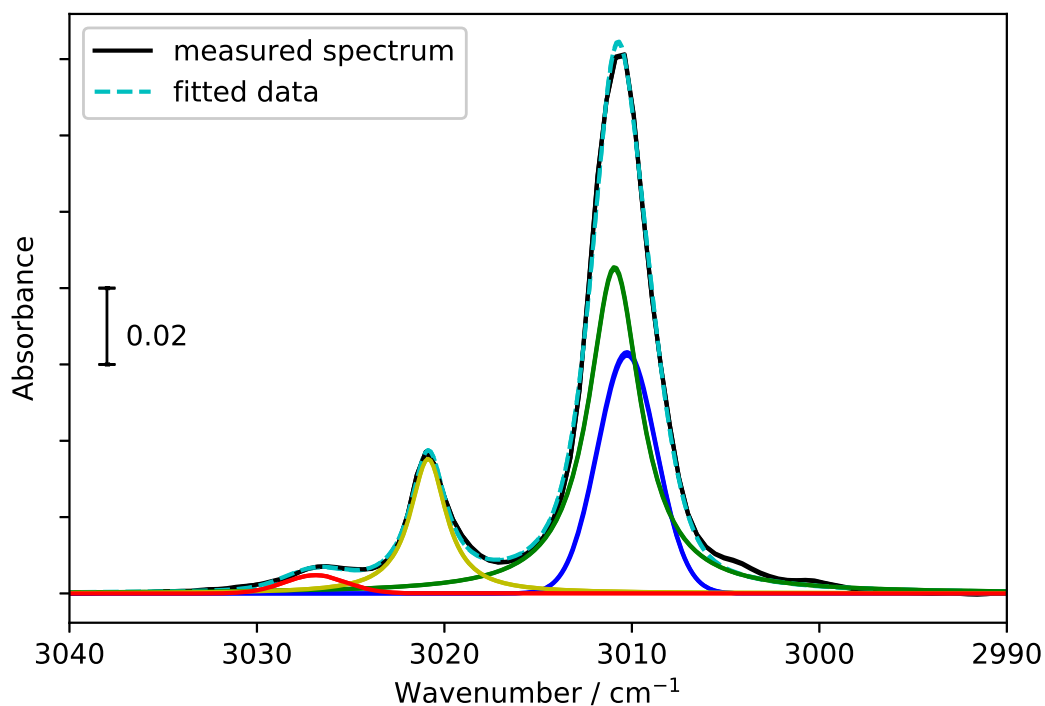


Figure 15: Illustration of the fitting method used in the analysis. Each absorption feature in the spectrum is fitted with two functions, a Lorentzian and a Gaussian. Out of four fitted curve, the two Lorentzian functions (green and yellow) represent  $L_{0\leftarrow 0}$  and  $R(0)$  peaks. Two Gaussian functions (blue and red) represent  $Q(1)$  and  $R(1)$  peaks, respectively.

### 3.4.1 FTIR absorption spectra of $\nu_3$ and $\nu_4$ modes

Figure 12 shows the  $\nu_3$  (bending mode) and  $\nu_4$  (stretching mode) of methane in the two different crystalline phases. In each panel, the middle trace shows methane after it has been brought to and held at 30 K for 10 minutes. At this temperature, solid methane is in Phase I, an fcc lattice with orientational disorder [45, 90]. The top trace is obtained by cooling the sample to 6 K and holding it for 30 minutes. Here methane is in Phase II, in which six of the eight molecules in the unit cell are orientationally ordered, while the other two are virtually rotationally free. Both phases have been seen and identified before (see [80, 81] and referenced cited therein). The emergence of additional features in the top traces is due to NSC and is explained in the later half of the paper. The bottom traces in both panels of Figure 12 show absorption feature of methane that haven't been reported before. We attribute them to partially orientationally ordered Phase II and we label it as Phase II\*. Figure 13 shows the  $\nu_3$  and  $\nu_4$  modes of methane as deposited at 6 K, 10 K, and 13 K. In each panel, the top trace is recorded right after deposition of methane at 6 K. At this temperature methane is in partially orientationally ordered Phase II as in the bottom traces of Figure 12. At this temperature, there is little to no change of the IR spectrum even after the deposited methane is kept at 6 K as long as 18 hours. The middle and bottom traces are obtained by depositing methane at 10 K and 13 K, respectively. At these temperatures, methane is in Phase II right at the moment of deposition.

In Phase II, there is the emergence of new bands near both the  $\nu_3$  and  $\nu_4$  modes as shown in the top curve of Figure 12. In the case of the  $\nu_3$  mode, we assigned the peaks as follows [80]:  $3000.6 \text{ cm}^{-1}$  (P(2)),  $3004.1 \text{ cm}^{-1}$  (P(1)),  $3021.0 \text{ cm}^{-1}$  (R(0)), and  $3026.6 \text{ cm}^{-1}$  (R(1)). The molecules in the  $D_{2d}$  symmetry sites are responsible for the  $L_{0\leftarrow 0}$  transition [18]. This transition and Q(1) of the free rotators ( $O_h$ ) are not resolved in the main peak centered at  $3010.9 \text{ cm}^{-1}$ , in contrast to that of Ref [80]. In the  $\nu_4$  mode region we detect P(2), P(1), Q(1), R(0), and R(1) at  $1293.2$ ,  $1294.4$ ,  $1297.8$ ,  $1301.2$  and  $1307.3 \text{ cm}^{-1}$ , respectively. We observe  $L_{0\leftarrow 0}$  for  $\nu_4$  at  $1304.8 \text{ cm}^{-1}$  which agrees with the assignment made by Chapados and Cabana [18], except for a blue shift of  $3.5 \text{ cm}^{-1}$ . (Note: it appears that all peaks in [18] are blue shifted by  $\geq 3.5 \text{ cm}^{-1}$ ). Therefore, the assignment of  $L_{0\leftarrow 0}$  is different than that of Sugimoto et al. [80] in which it is claimed that  $L_{0\leftarrow 0}$  peak is merged with the Q(1) peak, and thus unresolved. Since the  $L_{0\leftarrow 0}$  transition is attributed to the molecules in  $D_{2d}$ , one should expect significant changes in peak position and strength since those molecules become free rotators during the transition from Phase II to Phase I. Our data shows that the peak  $L_{0\leftarrow 0}$  at  $1304.8 \text{ cm}^{-1}$  in the  $\nu_4$  region and the unresolved peaks of  $L_{0\leftarrow 0}$  and Q(1) in the  $\nu_3$  region change significantly during the phase change.

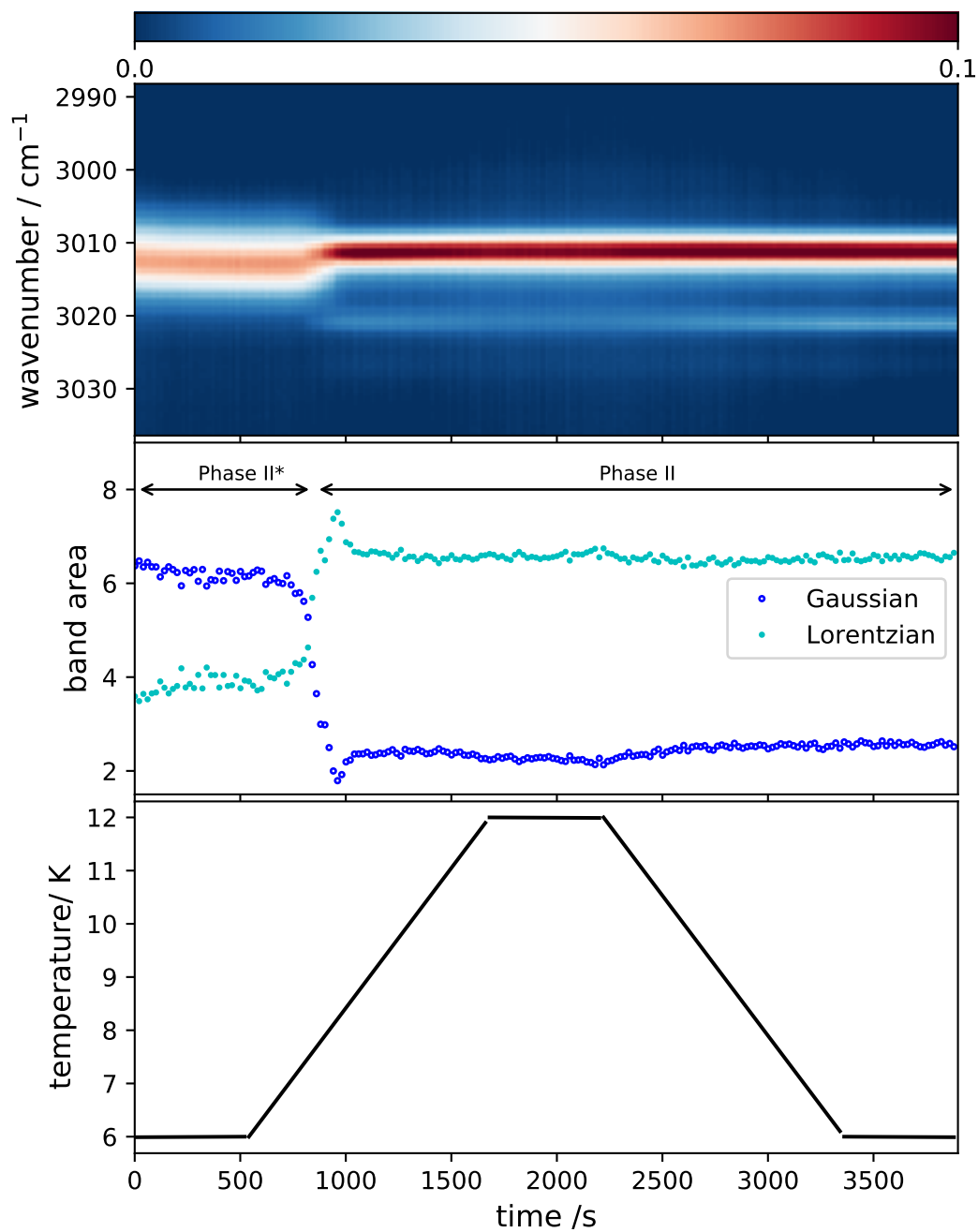


Figure 16: The  $\nu_3$  mode during a heating and cooling cycle in the 6 - 12 K temperature range. The three panels show the intensity map (top), the band area of the Gaussian and Lorentzian components (middle), and the temperature ramp (bottom). The horizontal color scale bar on top of the figure shows the relative strength on the 0-0.1 scale in the intensity plot.

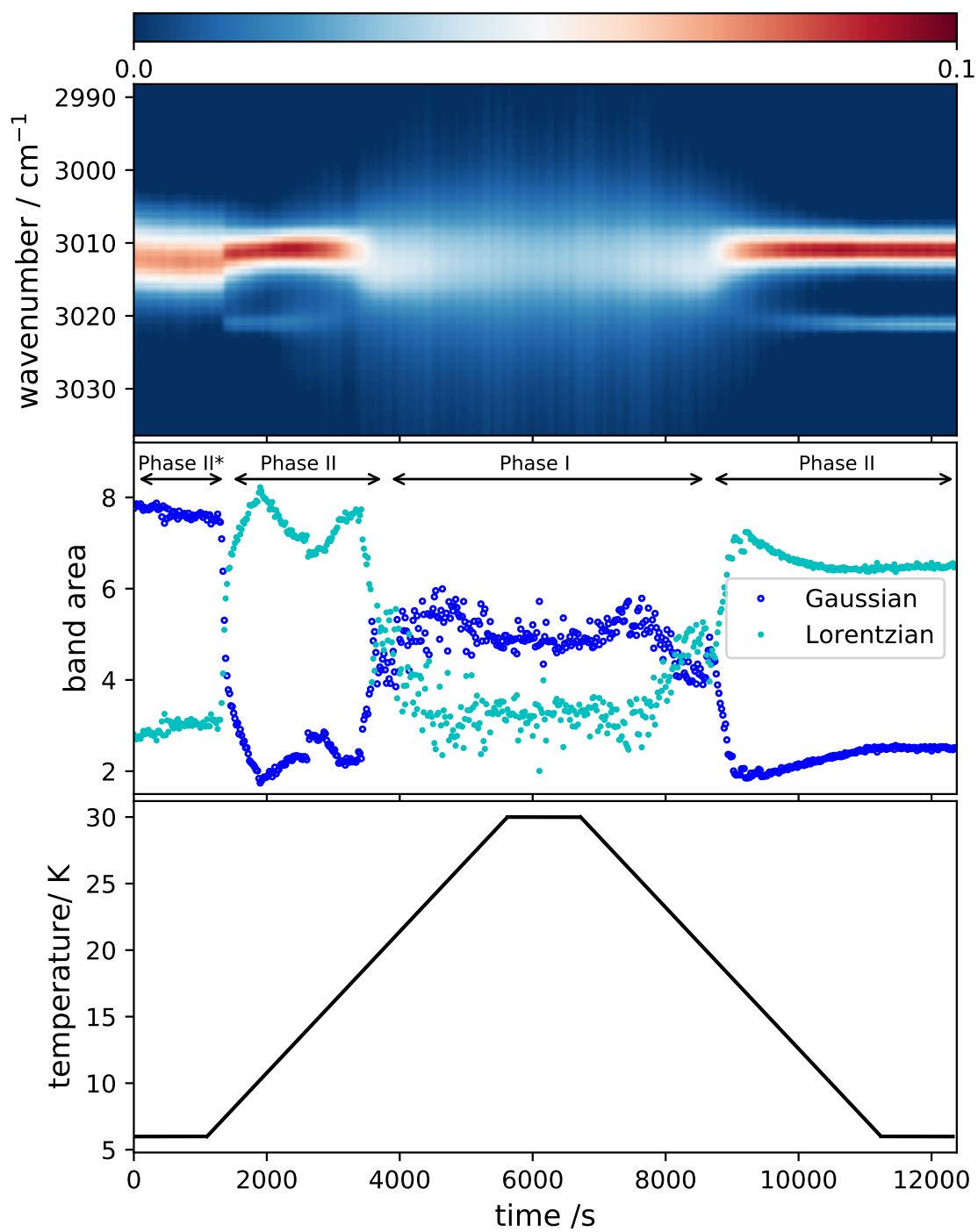


Figure 17: As in Figure 16, but in the 6 - 30 K temperature range

### 3.4.2 The $\nu_3$ mode of methane ice grown at 6 K and 30 K

When methane is first deposited at 6 K, we obtain the bottom traces shown in both panels of Figure 12. Even after leaving the ice for an extended period of time, no additional peaks (such as the ones shown in the bottom traces of both panels of Figure 12) develop. This is contrary to the expectation of a methane ice in Phase II. We argue that this is a different, metastable phase, Phase II\*. In Figure 14 we compare the time evolution of the  $\nu_3$  mode measured at 8 K and obtained by deposition at 30 K, left panel, and at 6 K, right panel. For the 30 K deposited ice we see already resolved peaks of R(0), R(1), P(0) and P(1), indicating that the ice is in phase II at  $t=0$  at 8 K. Notice that the central peak that is associated with the  $L_{0\leftarrow 0}$  transition does not change in the 0 to 300 minutes interval. On the other hand, for the 6 K deposited ice, the central peak changes with time and becomes sharper. Since the central peak contains the  $L_{0\leftarrow 0}$  transition due to the molecules in the  $D_{2d}$  symmetry lattice, we propose that the sharpening is due to a transition from Phase II\* to Phase II where molecules become ordered in the  $D_{2d}$  lattice. The Phase II\* cannot be restored once the system has been brought to Phase II. An ice prepared in Phase II and cooled to 6 K remains in such phase.

### 3.4.3 Phase change from II\* to II

In this section we explore the kinetics of the phase change from Phase II\* to Phase II. Most of the analysis is done in the  $\nu_3$  region, since peaks near  $\nu_4$  mode show blending. Each peak was fitted with a Gaussian and Lorentzian spectral line shape. We assign the Gaussian component to orientationally disordered molecules, as shown from peak analysis reported below. P(1) and P(2) were not fitted because they are too small. A sample of the fitting is given in Figure 15.

In Figures 16 and 17 we plotted three sections of the heat up and cool down cycle: a) intensity map of all the IR spectrum collected in that time frame, b) the area of the Gaussian and Lorentzian components of the fitting for two heating and cooling experiments and c) the temperature ramp. In the first experiment, we deposited methane at 6 K, and then did a heating/cooling cycle between 6 to 12 K at 0.3 K/min. In the middle panel of Figure 16 we see that there is a crossover between Gaussian and Lorentz components at around 850 s ( $\simeq 8$  K), which corresponds to the time when there is a change in the intensity map of the  $\nu_3$  mode (top panel of Figure 16). This change is irreversible, as shown in the cooling part of the plot. The decrease of the area of the Gaussian component means that there is an orientational ordering of molecules in the  $D_{2d}$  lattice.

In the second experiment, the heating/cooling cycle was extended to 30 K. In this case, methane ice goes through a first change (Phase II\* to Phase II at 1400 s ( $\simeq 8$  K) in Figure 17) as in the first experiment. Then there is a change from Phase II to Phase I in which the Gaussian component

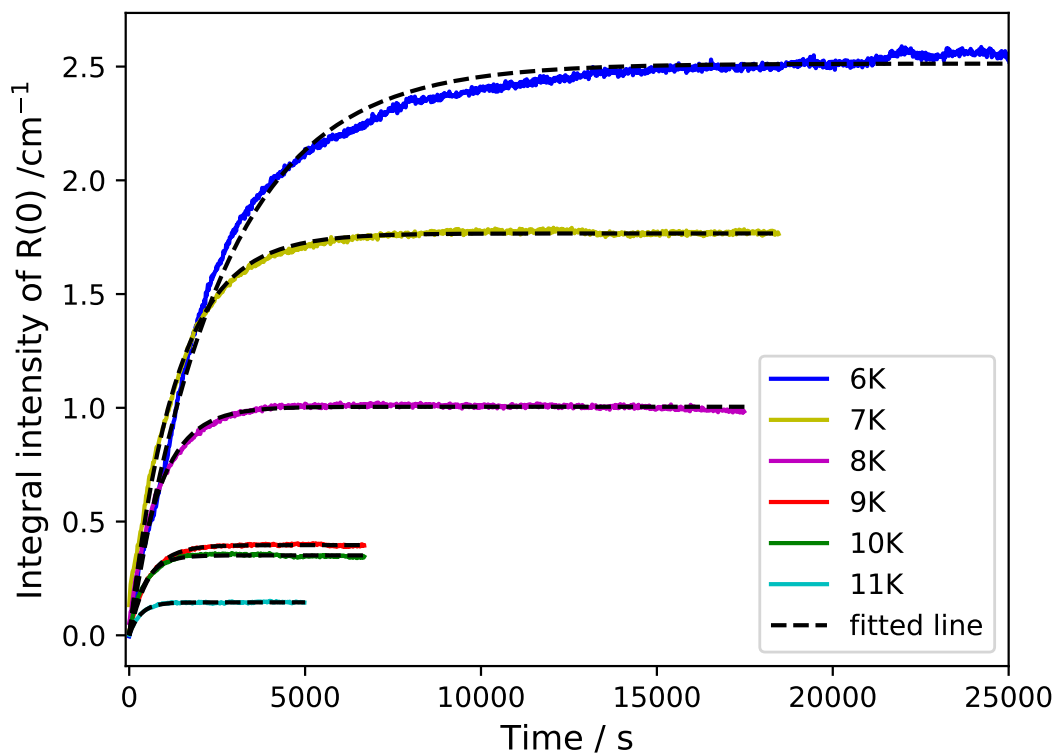


Figure 18: Temporal change of the integral intensities of R(0) at different temperatures for methane deposited at 30 K. The dotted lines indicate the results of fitting with Eq. 3.1. For clarity's sake  $I_\infty$  has been subtracted from each curve.

becomes strong again (in Phase I all molecules are free rotators). As seen from Figure 17, the transition between Phase I and II is reversible, but there is no transition back to Phase II\*.

### 3.4.4 Calculation of the Nuclear Spin Conversion (NSC) rate

Table 2: Parameters in the analysis of the R(0) and R(1) bands

assignment	variable	dep. temp.	temp. range	A/ hr <sup>-1</sup>	B/ hr <sup>-1</sup>	C /K
R(0)	k	30 K	6.0 to 11.0 K	0.51± 0.31	215± 61	33.7±3.6
R(1)	k <sub>1</sub>		6.0 to 11.0 K		91± 85	27.5±9.2
	k <sub>2</sub>		6.0 to 10.0 K		6290± 3100	42.7± 4.6
R(0)	k	6 K	7.2 to 8.5 K		6560± 280	61.6±3.6
	k		8.5 to 11.0 K		32.6± 9.6	16.5±2.9

The rate of NSC in the CH<sub>4</sub> ice is a function of temperature, as is given by Eq. 3.2. According to Miyamoto et al. [56] the first term in the right side of the equation is the rate due to one phonon process [58], which is dominant for  $T \leq 4$  K; the second term is larger at higher temperature and is the two-phonon Orbach process. The relaxation rate of the NSC can be calculated by fitting the data with Eq. 3.1. We have calculated the NSC rate for two sets of ices. The first set of ices were deposited at 30 K; they were annealed for 10 min and then cool to the desired temperature within 30 s. For the second set we deposited the ice at 6 K at then immediately heated to the desired temperature at a rate of 12 K/min. The temporal change of integral intensity (after subtraction from the initial value) of the R(0) peak and their fitted lines are shown in Figure 18 for different values of the temperature in the isotherm experiments. In Eq. 3.2 we took the value of  $E=12.7$  K from Grieger et al. [32]'s. To obtain that value they used their data and data from a compilation of experimental results of prior experiments by other authors. Since we cannot cool down our sample to lower than 5.0 K, we cannot obtain the value for the parameter  $A$  in Eq. 3.2 from our data. Sugimoto et al. [80] mentioned that they used the value of  $A=(0.81 \pm 0.27) \text{ h}^{-1}$  from Grieger et al. [32]. However, Grieger et al. [32] did their experiments in an adiabatic helium cell while both we and Sugimoto et al. [80] did our respective experiments using thin films; it is not clear whether the value of  $A$  would be the same as the Grieger et al. [32]'s. In our analysis we fitted the relaxation

rate of R(0) from 6 K to 11 K for 30 K deposited ice using non-linear fitting and calculated the variables  $A$ ,  $B$  and  $C$  (listed in Table 2). The data and the fitted curve are shown in Figure 19 as, respectively, red dots and the solid red line both plots in the main and inset figures. Later we kept the  $A = (0.51 \pm 0.31) \text{ h}^{-1}$  constant and fitted other set of data (6 K deposited ice and R(1) of 30 K deposited ice) through non-linear fitting and obtained the values for  $B$  and  $C$  (listed in Table 2).

For the ice deposited at 6 K (main plot in Figure 19), we see two trends in the NSC. For temperature up to 7.0 K, the relaxation rate is very small and almost no change occurs in the ice. At 7.0 K one has to wait for approximately one and a half hours to see the first significant change in the relaxation rate. Once the ice reaches 7.2 K, we see a significant rise in the relaxation rate up to 8.5 K. Those data are labeled as blue stars in Figure 19; the broken blue line is a fit using Eq. 3.2. Beyond 8.5 K we see another trend in the relaxation rate (black triangles). The grayed lines show the trends past the data. Therefore, we conclude that 8.5 K is a critical temperature for methane ice deposited at  $\leq 7$  K; this is in agreement with the analysis of peak shapes presented above. The activation energy for the Orbach process in Phase II\* is  $61.6 \pm 3.6$  K (Table 2).

Recently, Sugimoto et al. [82] suggested that the use of Eq. 3.1 to fit the change of the peak area vs. time might not be entirely applicable for a system of more than two spin isomers. Using a much faster cooling from 30 K to 5 K to prepare their samples than they used in a previous work, they found that their data in the 5 to 7 K range can be fit using :

$$I(t) = I_{\infty} + A_1 e^{-k_1 t} + A_2 e^{-k_2 t} \quad (3.4)$$

We found that bi-exponential fitting is only necessary for isotherms of R(1) peak deposited at 30 K, but not for R(0), since the fit with one exponential is excellent (see Figure 18). A sample comparison of R(0) and R(1) in the 8 K isotherm is shown in Figure 20 in which red dots represent the integral intensity of R(0) and the green dots represent the integral intensity of R(1) during a 8 K isotherm. The values of  $k_2$  are plotted as green squares in the inset of Figure 19. The cyan triangles represent  $k_1$  calculated from R(1). The values of the relaxation variables  $k_1$  and  $k_2$  of R(1) are listed in Table 2.

### 3.5 Summary

We have characterized the low temperature phases of solid methane obtained by deposition at 6 K and 30 K. We discovered a new metastable state of solid methane when the methane ice is grown at  $\leq 7$  K. By comparing the IR features with the ones of the equilibrium phases, we suggest that this phase likely consists of a crystal with orientational ordering in between Phase I and Phase II.

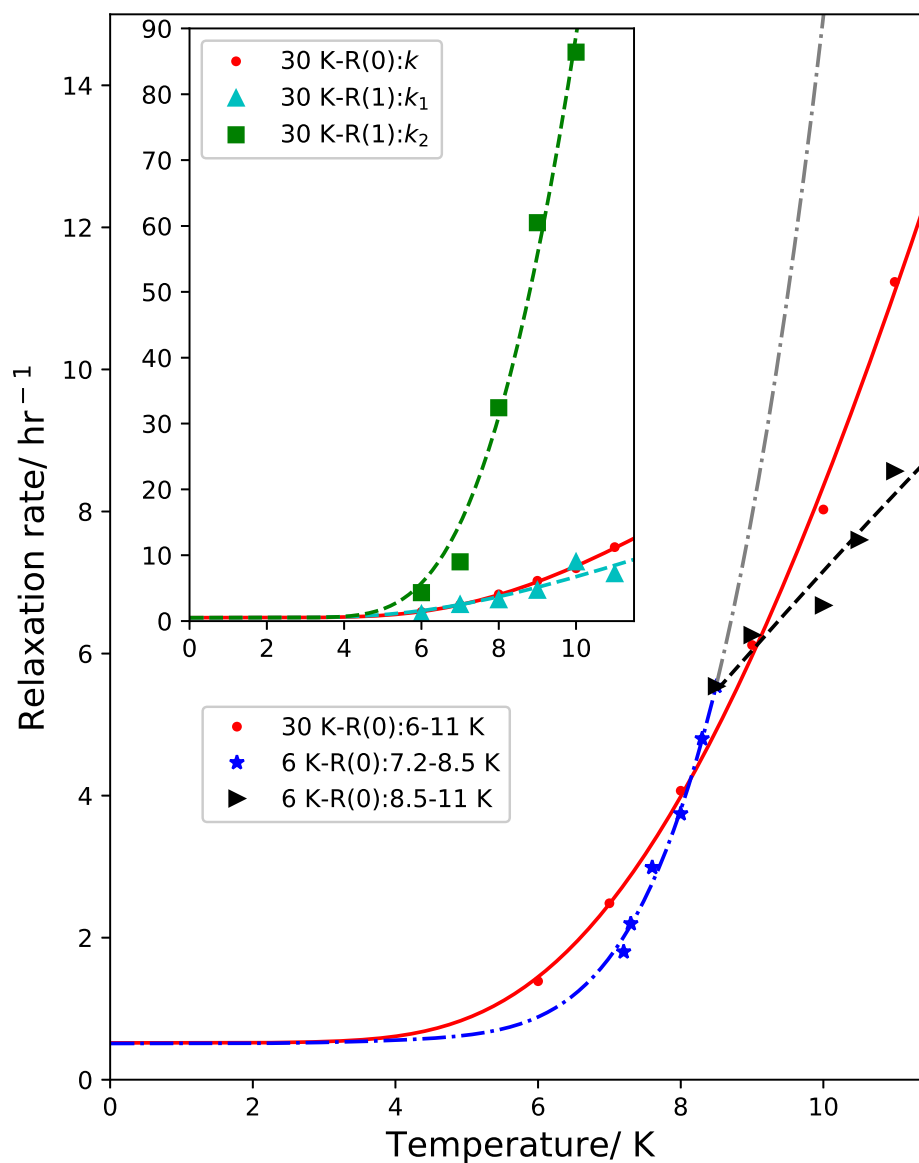


Figure 19: Temperature dependence of the relaxation rates of  $R(0)$  and  $R(1)$  for ice deposited at 6 K and at 30 K. Main plot: Blue stars and black triangles show the rates for  $J = 0(R(0))$  between, respectively, 7.2 K and 8.5 K and between 8.5 K to 11.0 K for solid methane deposited at 6K. The red dots show the rates for solid methane deposited at 30 K. In the inset: green squares and cyan triangles show rates for  $J = 1(R(1))$  for solid methane deposited at 30 K. Solid, dashed, and dash-dotted curves show fitting of data using Eq. 3.2

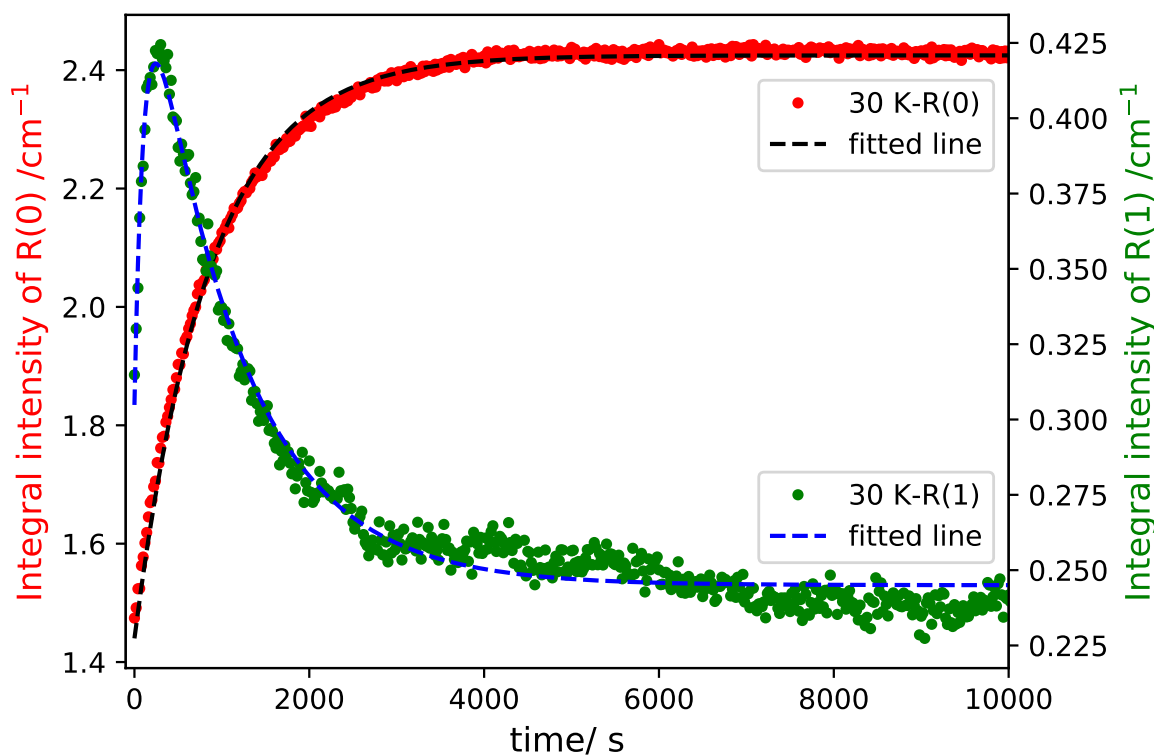


Figure 20: Temporal change of the integral intensity of R(0) (red) and R(1) (green) at 8 K for solid methane deposited at 30 K. The dotted lines indicate the results of fitted function for R(0) with Eq. 3.1 for R(0) and Eq. 3.4 for R(1) ]

The metastable phase becomes Phase II when the ice is brought past 8.5 K.

We measured NSC using the IR bands of R(0) and R(1). Using Eq.3.3 and  $k$  values from temporal measurements of R(0), we obtained the activation energy for the Orbach process, in good agreement with the energy of the transition between rotational level  $J=0$  ( $I=2$ ) and the intermediate level  $J=2$  ( $I=1$ ). The relaxation rates of R(0) and R(1), long time behaviour, for  $\nu_3$  mode at 7 K are  $2.48 \pm 0.18 \text{ hr}^{-1}$  and  $2.52 \pm 0.32 \text{ hr}^{-1}$ . The calculated relaxation rates are close to the values obtained by Sugimoto et al. [80],  $3.24 \pm 0.19 \text{ hr}^{-1}$  and  $2.92 \pm 0.21 \text{ hr}^{-1}$  for methane solid deposited at 30 K. The activation energy for the Orbach process ( $\Delta = 33.7 \pm 3.6 \text{ K}$ ) is in good agreement with the one obtained by Sugimoto et al. [80],  $\Delta = 35.3 \pm 4.4 \text{ K}$ . When using R(1) data, we employed the fitting equation 3.4 suggested by Sugimoto et al. [82]. We extended the range of  $k_2$  values from the 5-7 K range of Sugimoto et al. [82] to the 6 to 11.0 K range. This has allowed us to obtain the activation energy of the Orbach process for this transition.

The metastable phase upon heating from 6 K yields a NRC that is characterized by two activation energies, one for 7.2-8.5 K and another for  $T > 8.5 \text{ K}$ . The limited temperature range over which NSC can be observed in laboratory timescales (7.2-8.5 K) prevents us from drawing firm conclusions on the relaxation process for this metastable phase. If the rise of the relaxation rate below 8.5 K is due to the Orbach process, the high value of  $\Delta \simeq 61 \text{ K}$  would imply an intermediate state such as  $J=2$  ( $I=0$ ). Given the high value of  $\Delta$ , a two-phonon Raman process through a virtual state is also possible [73].

## Chapter 4

# Infrared Spectroscopic Study of Crystalline Methane Solid and Methane Mixture with Polar and Non-polar Molecules

### 4.1 Abstract

Methane ice, whether pure or in mixtures with polar ( $\text{H}_2\text{O}$ ) and non-polar ( $\text{N}_2$ ) molecules, is found in interstellar space as well as in outer solar system bodies. Nuclear Spin Conversion (NSC), crystalline structures, and the transition temperature between solid-state phases can be affected by the presence of polar and non-polar molecules ( $\text{H}_2\text{O}$  and  $\text{N}_2$ ), deposition temperature, and deposition rate. Specifically, we found a relationship between the thickness and the solid-state ordering transformation in methane thin films. A new study of NSC of pure  $\text{CH}_4$  ice and of  $\text{CH}_4:\text{H}_2\text{O}$  ice mixture at 7 K is placed in relation to segregation of  $\text{H}_2\text{O}$  using methane IR inactive  $\nu_1$  and  $\nu_2$  modes. The diffusion of  $\text{N}_2$  and  $\text{CH}_4$  in  $\text{CH}_4:\text{N}_2$  ice mixture with temperature cycling has also been studied in order to obtain a relation between IR features and state of aggregation of the ice. With the launch of the James Webb Space Telescope (JWST), IR data of fundamental vibrational modes of  $\text{CH}_4$  ice and its mixture with volatiles will be accessible to study the aggregation and thermal history of volatiles in interstellar and planetary ices. Mid-IR range laboratory data of the fundamental vibrational modes of  $\text{CH}_4$  ice and its mixture with volatiles will become essential in the analysis of observational data from JWST.

## 4.2 Introduction

Methane is the simplest example of a hydrocarbon molecule. In solid form, methane and its mixtures with other volatiles are important candidates for laboratory studies as they are present in ocean beds as clathrate hydrates [70], in solar system bodies [84], interstellar ices [14, 12, 59, 1], and comets [11]. In particular, methane ice has been detected in different solar system bodies either as pure and or mixed with other molecules at different mixing ratios. Until today, most of the infrared planetary methane ice data are based on near-IR ( $\nu=10000-4000\text{ cm}^{-1}$  ;  $\lambda = 1.0-2.5\text{ }\mu\text{m}$ ) spectrum. But, the James Webb Space Telescope will initiate a new era of planetary ice exploration in the Mid-IR ( $\nu=4000-400\text{ cm}^{-1}$  ;  $\lambda = 2.5-25\text{ }\mu\text{m}$ ) range. Overall, laboratory data in the Mid-IR range for methane crystalline phases and their transformation in thin films are necessary since there have been very few dedicated studies.

At cryogenic temperature and low pressure, methane solid has two crystalline phases. The first one is an orientationally ordered phase (Phase II) - which can be found at  $T < 20.4\text{ K}$  in bulk methane ice. The second crystalline phase is an orientationally disordered phase (Phase I) that is at  $T > 20.4\text{ K}$ . Both are fcc solids but with different orientational order of the methane molecules. In addition, methane solid goes through nuclear spin conversion (NSC) at cryogenic temperature [19, 63, 25], see also the preceding chapter. Recently a new metastable phase ( $T < 7.0\text{ K}$ ) of solid methane was reported which is a metastable crystalline phase with an orientational order between Phase II and Phase I [25].

Molecular-level interaction between  $\text{CH}_4$  and  $\text{H}_2\text{O}$  is accompanied by significant shifts in peak positions and spectral features in near [7] and mid-IR [43] spectral regions. In addition to the two fundamental modes  $\nu_3$  and  $\nu_4$ , there are two IR inactive  $\nu_1$  and  $\nu_2$  modes in solid methane [44, 42] in mid-IR range. These modes are only activated in the presence of water in the ice matrix [27, 42]. Water dangling bond sites have been used to calibrate the diffusion rate of volatiles in ASW [37]. Similarly, IR inactive modes of methane can be used to probe the segregation of water in  $\text{CH}_4$  and  $\text{H}_2\text{O}$  ice mixtures.  $\text{CH}_4:\text{N}_2$  ice mixtures are relevant in the planetary system due to their presence in outer solar system bodies [33] and satellites of planets [53]. Blue-shift in near-IR features of methane IR peak positions has been reported for outer solar system bodies  $\text{CH}_4:\text{N}_2$  ice mixtures [68].

The goal of this work is to study IR absorption features of pure methane and methane ice mixture (with  $\text{H}_2\text{O}$  and  $\text{N}_2$ ). We investigated the effect of deposition methods, thermal cycling, NSC, and deposition temperature on thin films of pure methane in UHV conditions. The spectral changes that methane ice experiences in the presence of polar ( $\text{H}_2\text{O}$ ) and non-polar ( $\text{N}_2$ ) molecules were measured. This allowed us to study the segregation and diffusion process of  $\text{CH}_4:\text{H}_2\text{O}$  and

CH<sub>4</sub>:N<sub>2</sub> ice matrices.

### 4.3 Experimental Methods

A detailed description UHV apparatus is given in Chapter 2 of this thesis as well as prior published works [37]; here only the main features that are relevant to this study are summarized. For deposition of CH<sub>4</sub> and H<sub>2</sub>O, two separate UHV precision leak valves were used. Distilled water underwent at least three freeze-pump-thaw cycles before being sent into the chamber. Premixed CH<sub>4</sub> and N<sub>2</sub> gas was deposited using a single UHV leak valve for CH<sub>4</sub>:N<sub>2</sub> mixture deposition. Ices were grown on the sample disk by introducing methane through a stepper motor controlled UHV precision leak valve except for one occasion: a molecular beamline was used to deposit 100 ML CH<sub>4</sub> for the experiment presented in Figure 23. A LabVIEW program controlled the rate of the deposition and the thickness of the deposit. In all experiments, 100 monolayers (ML, defined as 10<sup>15</sup> molecules/cm<sup>2</sup>) of ice were grown at a relatively high deposition rate of 100 ML per minute in the case of deposition from background gas. This deposition dose was calculated using the impingement rate, see Chapter 2 for details. The deposition of methane via the beamline is much slower, by a factor 100.

In most of the experiments, methane was deposited at 10 K, unless otherwise mentioned. A Nicolet 6700 FTIR in the Reflection Absorption Infrared Spectroscopy (RAIRS) configuration with an incident angle of  $\sim 80^\circ$  was used to obtain mid-IR spectra of the ice. Spectra were measured and averaged every 20 seconds at a resolution of 1 cm<sup>-1</sup>. To measure the NSC, the IR spectra were continuously monitored at a fixed temperature for different lengths of time, depending on the features being measured. For example, the isothermal experiments in which the ice was brought and kept at 7 K from the deposition temperature of 30 K, lasted approximately twelve hours. In other experiments, the ice was deposited at 10 K, kept at this temperature for several minutes, and then heated at 3 K/min to the desired temperature and subsequently cooled down to 10 K for temperature cycling experiments.

### 4.4 Results and Analysis

We carried out two sets of experiments. In the first set, we studied the attributes of crystalline phases of methane under different conditions. For these experiments, pure methane ices of different thicknesses were either deposited at 6 or 10 K. Then the methane ice was either kept at a specific temperature for an extended period of time or heated slowly at 3 K/min until the methane

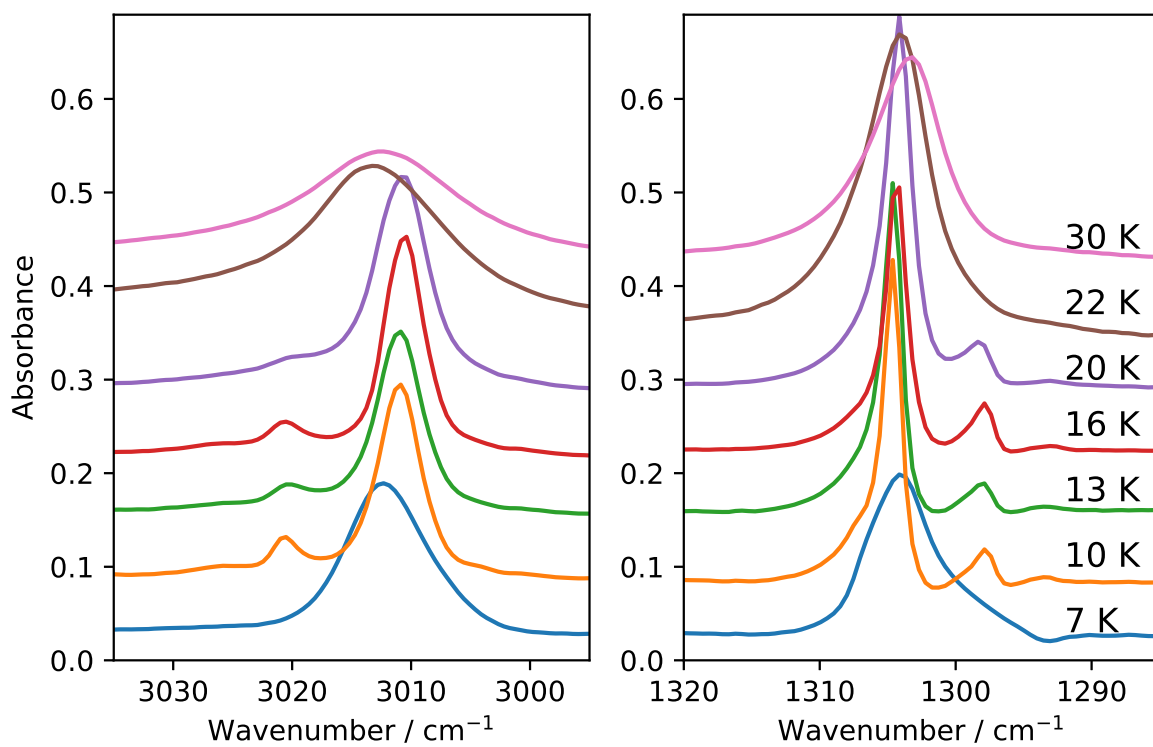


Figure 21: Mid-IR vibrational modes of 100 ML methane ice ( $\nu_3$  (left) and  $\nu_3$  (right)) deposited at 7 K, 10 K, 13 K, 16 K, 20 K, 22 K, and 30 K. The traces are displaced vertically for clarity.

ice desorbed past 40 K. In the second set, methane ice mixed with either water or nitrogen was deposited at 10 K and then the ice went through temperature cycling (heating up and cooling down) to study the changes in IR features during the process.

#### 4.4.1 Methane crystalline phases and deposition temperature

It is a well-established fact that methane has two crystalline fcc phases with a transition temperature of 20.4 K. Most of these experiments of phase transition in methane ice were conducted in a closed-cell [18]. The transition from orientationally ordered phase (Phase II) to orientationally disordered phase (Phase I) is an abrupt process in a closed-cell experiment. On the other hand, from an analysis of methane thin films deposited in the 7-30K range, we observe that the transition from Phase II to Phase I is a relatively slow process. Figure 21 shows the  $\nu_4$  and  $\nu_3$  mode of pure methane ice deposited at different temperatures. At 7 K the ice is in metastable Phase II without the presence of band splitting [25]. For methane deposited at 10K, the ice is in Phase II crystalline methane at 10 K with the fully emerged band splittings due to NSC [25], in agreement with the results presented in the previous chapter. As we raise the deposition temperature we observe that the band splitting gradually diminishes due to the disruption of neighboring lattice sites. We observe that bulk orientational disordering at lattice sites happens in the ice matrix between 20 and 22 K in which the multiple peaks of  $\nu_4$  and  $\nu_3$  modes converge into a single broad peak for each mode. We observe significant blue-shift from  $3010.6 \text{ cm}^{-1}$  to  $3014.2 \text{ cm}^{-1}$  for  $\nu_3$  mode in that temperature range. Beyond 22 K, the ice is an orientationally disordered fcc lattice.

#### 4.4.2 Effect of thickness of CH<sub>4</sub> thin film on phase transition

We deposited 5, 10, 15, 20, and 30 ML of CH<sub>4</sub> on a substrate at 10 K, and then heated the sample from 10 K to 45 K at a rate of 0.1 K/s. The bending mode  $\nu_3$  absorption spectra for all these thicknesses, normalized to the maximum of all the spectra for all the spectra for the same thickness during the heating up process, are shown in Figure 22. When solid methane goes through the orientational phase transition (from Phase II to Phase I) there is a change in the IR peak position and spectral features due to change in the lattice field [80]. (For convenience's sake, we call the phase transition an orientational phase transition irrespective if it goes from an orientational disordered to an orientationally ordered state or vice-versa). In the case of 5 ML coverage, we don't observe any significant pattern in the transition from Phase II to Phase I. At 10 ML coverage the transition temperature of Phase II crystalline ice to Phase I crystalline ice is 23.8 K. In this case, the disruption of neighboring lattice field sites is delayed due to the thinness of the film. On the other hand, for 15ML the transition temperature is a little less than 20.4 K. For coverage of 20 ML

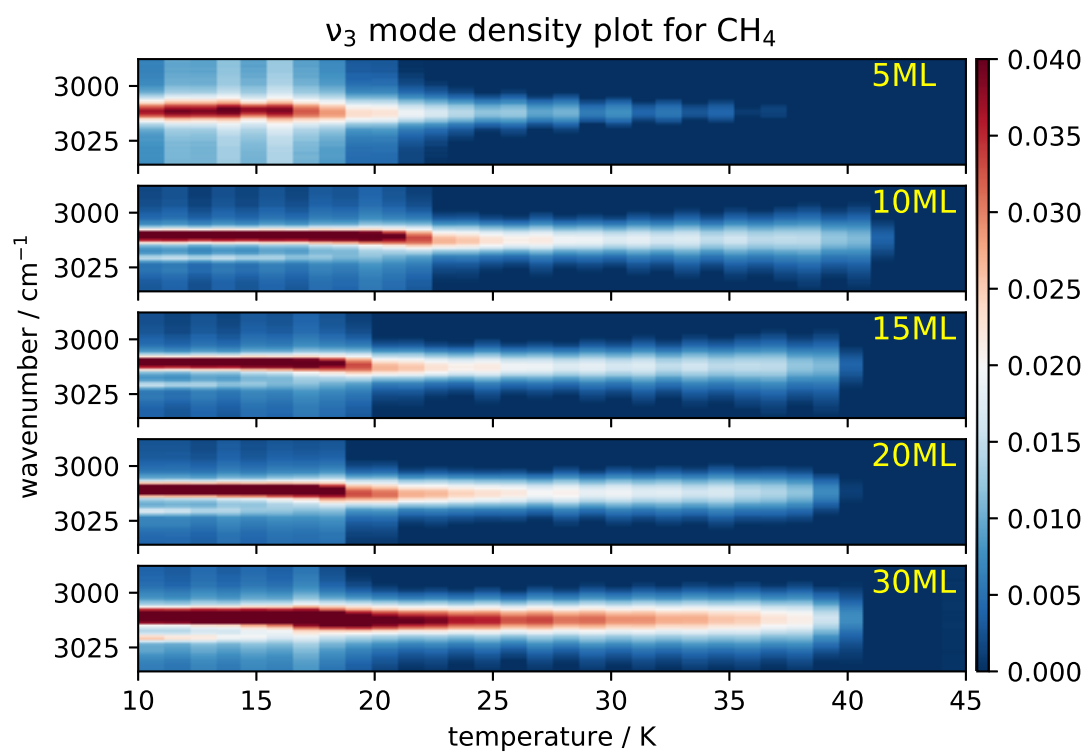


Figure 22: Slow heating up experiment for 5-30 ML of methane ice deposited at 10 K. This diagram shows the relative temperature range for Phase II to Phase I transition of  $\nu_3$  mode for different methane thin film coverage. The absorbance scale is on the right.

and beyond the transition settles down to the bulk value. These experiments suggest that methane ice experiences thin-film effects for coverage below 15 ML. For higher coverage ( $>20$  ML), the ice is independent of thin-film effects.

#### 4.4.3 Effect on NSC of methane ice prepared with two different deposition methods

We know that at 6 K the methane thin film is in a metastable phase where Nuclear Spin Conversion (NSC) is insignificant at that temperature [25], see preceding chapter. As we increase the temperature, and once the temperature reaches beyond 7 K, we observe an exponential increase in the relaxation rate up to 8.5 K. Depending on the deposition method, we found different rates of NSC for methane ice. The top two panels of Figure 23 show 100 ML of methane ice deposited at 6 K and kept for 12 hours; methane gas was deposited filling the chamber through a UHV leak valve. In this background deposited methane ice, we don't see any emergence of band splitting, which is a sign for NSC in IR spectroscopy. On the other hand, the bottom two panels of Figure 23 show 100 ML of methane ice deposited with the molecular beamline; the ice was kept at 6 K for a similar amount of time. In this case, we observe the emergence of band splitting upon the completion of deposition. It takes 100 minutes to finish the deposition through the beamline compared to 1 min using the UHV leak valve. Initially (see bottom two panels), we see emergence of R(0) band ( $3010.9\text{ cm}^{-1}$ ) for  $\nu_3$  mode and Q(1) band ( $1297.8\text{ cm}^{-1}$ ) for  $\nu_4$  mode. As we keep the ice at 6 K for 12 hours we see that the band splitting becomes more pronounced with time. In the ice prepared slowly, orientational ordering at lattice sites takes place; therefore, we see a significant rate of NSC even at 6 K. This fact further strengthens our argument that at 6 K we observe a metastable phase of methane which is a crystalline phase with an orientational ordering between Phase I and Phase II [25].

#### 4.4.4 Methane and water ice mixture with different ratios

Figure 24 shows IR data of  $\nu_4$  and  $\nu_3$  modes of pure methane and methane-water mixture with different mixing ratios. We observe significant change in IR features and FWHM values as water is introduced in the methane ice matrix. For  $\text{CH}_4:\text{H}_2\text{O}(=95:5)$  we observe the peak position is red-shifted by  $0.8\text{ cm}^{-1}$  and  $0.7\text{ cm}^{-1}$  for  $\nu_4$  and  $\nu_3$ , respectively. The FWHM becomes  $14\text{ cm}^{-1}$  for  $\nu_4$  and  $\nu_3$  modes, which is a significant increase from pure methane. The red-shift in peak position is more significant for  $\nu_3$  than for the  $\nu_4$  mode. All the relevant values are listed in Table 3.

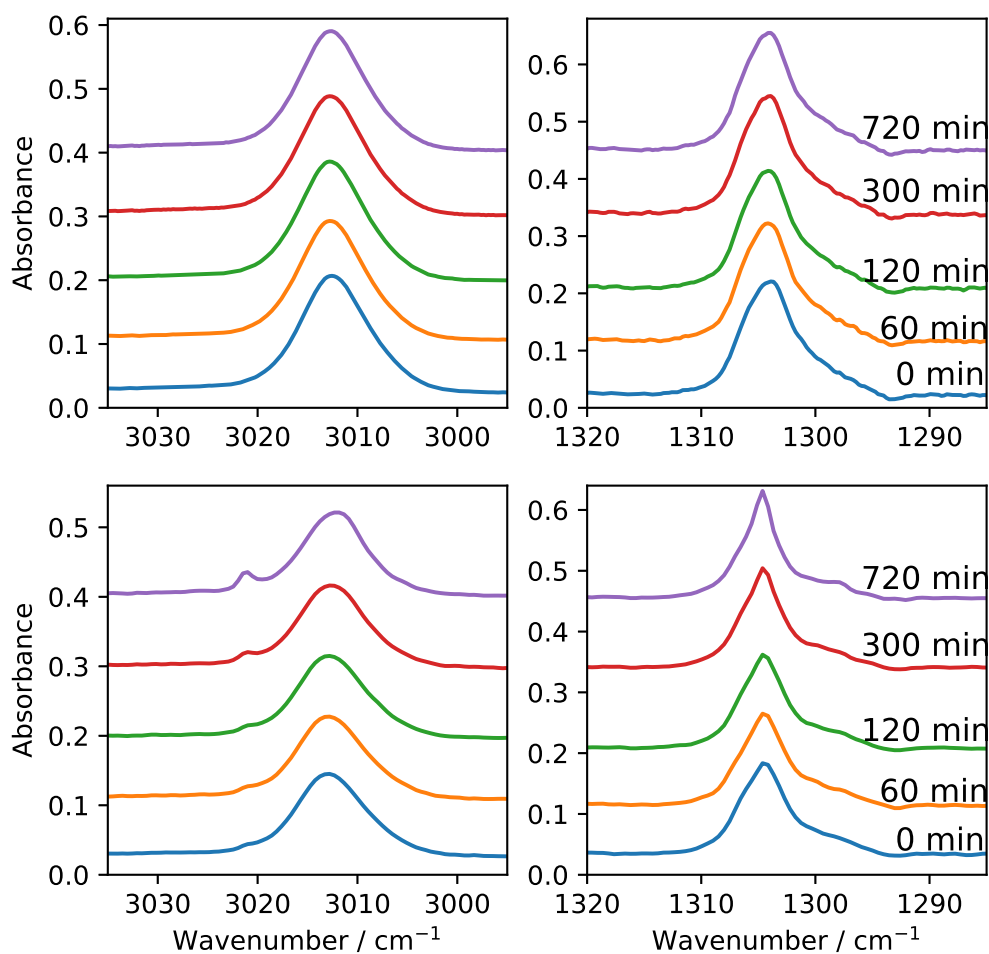


Figure 23:  $\nu_3$  (left) and  $\nu_4$  (right) modes of 100 ML of methane solid deposited at 6K. The top two panels show the temporal change of CH<sub>4</sub> ice deposited through a UHV leak valve (deposition from background gas) at a rate of 100 ML/min. The bottom two panels show the temporal change of CH<sub>4</sub> ice deposited through the molecular beamline at a rate of 1 ML/min.

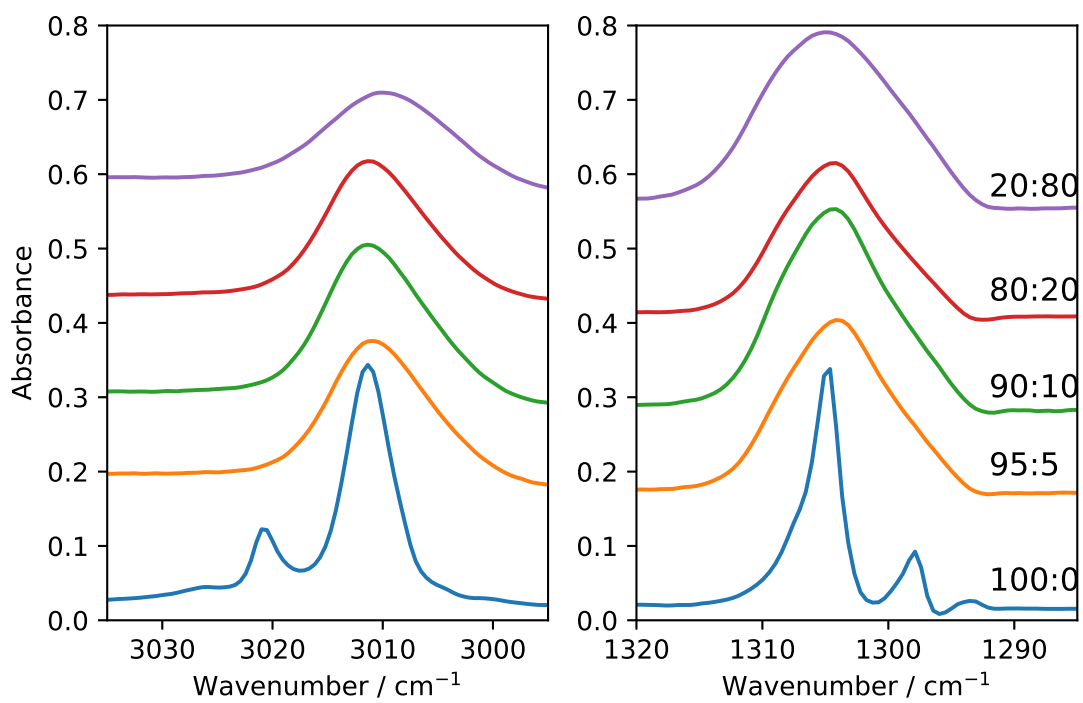


Figure 24:  $\nu_3$  (left) and  $\nu_4$  (right) modes for a CH<sub>4</sub>:H<sub>2</sub>O mixture with different concentrations. All the mixtures were deposited at 10 K.

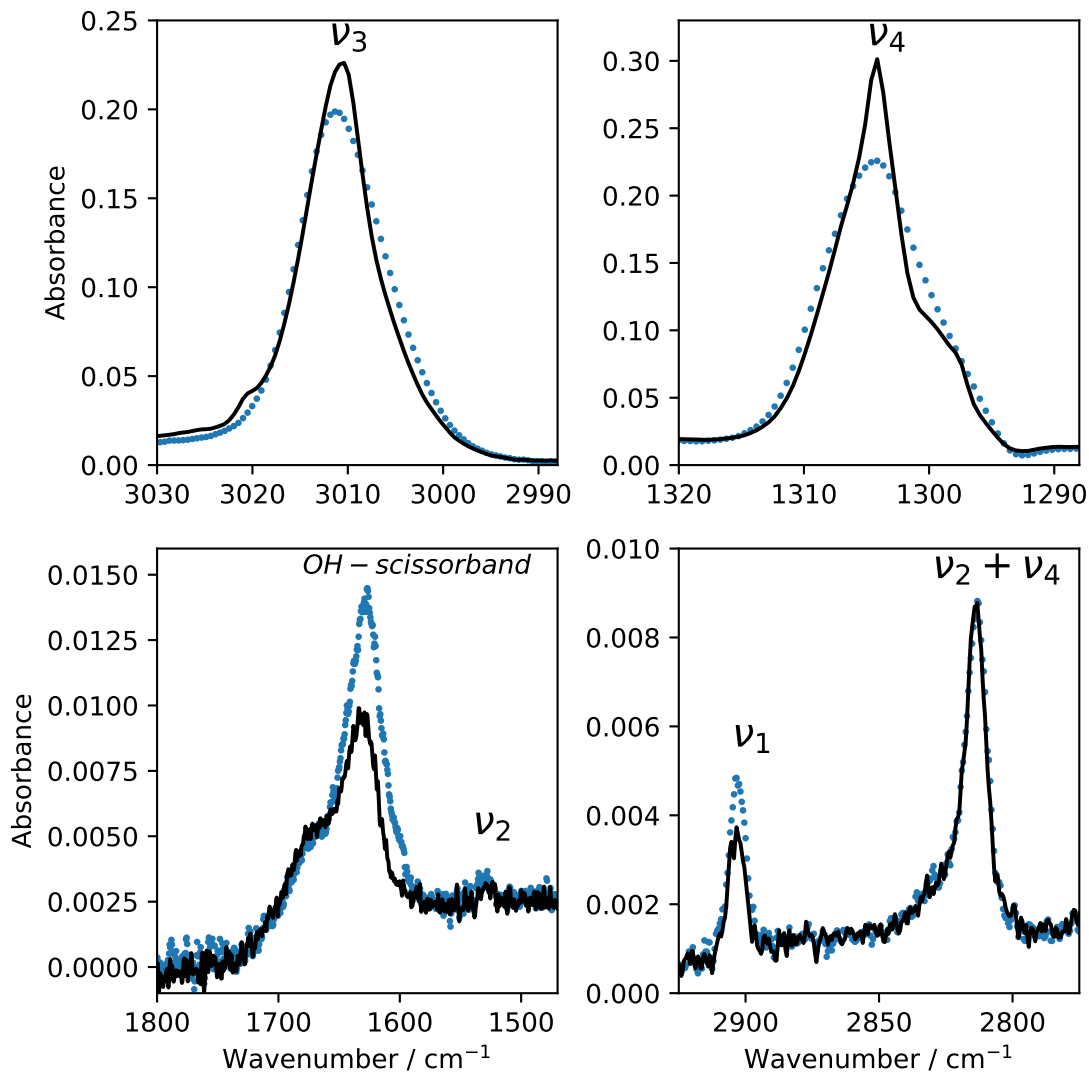


Figure 25: Segregation of water ( $\text{H}_2\text{O}$ ) in  $\text{CH}_4:\text{H}_2\text{O}$  (= 80:20) mixture for a cyclic heating up experiment in the temperature range of 10 to 30 K. The dotted IR trace represents the ice deposited at 10 K, while the solid black line is for the ice after it has undergone one round of heat cycling (from 10K to 30K and back down to 10K).

Table 3:  $\nu_4$  and  $\nu_3$  band positions, shifts and FWHM of  $\text{CH}_4:\text{H}_2\text{O}$  with different mixing ratios

Mode	Mixing ratio	Peak Position ( $\text{cm}^{-1}$ )	FWHM ( $\text{cm}^{-1}$ )	Shift ( $\text{cm}^{-1}$ )
$\nu_4$	100:0	1304.8	4.5	-
	95:5	1304.0	14	-0.8
	90:10	1303.9	14.5	-0.9
	80:20	1303.9	15.5	-0.9
	20:80	1304.2	21	-0.6
$\nu_3$	100:0	3010.9	7	-
	95:5	3010.2	10.5	-0.7
	90:10	3010.0	11.0	-0.9
	80:20	3009.9	11.2	-1.0
	20:80	3008.1	14.0	-2.8

#### 4.4.5 Segregation of water in $\text{CH}_4:\text{H}_2\text{O}$ ice matrix

The influence of IR inactive modes of  $\text{CH}_4:\text{H}_2\text{O}$  mixture was investigated in this section. Pure methane has two IR inactive modes:  $\nu_1$  ( $2904.5 \text{ cm}^{-1}$ ) and  $\nu_2$  ( $1540.0 \text{ cm}^{-1}$ ). When water is mixed with methane we don't observe band splitting in Phase II  $\text{CH}_4:\text{H}_2\text{O}$  mixture at 10 K. But the presence of water activates the IR inactive mode [44, 42]. Figure 25 shows two different IR spectra of  $\text{CH}_4:\text{H}_2\text{O}$  for two different steps of the same experiment. The dotted marked spectra represent  $\text{CH}_4:\text{H}_2\text{O}$  after the deposition at 10 K. The solid line shows the band after the ice is taken to 30 K and then cooled back to 10 K. Two intense bands (not shown) are observed at  $3500 \text{ cm}^{-1}$  and at  $1635 \text{ cm}^{-1}$ , caused by, respectively, by O-H stretching and O-H-O scissors-bending [57]. We observe significant changes in  $\nu_4$  and  $\nu_3$  modes before and after temperature cycling. Band splitting such as R(0) for  $\nu_3$  and Q(1) for  $\nu_4$  emerges after temperature cycling (Figure 26). Band strengths of  $\nu_1$ ,  $\nu_2$ , and of O-H-O scissors-bending decrease by about 50% after the heating up and cooling down process. This change in IR features is indicative of partial segregation of water in the  $\text{CH}_4:\text{H}_2\text{O}$  mixture. This segregation process happens during orientational reordering of lattice field sites of methane molecules during temperature cycling.

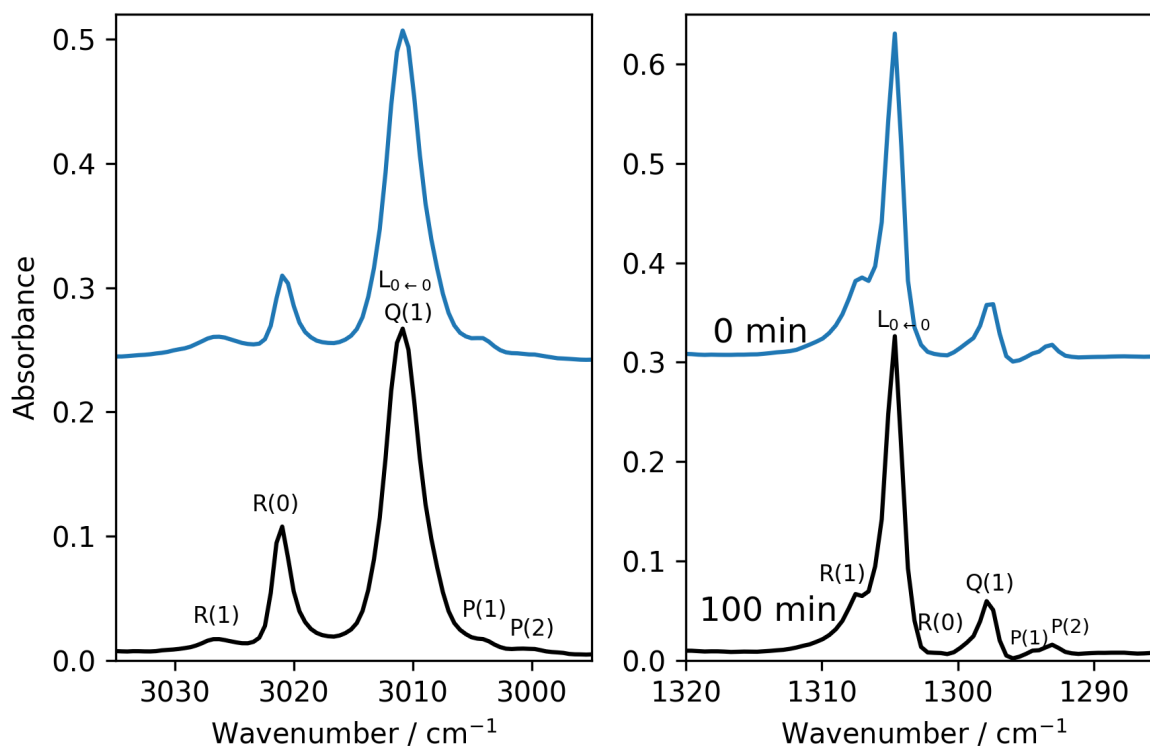


Figure 26: Temporal change of Nuclear Spin Conversion of solid methane at 7 K. The ice was prepared at 10 K (blue line), heated to 30 K, and rapidly cooled back down to 7 K (black line) to track the NSC for  $\nu_3$  and  $\nu_4$  vibrational modes over a time of 100 min.

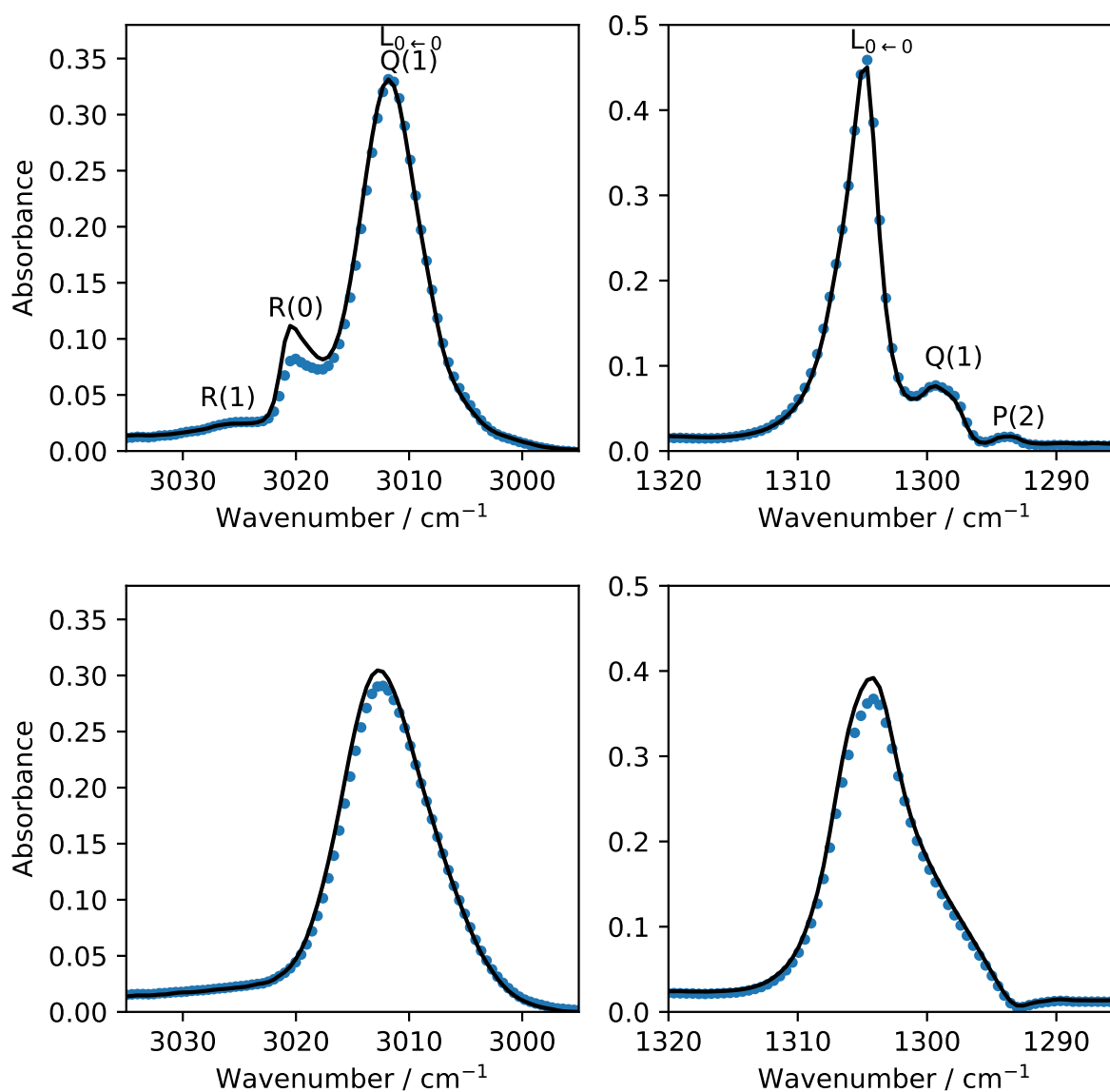


Figure 27: Temporal change of Nuclear Spin Conversion of  $\text{CH}_4:\text{H}_2\text{O}$  (= 95:5) mixture at 7 K. The ice was prepared at 10 K, heated to 30 K, and rapidly cool back down to 7 K to track the NSC for  $\nu_3$  and  $\nu_4$  vibrational modes over a time period of 30 min. The top two panels show the temporal change at 7 K after cooling down from 30 K and the bottom two panels show the temporal change over 30 min. of ice deposited as 10 K

Table 4: Band positions and shifts of pure methane and CH<sub>4</sub>:H<sub>2</sub>O=95:5 during NSC

Mode	Band Assignment	Pure Methane (cm <sup>-1</sup> )	CH <sub>4</sub> :H <sub>2</sub> O(cm <sup>-1</sup> )	Shift (cm <sup>-1</sup> )
v <sub>4</sub>	R(0)	1307.3	-	-
	R(1)	1301.2	-	-
	Q(1)	1297.8	1298.7	0.9
	P(1)	1294.4	-	-
	P(2)	1293.2	1294.4	1.2
v <sub>3</sub>	R(0)	3021.0	3020.1	-0.9
	R(1)	3026.6	3027.2	0.6
	Q(1)	3010.9	3011.4	0.5
	P(1)	3004.1	-	-
	P(2)	3000.6	-	-

#### 4.4.6 NSC in partially segregated CH<sub>4</sub>:H<sub>2</sub>O ice mixture

Nuclear Spin Conversion (NSC) is a low-temperature phenomenon that methane ice experience at 7 to 11 K, see the previous chapter. There hasn't been any report of NSC for a CH<sub>4</sub>:H<sub>2</sub>O ice mixture. For this study we kept pure and CH<sub>4</sub>:H<sub>2</sub>O (95:5) ice at 10 K for 30 min after deposition, heated up to 30 K, and then rapidly cooled back down to 7 K, and kept it at T= 7 K for 100 min. From these two experiments, see Figure 26 and Figure 27, we observe that CH<sub>4</sub>:H<sub>2</sub>O ice mixture goes through the NSC process similar to pure methane ice. This process further proves our argument that H<sub>2</sub>O segregates from CH<sub>4</sub>:H<sub>2</sub>O mixture if the ice is prepared in Phase II and undergoes a heat cycling. Therefore, we observe that the ice mixture experiences NSC at 7 K (which is a distinct feature of pure CH<sub>4</sub>) when it underwent segregation, but not when was deposited in the mixed state (bottom panels of Figure 27). All the relevant values of v<sub>3</sub> and v<sub>4</sub> vibrational modes peak position and band-shift are listed in Table 4.

#### 4.4.7 Methane and nitrogen ice mixtures with different ratios

N<sub>2</sub> is a non-polar molecule and the unit cell of N<sub>2</sub> has lattice parameter of 5.64 Å [49]. On the other hand, the unit cell of CH<sub>4</sub> has a lattice parameter of 5.89 Å. Thus, it's a reasonable assumption

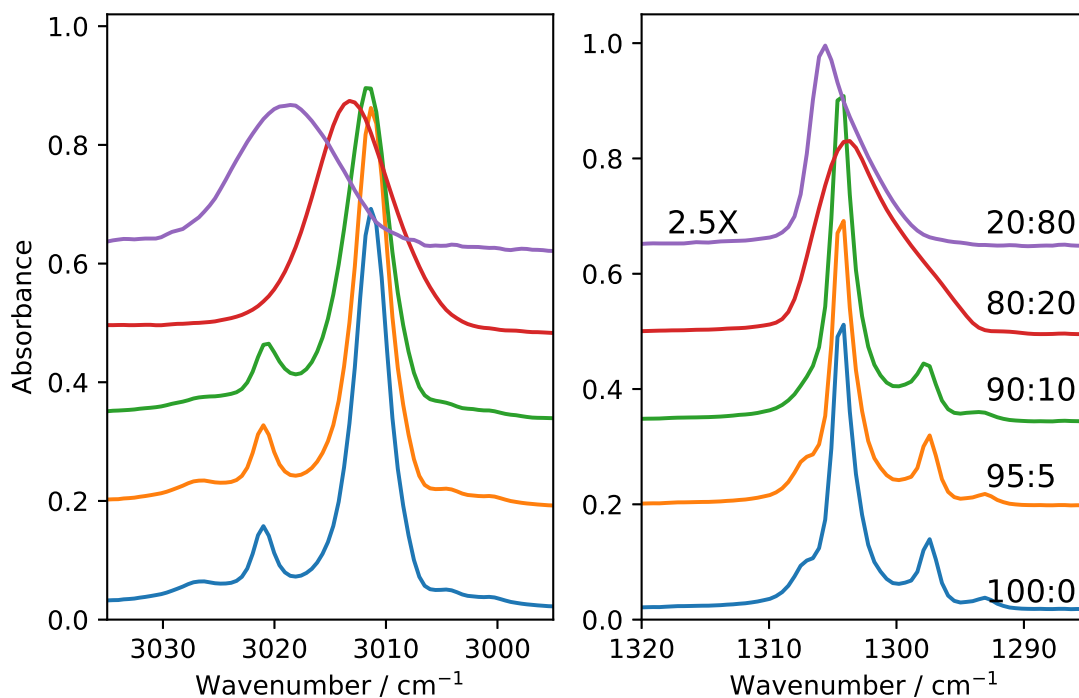


Figure 28: FTIR spectra of solid methane in the  $\nu_3$  and  $\nu_4$  vibrational modes for  $\text{CH}_4:\text{N}_2$  mixture for various concentration at a resolution of  $1.0 \text{ cm}^{-1}$ . All the mixtures were deposited at 10 K. This figure represents how the increase of  $\text{N}_2$  in  $\text{CH}_4:\text{N}_2$  ice matrix distort the molecular symmetry of  $\nu_4$  and  $\nu_3$  mode of solid methane

that in  $\text{CH}_4:\text{N}_2$  mixture,  $\text{N}_2$  is in a substitutional site, rather than in an interstitial site as the ices have similar lattice parameters and both have face center cubic (fcc) structure. Figure 28 shows the IR data for  $\nu_4$  and  $\nu_3$  modes of  $\text{CH}_4:\text{N}_2$  with different mixing ratios. We observe that there is insignificant change once we introduce little  $\text{N}_2$  in the ice matrix. The  $\text{CH}_4$  lattice symmetry is disrupted once the impurity level reaches 20%. At  $\text{CH}_4:\text{N}_2$  80:20 ratio we observe the satellite peaks of  $\text{CH}_4$   $\nu_4$  and  $\nu_3$  modes completely disappear which indicates that the  $\text{N}_2$  molecules in the ice matrix disrupt the neighboring  $\text{CH}_4$  symmetry sites. We see a significant change in IR features and FWHM values at  $\text{CH}_4:\text{N}_2$  80:20. In this case, we observe the peak position is red-shifted by  $0.4 \text{ cm}^{-1}$  and  $2.3 \text{ cm}^{-1}$  for  $\nu_4$  and  $\nu_3$ , respectively. The FWHM becomes  $9.4 \text{ cm}^{-1}$  for  $\nu_4$  and  $9.5 \text{ cm}^{-1}$  for  $\nu_3$  modes, which is a slight increase from pure methane  $\nu_4$  and  $\nu_3$  modes FWHM. The blue-shift in peak position is more significant for the  $\nu_3$  than for the  $\nu_4$  mode. All the relevant values are listed in Table 5.

Table 5: Band positions, FWHM and shifts of  $\nu_4$  and  $\nu_3$  modes of CH<sub>4</sub>:N<sub>2</sub> for various mixing ratios

<b>Mode</b>	<b>Mixing ratio</b>	<b>Peak Position (<math>cm^{-1}</math>)</b>	<b>FWHM (<math>cm^{-1}</math>)</b>	<b>Shift (<math>cm^{-1}</math>)</b>
$\nu_4$	100:0	1304.8	4.5	-
	95:5	1304.9	4.7	0.1
	90:10	1305.0	4.8	0.2
	80:20	1304.6	9.4	0.4
	20:80	1306.4	6.5	1.4
$\nu_3$	100:0	3010.9	7	-
	95:5	3011.0	7.2	0.1
	90:10	3011.2	7.5	0.3
	80:20	3013.2	9.5	2.3
	20:80	3018.6	12.8	8.5

#### 4.4.8 Diffusion of molecules in methane and nitrogen ice mixtures

Figure 29 shows two different IR spectra of CH<sub>4</sub>:N<sub>2</sub> for two different steps of the same experiment. It shows that both CH<sub>4</sub> and N<sub>2</sub> diffuses in ice mixture as ice undergoes a heat cycling between 10 and 20 K. We observe significant change in  $\nu_3$  mode and  $\nu_2+\nu_4$   $\nu_3+\nu_4$  combinations modes. The peak position of  $\nu_3$  mode blue shifts 3012.5 cm<sup>-1</sup> to 3016.3 cm<sup>-1</sup> and FWHM becomes 14.8 cm<sup>-1</sup> from 9.5 cm<sup>-1</sup>. In case of combination modes,  $\nu_2+\nu_4$  loses its band strength by 50 % and  $\nu_3+\nu_4$  blue shifts during this diffusion process. A detail study of CH<sub>4</sub>/N<sub>2</sub> diffusion process is presented in Chapter 5.

### 4.5 Astrophysical Implications

Methane has been detected both towards low- and high-mass young stellar objects in the ISM. Methane is predicted to form in ISM primarily from the atomic addition reaction of H-atoms and solid C at the onset of H<sub>2</sub>O-rich ice phase of molecular clouds [59]. Observations of solid CH<sub>4</sub> toward a few high mass young stellar objects (YSOs) show that the CH<sub>4</sub> absorption band profiles are broad and agree better with CH<sub>4</sub> in hydrogen-bonding ice, H<sub>2</sub>O or CH<sub>3</sub>OH, than with a pure CH<sub>4</sub> ice or CH<sub>4</sub> mixed with CO [12]. Öberg et al. [59] reported that CH<sub>4</sub> 7.7 μm (1298cm<sup>-1</sup>) absorption feature is redshifted due to presence of water. These observational findings indicate that interstellar CH<sub>4</sub> most likely was formed in H<sub>2</sub>O-rich environment and mixed with other polar and no-polar molecules. On the other hand astronomical model of galactic hot molecular cores in the Large and Small Magellanic Clouds using a gas-grain network predicts that molecular CH<sub>4</sub> abundance is larger when compared with the elemental abundance [2]. This fact might indicate the segregation of CH<sub>4</sub> from the ice matrix in ISM. To date, segregation of CH<sub>4</sub> from polar H<sub>2</sub>O ice has not been confirmed in the laboratory. The increase in sensitivity of the JWST Mid-Infrared telescope is expected to allow observations of CH<sub>4</sub> ice towards numerous background stars to probe more quiescent environments, in addition to observations towards YSOs. The work presented here is the first experimental proof of CH<sub>4</sub> segregation mechanism from H<sub>2</sub>O ice. The temporal evolution of NSC (presented in Figure 24) in segregated CH<sub>4</sub> ice can be a crucial probe to study the evolutionary phase of ISM CH<sub>4</sub> ice. The astrophysical importance of CH<sub>4</sub>:N<sub>2</sub> mixture is discussed in the following chapter.

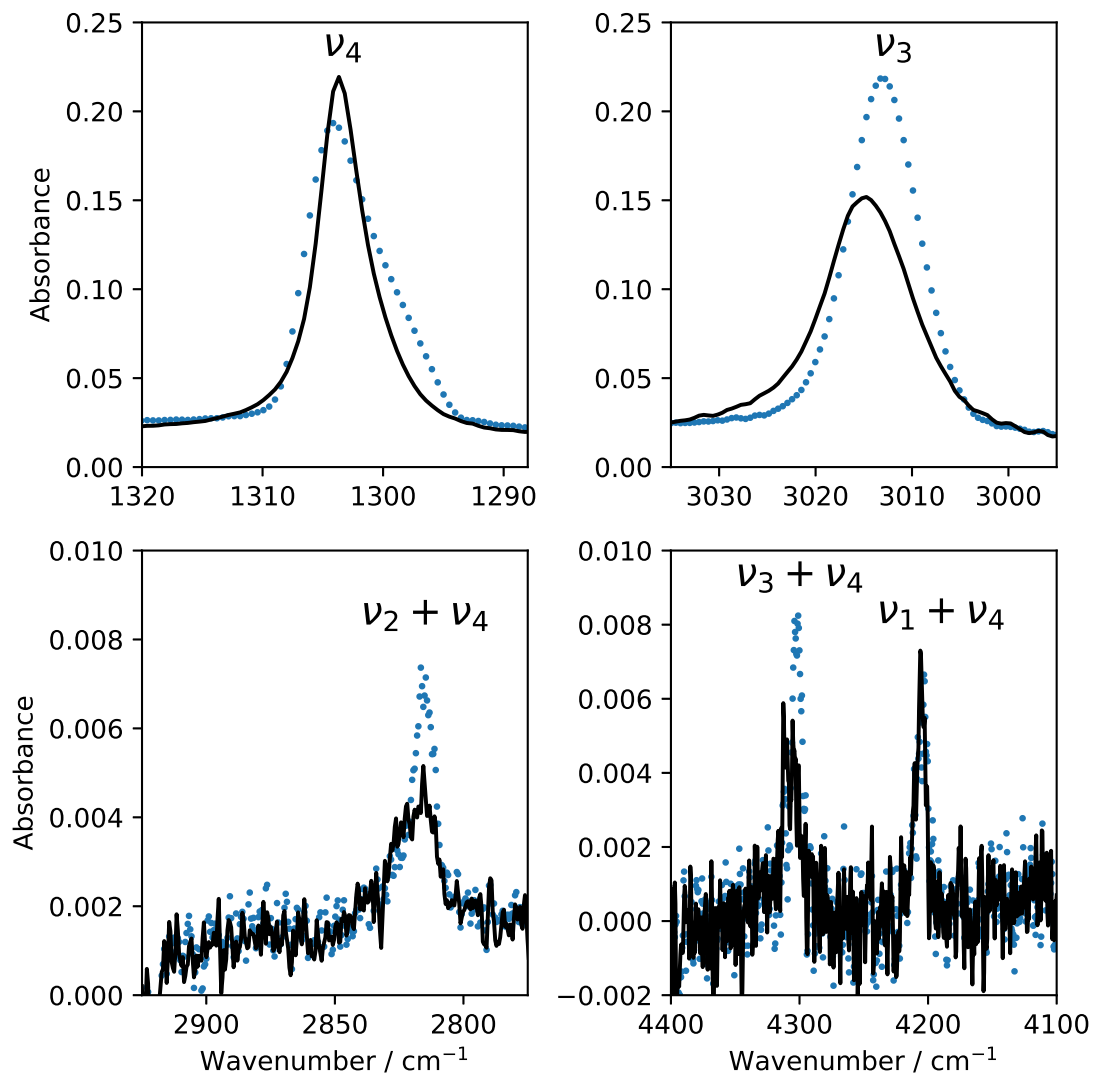


Figure 29: Diffusion process of  $\text{N}_2$  in  $\text{CH}_4:\text{N}_2$  (= 80:20) mixture in a cyclic heating experiment in a temperature range of 10 to 20 K. The blue dotted line shape represents the ice mixture upon deposition and solid black line represents the ice that is taken to 20 K and then cooled back to 10 K.

## 4.6 Summary

This chapter presents the infrared spectroscopic properties in mid-IR and near-IR spectral range ( $650\text{-}5000\text{ cm}^{-1}$ ) of pure methane and methane ice mixtures at low temperature. It reports the experimental data of band peaks, spectral features, bandwidth, and their variation in pure methane and methane ice mixtures under different concentrations and thermal cycling. The main conclusions we derive from this work are the following:

- Methane solid undergoes thin-film effects below 10 ML coverage. We observed changes in the temperature of the transformation from Phase II to Phase I below that coverage. From our experiments, we found that the transition happens around 24.0 K for 10 ML methane ice. Beyond 10 ML ice, we observe that the transition temperature shifts close to the bulk temperature of 20.4 K.
- Nuclear Spin Conversion (NSC) at cryogenic temperature depends on the deposition rate. In our recent work (see Chapter 3) about metastable Phase II of methane, we showed that NSC is very insignificant at temperature  $<7\text{ K}$ . In the present work, we showed that the rate of NSC can vary depending on the deposition method and deposition rate. We used a UHV leak valve for background gas deposition and a molecular beamline to deposit a similar amount of methane at 6 K. We found that although NSC is virtually nonexistent in a fast deposition (100 ML/min, deposited from background gas); NSC is quite active for a slow deposition of ice at 6 K (1 ML/min, from the beamline).
- We showed that methane thin film phase transition is a slow process due to the disruption of neighbouring sites and the substantial amount of orientational ordering and re-ordering occur around 20.4 K. In the past decades, most of phase transition experiments of  $\text{CH}_4$  solid were done inside closed cells. In those experiments it was showed that the phase transition for methane solid is abrupt and centered around 20.4 K. However, ices of  $\text{CH}_4$  in ISM and planetary bodies in pure and mixed forms consist of a small number of layers.
- Methane ice IR features become distorted even if there is very little (5%) amount of water present in the ice matrix. The peak position of the  $\text{CH}_4\text{:H}_2\text{O}$  matrix gets red-shifted as we increase the amount of water in the mixture. Similarly, the FWHM of the  $\text{CH}_4\text{:H}_2\text{O}$  broadens with the increased percentage of water.
- We showed evidence of water segregation with temperature cycling (warming and cooling) of the  $\text{CH}_4\text{:H}_2\text{O}$  ice mixture. Water partially segregates from the  $\text{CH}_4\text{:H}_2\text{O}$  mixture if the ice

experiences orientational reordering of methane molecules in the ice mixture. We know that pure methane ice experiences NSC in the 7 to 11 K temperature range. No NSC is observed in CH<sub>4</sub>:H<sub>2</sub>O when deposited at 7 K. Active NSC of CH<sub>4</sub>:H<sub>2</sub>O (=95:5) mixture, prepared in the orientationally disordered phase (Phase I) and then cooled to 7 K, shows that water is segregated.

- CH<sub>4</sub> and N<sub>2</sub> ices have similar lattice parameters and the same fcc symmetry. A very small amount of non-polar molecules (N<sub>2</sub>) doesn't distort the orientational ordering of Phase II methane. In our experiment, we showed that in CH<sub>4</sub>:N<sub>2</sub> ice matrix at least (20%) of N<sub>2</sub> is required for the distortion of lattice symmetry inside the ice mixture to appear. Once the mixing ratio reaches that limit, the IR spectra of CH<sub>4</sub>:N<sub>2</sub> experience a blue shift of peak positions of  $\nu_3$  and  $\nu_4$  modes. In addition, band splitting due to NSC diminishes for the mixing ratio of CH<sub>4</sub>:N<sub>2</sub> (=80:20) and beyond. From the results of our experiments, we propose that N<sub>2</sub> is in a substitution site, rather than in an interstitial site. Once the temperature is raised, diffusion of N<sub>2</sub> becomes efficient, i.e. more N<sub>2</sub> destroys the symmetry sites of the CH<sub>4</sub> structure.

## Chapter 5

# Temperature Evolution of CH<sub>4</sub> : N<sub>2</sub> Ice Mixture - an Application to trans-Neptunian Objects

### 5.1 Abstract

CH<sub>4</sub>:N<sub>2</sub> ice mixtures that are relevant to the studies of Trans Neptunian Objects (TNO) were investigated using IR spectroscopy. Ices of CH<sub>4</sub> and N<sub>2</sub> with a wide range of mixing ratios are present in TNOs (such as Pluto, Triton, and others) in pure, binary, or ternary mixtures. The recent NASA New Horizons flyby near Pluto piqued the current interest in CH<sub>4</sub>: N<sub>2</sub> ices, as these ices are important in nitrile chemistry when subjected to energetic particles/radiation. We have studied the evolution of IR vibrational bands of CH<sub>4</sub> in CH<sub>4</sub>: N<sub>2</sub> thin films under different conditions. The experiments, conducted under UHV conditions, explored the influence on ice morphology of film thickness, temperature, heating rate, and mixture ratio.

## 5.2 Introduction

Trans Neptunian Objects (TNOs) are some of the most primitive and smaller solar system bodies. The physical properties of these objects have been little known to astronomers and scientists because of their low albedos, small sizes, and large distance from Earth [91, 65, 89, 60]. Pluto and Titan, the largest satellite of Saturn, are the two relatively larger TNOs. They have a dense N<sub>2</sub>-CH<sub>4</sub> rich atmosphere and surface composition similar to the primordial Earth's atmosphere when the earliest form of life emerged through complex chemistry [47, 78].

Nitrogen is an important component of the surface and atmosphere of Pluto and Triton [47, 51]. The surface temperature of Pluto and Triton is 33.1 K and 35.6 K, respectively. Even at these low temperatures solid nitrogen is fairly volatile and can sublime to form an atmosphere or condense back to nitrogen solid. In the presence of ambient pressure and at low temperature solid nitrogen can be found in two crystal structures.  $\beta$ -N<sub>2</sub> is a hexagonal close-packed structure that exists from 35.6 K up to 63.1 K [68]. Another phase,  $\alpha$ -N<sub>2</sub>, exists below 35.6 K at low pressure and has a cubic structure. In UHV conditions, the transition from  $\alpha$ -N<sub>2</sub> to  $\beta$ -N<sub>2</sub> solid can occur at a much lower temperature than in equilibrium with its own gas. On the other hand, methane solid has two crystal phases, each with an fcc lattice, but in one molecules are partially orientationally ordered,  $\alpha$ -CH<sub>4</sub>, while in the other,  $\beta$ -CH<sub>4</sub>, they are orientationally disordered. The transition temperature is at 20.4 K in the bulk, see also preceding chapters. IR spectroscopy has been one of the main probes for astronomers to study outer solar system bodies and for chemical physicists to mimics the ices in those bodies. N<sub>2</sub> is IR inactive or very weakly active. But solid N<sub>2</sub> is porous [54] and can entrap volatiles such as CH<sub>4</sub> and CO in different ratios in the diffused solid mixture [33]. Nitrile chemistry of the outer solar system bodies can be probed through these entrapped volatiles. Astronomers have detected methane solid diffused in N<sub>2</sub> ice in Pluto and Triton, although there has been very little systematic experimental studies or evidence about the exact energetic processes behind the formation of this diffused N<sub>2</sub>:CH<sub>4</sub> solid and sublimation of the solid that creates the thick atmosphere of Pluto and Triton.

The shapes and the relative intensities of most of the CH<sub>4</sub> IR bands are significantly different in CH<sub>4</sub> isolated in N<sub>2</sub> than those in pure CH<sub>4</sub> ice and are also sensitive to the temperature and the crystal phase of N<sub>2</sub> [69]. It has been found in experiments that when N<sub>2</sub>:CH<sub>4</sub> solid is deposited at low temperature (i.e. 10 K) with a mixing ratio of 20:80 and higher,  $\alpha$ -N<sub>2</sub> crystalline structure gets distorted (Emtiaz et. al in prep). In UHV conditions and at that temperature the gas mixture forms an immiscible  $\alpha$ -N<sub>2</sub> and  $\alpha$ -CH<sub>4</sub> solution, which is representative of a segregated CH<sub>4</sub> and N<sub>2</sub> inside the solid. Once the solid is supplied with enough energy (i.e. by heating), it becomes a diffused mixture of  $\alpha$ -CH<sub>4</sub> and  $\alpha$ -N<sub>2</sub>. This transformation is quick and dependent on the mixing

ratio. Astronomers have reported that CH<sub>4</sub> combination modes involving IR inactive modes (i.e.  $\nu_1+\nu_3$  and  $\nu_2+\nu_4$ ) are absent in Triton's spectrum, which indicates that CH<sub>4</sub> molecules are isolated and diffused in the N<sub>2</sub>:CH<sub>4</sub> solid [69, 23, 52].

In infrared spectroscopic study, spectra for the molecular ices at Mid-IR ( $\nu=4000-400\text{ cm}^{-1}$ ;  $\lambda = 2.5-25\text{ }\mu\text{m}$ ) absorption features are the result of their fundamental rovibrational modes and combination modes of the fundamental modes, and their overtones. This is an obvious fact that the Mid-IR features of IR active molecules are the strongest features of IR spectrum. On the other hand, near-IR ( $\nu=10000-4000\text{ cm}^{-1}$ ;  $\lambda = 1.0-2.5\text{ }\mu\text{m}$ ) features consist of the combination modes and higher overtones and consequently, they represent much weaker features of IR spectrum. Most of the observational data for pure CH<sub>4</sub> solid and CH<sub>4</sub> mixtures present in ISM and planetary bodies are based on near-IR features of the methane absorption spectra. For this reason, Near-IR observational data for the methane spectrum, specifically for outer solar system bodies where methane ice mixtures have been identified, is quite difficult to match with the laboratory data based on Mid-IR. The James Webb Space Telescope, scheduled to be launched in 2021 [31], will usher in a new age of methane chemistry as the next-generation space telescope will be equipped with NIRCam and MIRI. The JWST Near-Infrared Spectrometer (NIRSpec) will perform observations from 0.6 to 5  $\mu\text{m}$  ( 16667- 2000  $\text{cm}^{-1}$ ) and MIRI (Mid-InfraRed Instrument) will measure mid to long wavelength range from 5 to 27  $\mu\text{m}$  ( 2000- 370  $\text{cm}^{-1}$ ) [28]. Once the data from NIRCam and MIRI is available, the laboratory mid-IR data of pure methane solid and in mixtures with N<sub>2</sub> and H<sub>2</sub>O will be useful.

The study of nitrile chemistry of TNOs can be a significant probe of Earth's prebiotic history. Most TNOs landscape were shaped by the endless condensation and sublimation cycles of the volatile ices covering its surface [33]. The latest spectra from the New Horizons mission reveal an abundance of methane ice on Pluto's surface, but with striking differences from place to place across the frozen surface of Pluto [9]. These ices can be CH<sub>4</sub>-rich ice and CH<sub>4</sub> diffused in N<sub>2</sub>-rich ice [33, 67]. The size of a TNO, the distance from the sun, and its surface temperature are the primary factors impacting an object's surface composition. Astrophysical models of volatile retention on TNOs take these properties into consideration when used to evaluate whether or not a TNO should retain its initial volatile inventory over the age of the solar system [71]. Surface diffusion and sublimation process can play an important role in volatile retention on TNOs. The exact process of CH<sub>4</sub>/N<sub>2</sub> diffusion, and N<sub>2</sub> sublimation from ice mixture is still unknown on the cold surface of TNOs. In this work we report two transformations in CH<sub>4</sub> and N<sub>2</sub> ice mixtures under UHV conditions. The mid-infrared spectra are well suited to investigate the surface composition of TNOs, as the fundamental vibration  $\nu_4$  and  $\nu_3$  mode of methane lies in mid-infrared.

These results will be a useful reference to analyze the observational data collected by JWST-MIRI detector [31, 64].

The Arrhenius equation gives the dependence of the rate constant of chemical or physical change in the ice structure on the absolute temperature, a pre-exponential factor, a other constants of the reaction. This equation can be used to calculate the activation energy of the 1<sup>st</sup> transformation in CH<sub>4</sub>: N<sub>2</sub> ice mixture.

$$k = Ae^{\frac{-E_a}{k_B T}} \quad (5.1)$$

where  $k$  is the rate constant.  $T$  is the absolute temperature (in K).  $A$  is the pre-exponential factor, a constant for each physical/chemical change.  $E_a$  is the activation energy for the change, and  $k_B$  is the Boltzmann constant. Taking the natural logarithm of Equation 5.1 yields:

$$\ln k = \ln A - \frac{E_a}{k_B T} \quad (5.2)$$

Rearranging Equation 5.2 yields:

$$\ln k = \frac{-E_a}{k_B} \frac{1}{T} + \ln A \quad (5.3)$$

Equation 5.3 has the same form as an equation for straight line,  $y=mx+c$ , where  $x$  is the reciprocal of  $T$ . So, when a reaction has a rate constant that obeys Arrhenius equation, a plot of  $\ln A$  versus  $T^{-1}$  gives a straight line, whose gradient and intercept can be used to determine the activation energy  $E_a$ .

### 5.3 Experimental Methods

A detailed description UHV apparatus is given in Chapter 2 of this thesis as well as prior published works [37]; here only the main features that are relevant to this study are summarized. We used the lab grade compressed CH<sub>4</sub> and N<sub>2</sub> gases from Airgas in our experiments. Gas mixtures are prepared inside the gas-line attached to the chamber within an hour of the experiment. We also ran a few experiments where we let the gas-mixture sit overnight and found no significant difference in the experimental outcome. Premixed CH<sub>4</sub> and N<sub>2</sub> gas in a gas mixing container was deposited using a single UHV leak valve for CH<sub>4</sub>:N<sub>2</sub> mixture deposition. Ices were grown on the sample disk by introducing methane through a stepper motor controlled UHV precision leak valve. A LabVIEW program controlled the rate of the deposition and the thickness of the deposit. In all experiments, 100 monolayers (ML, defined as 10<sup>15</sup> molecules/cm<sup>2</sup>) of ice deposited at 8 ML/minute has been used. This deposition dose was calculated using the impingement rate, see Chapter 2 for details.

## 5.4 Results and Analysis

We carried out two sets of experiments. In the first set, we studied the attributes of crystalline phases of methane based on different variables. For these experiments, pure methane ices of different thicknesses were either produced at 6 or 10 K. Then the methane ice was either kept at a specific temperature for an extended period of time or heated up slowly at 3 K/min until the methane ice desorbs beyond 40 K. In the second set methane ice mixed with either water or nitrogen was deposited at 10 K and then the ice went through temperature cycling (heating up and cooling down) to study the changes in IR features during the process.

### 5.4.1 Comparison between CH<sub>4</sub> and CH<sub>4</sub>: N<sub>2</sub> IR spectra

The presence of N<sub>2</sub> in CH<sub>4</sub> ice matrix has a different effect than the presence of other volatiles such as H<sub>2</sub>O, see Chapter 4. Figure 30 shows a relative spectrum of pure methane and CH<sub>4</sub>:N<sub>2</sub> mixture to mark down the first significant IR spectrum change of these cases while slow heating from 10 to 40 K. The top two plots are  $\nu_4$  and  $\nu_3$  modes of pure methane at 14 K (solid line) and 15 K (dotted line) while heating up the ice at a rate of 0.5 K/min. On the other hand the bottom two plots show the  $\nu_4$  and  $\nu_3$  mode of CH<sub>4</sub>:N<sub>2</sub>= 80:20 mixture at the same temperature point. In the case of pure methane at 10 K, the ice is in Phase II crystalline form and as we slowly heat up the ice we observe that some orientational disorder takes place between 14 to 15 K and simultaneously we observe some change in the IR spectrum. However, we observe completely different behavior for the CH<sub>4</sub>:N<sub>2</sub> mixture. We observe a significant change in shape and blue shift in peak position for fundamental vibrational modes of CH<sub>4</sub>. For the latter part of this investigation, we would term this change in ice mixture as 1<sup>st</sup> transformation.

### 5.4.2 Diffusion of molecules in CH<sub>4</sub> and N<sub>2</sub> ice matrix

We observe the 1<sup>st</sup> transformation in 20% or more mole fraction of N<sub>2</sub> in the ice matrix. When premixed methane-nitrogen molecules are deposited on a cold surface under UHV conditions, the ice matrix forms patches of methane and nitrogen molecules inside the mixture. This patch formation of individual molecules depends on the mixing ratio of the molecules and the deposition temperature of the mixture. As the ice undergoes thermal processing (heated to a higher temperature), CH<sub>4</sub> and N<sub>2</sub> molecules in segregated patches inter diffuse and mix. This mixing is active upon deposition at 10 K for the N<sub>2</sub> dominated ice mixture. Figure 32 shows that 1<sup>st</sup> transformation takes place between 9.6 to 10.2 K for the CH<sub>4</sub>:N<sub>2</sub>= 20:80 mixture. On the other hand, for the CH<sub>4</sub>:N<sub>2</sub>= 80:20 mixture in Figure 30 the temperature of this transformation is much

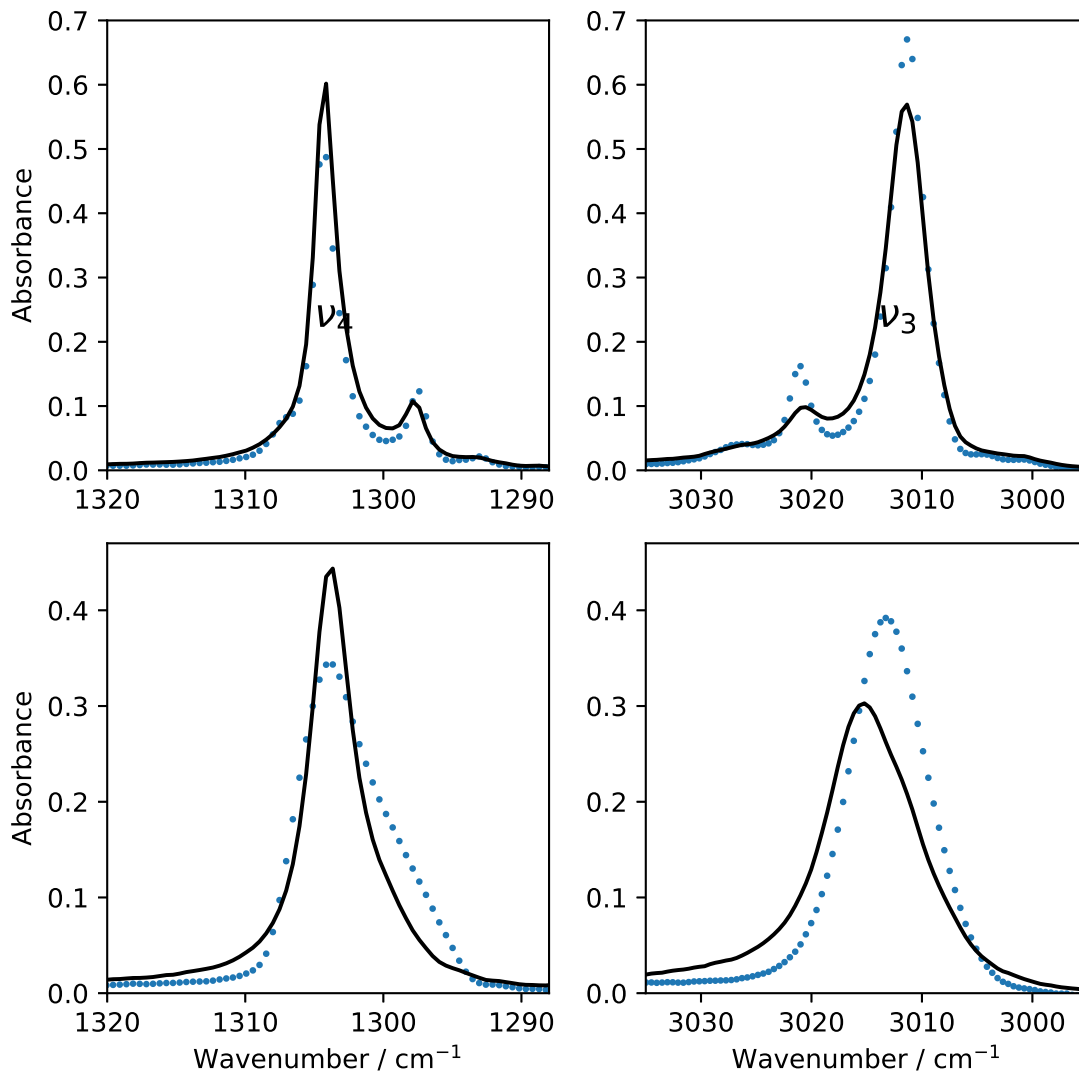


Figure 30: IR spectra of  $\nu_4$ (left) and  $\nu_3$  (right) modes of 100 ML of pure methane (top) and  $\text{CH}_4:\text{N}_2 = 80:20$  (bottom) mixture in a temperature range of 10 to 20 K. The blue dotted line shape represents the ice mixture upon deposition and solid black line represents the heated up ice at 20 K.

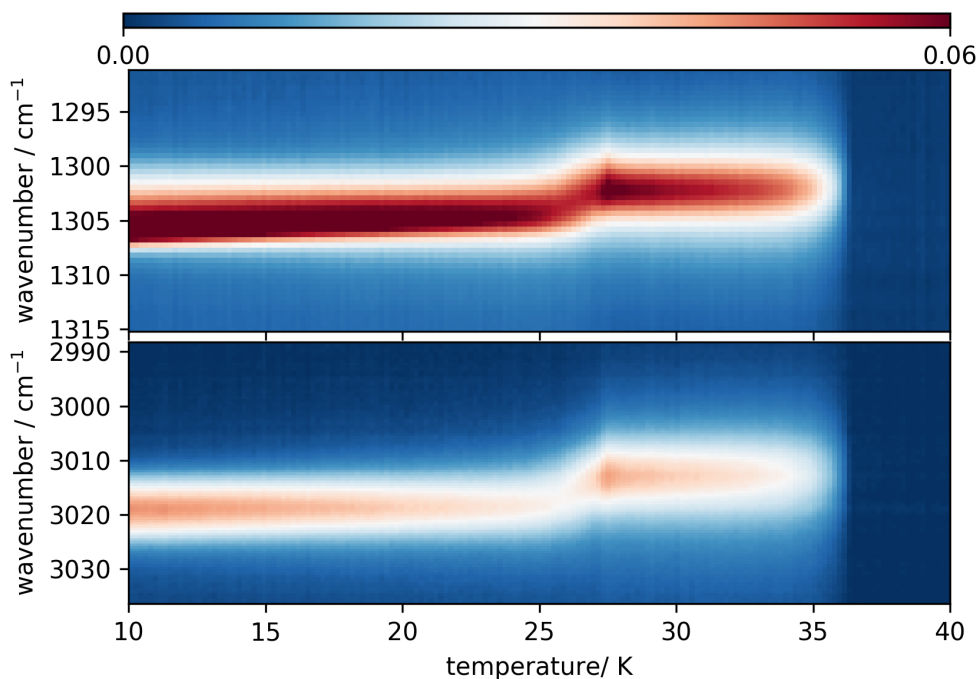


Figure 31: IR Intensity map of  $\nu_4$  (top) and  $\nu_3$  (bottom) modes of 100 ML  $\text{CH}_4:\text{N}_2=20:80$  mixture for a slow heating up experiment between 10 and 40 K.

higher, 14.1 to 15.0 K.

### 5.4.3 Diffusion of $\text{CH}_4$ and $\text{N}_2$ molecules in $\text{N}_2$ dominated ice matrix

The diffusion energy barrier is smaller for the ice dominated by a single-molecule. We don't observe any significant change in IR structure when the ice is dominated by  $\text{CH}_4$  ( $>80\%$ ) as  $\text{N}_2$  (minority) molecules occupy the substitutional sites due to similar lattice parameter and fcc lattice structure. As we decrease the ratio of  $\text{CH}_4$  ( $<80\%$ ) in the ice mixture, patches of individual molecules form inside the ice matrix. This cluster formation of molecules depends on the deposition temperature and mixing ratio of the molecules. For this reason, we observe the temperature range of 1<sup>st</sup> transformation increases as it requires more energy for the molecules to inter diffuse inside the ice matrix. We observe the highest temperature range for 1<sup>st</sup> transformation in case of evenly mixed (50:50)  $\text{CH}_4$  and  $\text{N}_2$  molecules in Figure 33. If the ice matrix is dominated by  $\text{N}_2$  ( $\geq 80\%$ ), as shown in Figure 31,  $\text{CH}_4$  and  $\text{N}_2$  molecules don't form patches upon deposition at 10 K. As the ice is mostly dominated by single-molecule ( $\text{N}_2$ ), diffusion of  $\text{N}_2$  and  $\text{CH}_4$  that is observed in 1<sup>st</sup> transformation take place upon deposition at 10 K. The experiment as described in Figure 32 further strengthens the argument where we observe 1<sup>st</sup> transformation in the ice matrix

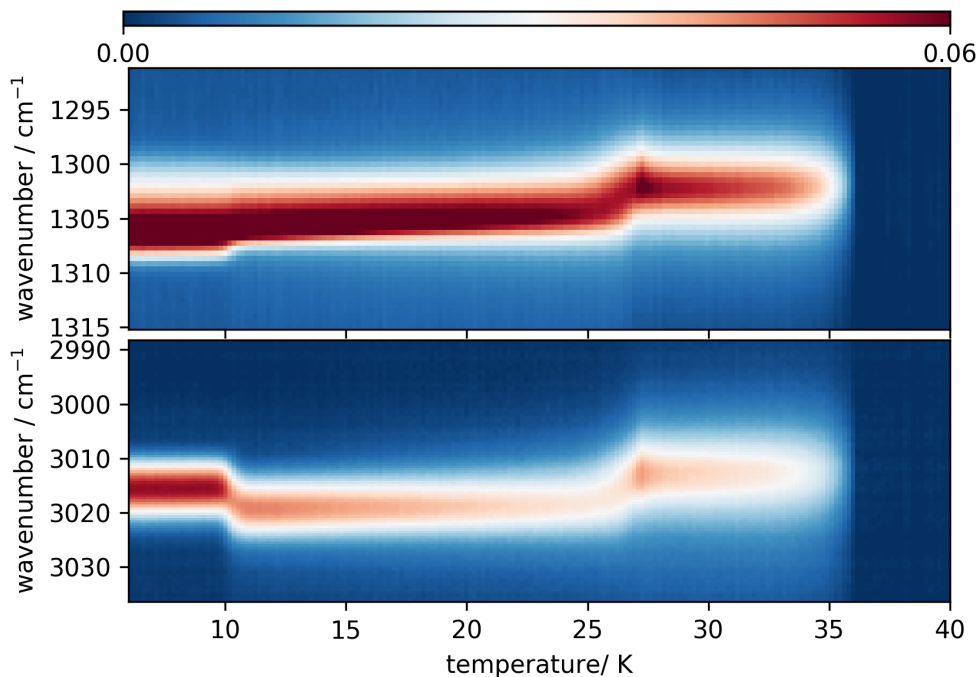


Figure 32: IR Intensity map of  $\nu_4$  (top) and  $\nu_3$  (bottom) modes of 100 ML  $\text{CH}_4:\text{N}_2= 20:80$  mixture for a slow heating up experiment between 6 and 40 K.

while heating up from 6 to 40 K. In this case,  $\text{CH}_4$  and  $\text{N}_2$  molecules inter diffuse between 9.6 to 10.2 K for 6 K deposited  $\text{CH}_4:\text{N}_2= 20:80$  ice mixture.

#### 5.4.4 $2^{\text{nd}}$ transformation in $\text{CH}_4$ and $\text{N}_2$ ice matrix

We observe significant red-shift in peak position of  $\nu_4$  and  $\nu_3$  modes in  $\text{N}_2$  dominated ice. Figure 32 shows the slow heating up experiment of  $\text{CH}_4:\text{N}_2= 20:80$  mixture from 6 to 40 K. In this experiment in addition to  $1^{\text{st}}$  transformation there is another significant change in ice structure between 27.6 to 28.4 K. This change happens due to the sublimation of  $\text{N}_2$  molecules from the ice matrix. We call this change in ice mixture the  $2^{\text{nd}}$  transformation. We observe significant changes in  $\nu_3$  mode as compared to changes in  $\nu_4$  mode in both transformations. For example, in the experiment shown in Figure 32, the  $\nu_3$  mode blue-shifts from  $3014.5 \text{ cm}^{-1}$  to  $3021.2 \text{ cm}^{-1}$  during  $1^{\text{st}}$  transformation and red-shifts from  $3021.2 \text{ cm}^{-1}$  to  $3012.8 \text{ cm}^{-1}$  during  $2^{\text{nd}}$  transformation, while changes in  $\nu_4$  are smaller (top of Figure 32). For the sake of convenience of analysis, we will only present  $\nu_3$  mode data in the latter part of this work.

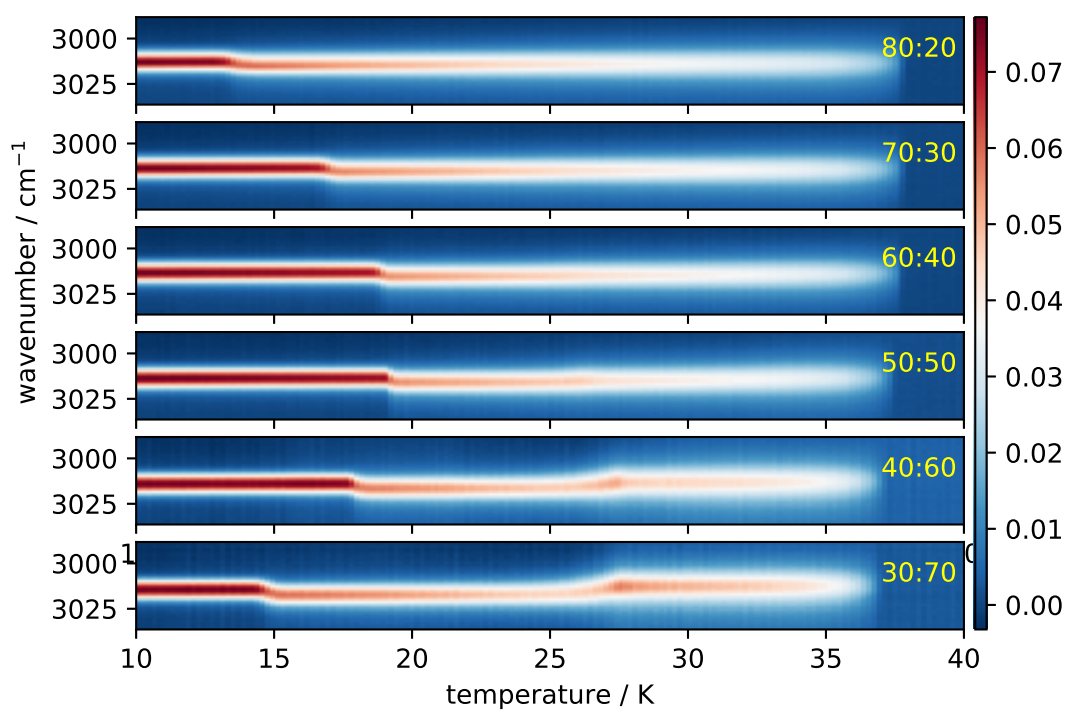


Figure 33: IR intensity map of  $\nu_3$  mode for the 1<sup>st</sup> transformation of a  $\text{CH}_4:\text{N}_2$  mixture with different mixing ratios

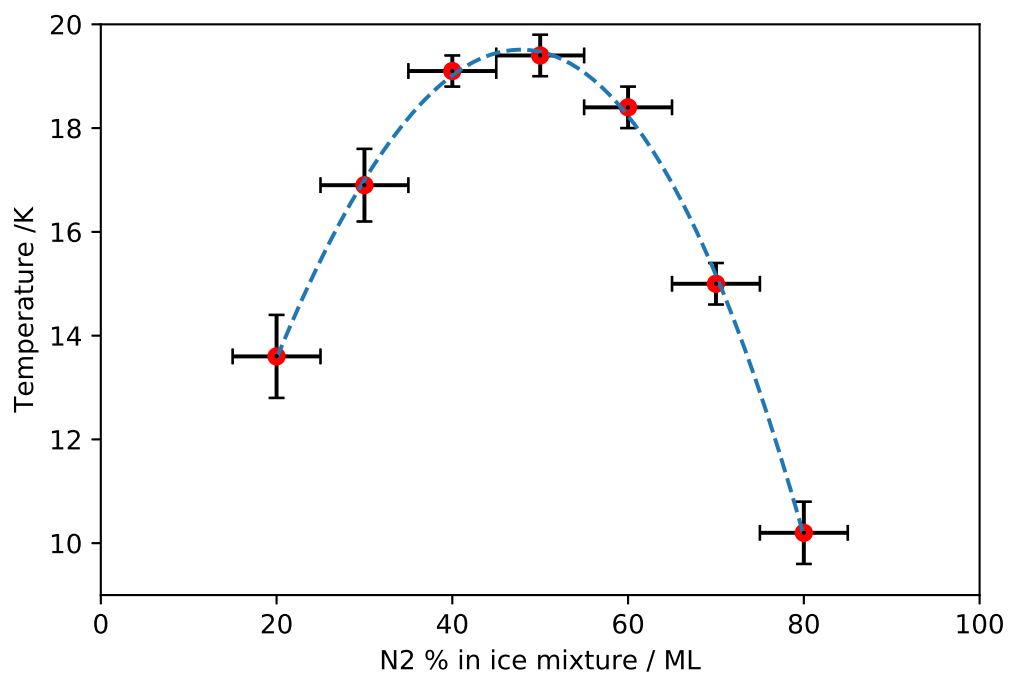


Figure 34: Fitting of the temperature of the 1<sup>st</sup> transformation of CH<sub>4</sub> and N<sub>2</sub> mixture with different mixing ratios with a quadratic equation. Error bars represent uncertainties in establishing the transition temperature and the fraction of N<sub>2</sub>.

### 5.4.5 Dependence of the 1<sup>st</sup> transformation on the mixing ratio

CH<sub>4</sub> and N<sub>2</sub> are present in different mixing ratios as observed in planetary ices. To disentangle the effects of mixing ratio from ice thickness and composition we performed several experiments based on the different mixing ratios of CH<sub>4</sub> and N<sub>2</sub>. The summary of these experiments is shown in Figure 33. We first observe the 1<sup>st</sup> transformation behavior for the mixture with 20 percent N<sub>2</sub>. We also observe 2<sup>nd</sup> transformation as the mole fraction of N<sub>2</sub> becomes 60 percent or more. The 1<sup>st</sup> transformation of ice takes place between 10 and 20 K depending on the mole fraction of CH<sub>4</sub> and N<sub>2</sub>. At first, we see a monotonic increase in transformation temperature until the ice has an even fraction of CH<sub>4</sub> and N<sub>2</sub>. As the ice becomes N<sub>2</sub> dominated, we observe a reversal in the trend of the transformation temperature, and it becomes close to 10 K as the ice is mostly dominated by N<sub>2</sub>. The transition temperature range and blue-shift data for the different mixing ratios of CH<sub>4</sub> and N<sub>2</sub> ice are presented in Table 1. We modeled the change in the transformation temperature with different mixing ratios by fitting the temperature with a quadratic equation as shown in Figure 34.

Ratio	Temp. (K)	Before(cm <sup>-1</sup> )	After(cm <sup>-1</sup> )	Blue shift
80:20	12.7-14.4	3013.2	3017.0	3.8
70:30	16.2-17.6	3013.3	3017.2	3.9
60:40	18.7-19.4	3013.4	3017.4	4.0
50:50	19.0-19.8	3013.6	3017.5	3.9
40:60	17.8-18.7	3013.8	3017.7	3.9
30:70	14.5-15.6	3014.0	3018.0	4.0
20:80	9.6-10.8	3014.3	3018.6	4.3

Table 6: Data of CH<sub>4</sub>: N<sub>2</sub> ice mixtures in the 1<sup>st</sup> transformation

### 5.4.6 Dependence of the 1<sup>st</sup> transformation on ice thickness

We found a correlation between ice thickness and 1<sup>st</sup> transformation temperature for certain mixing ratios of CH<sub>4</sub> and N<sub>2</sub>. Figure 35 1<sup>st</sup> transformation of CH<sub>4</sub>: N<sub>2</sub> takes place between 14.2-14.8 K for a 200 ML ice mixture. We observe an exponential increase in temperature range as we lower the ice thickness. For thicker ice (200 ML) the 1<sup>st</sup> transformation takes place close to the deposition temperature (10 K). In the case of thinner ice (5 ML), the 1<sup>st</sup> transformation can take place at the same temperature N<sub>2</sub> sublimates from the ice matrix. The thickness dependence of the 1<sup>st</sup> transformation has been modeled by fitting the temperature range for varying thickness with an exponential decay curve as shown in Figure 36.

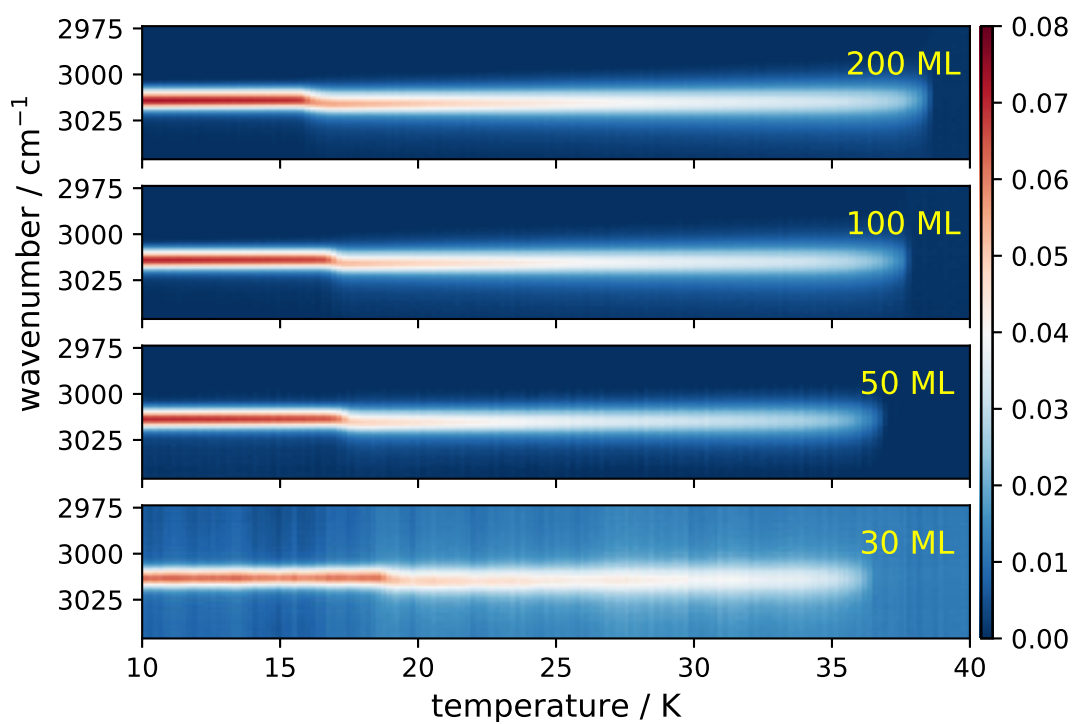


Figure 35: IR intensity map of the  $\nu_3$  mode for 1<sup>st</sup> transformation of a  $\text{CH}_4$  and  $\text{N}_2$  mixture with different film thickness

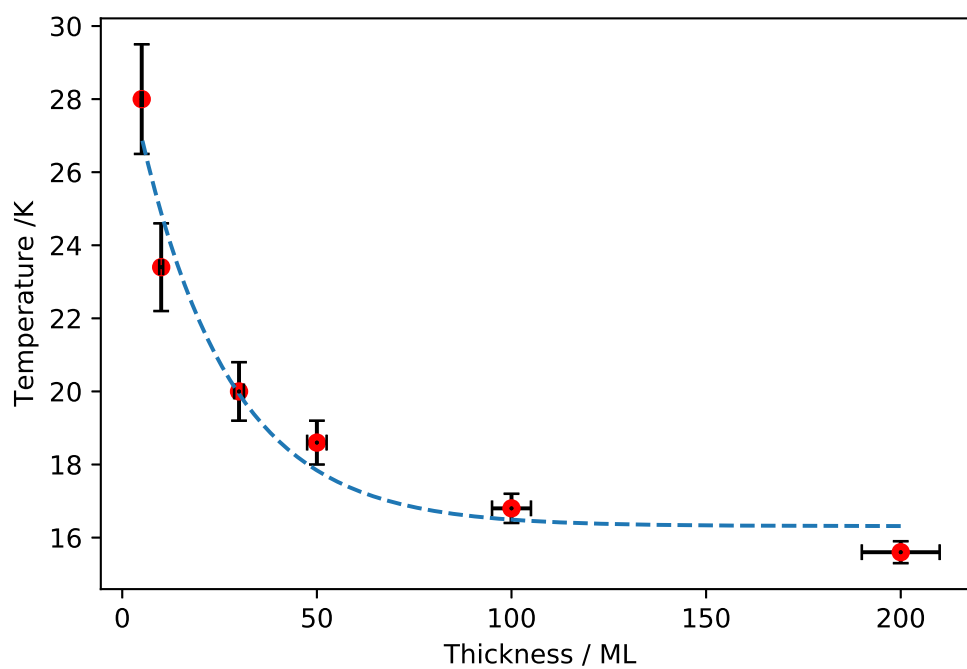


Figure 36: Fitting of the 1<sup>st</sup> transformation of CH<sub>4</sub> and N<sub>2</sub> mixture with different mixing ratios with an exponential decay curve.

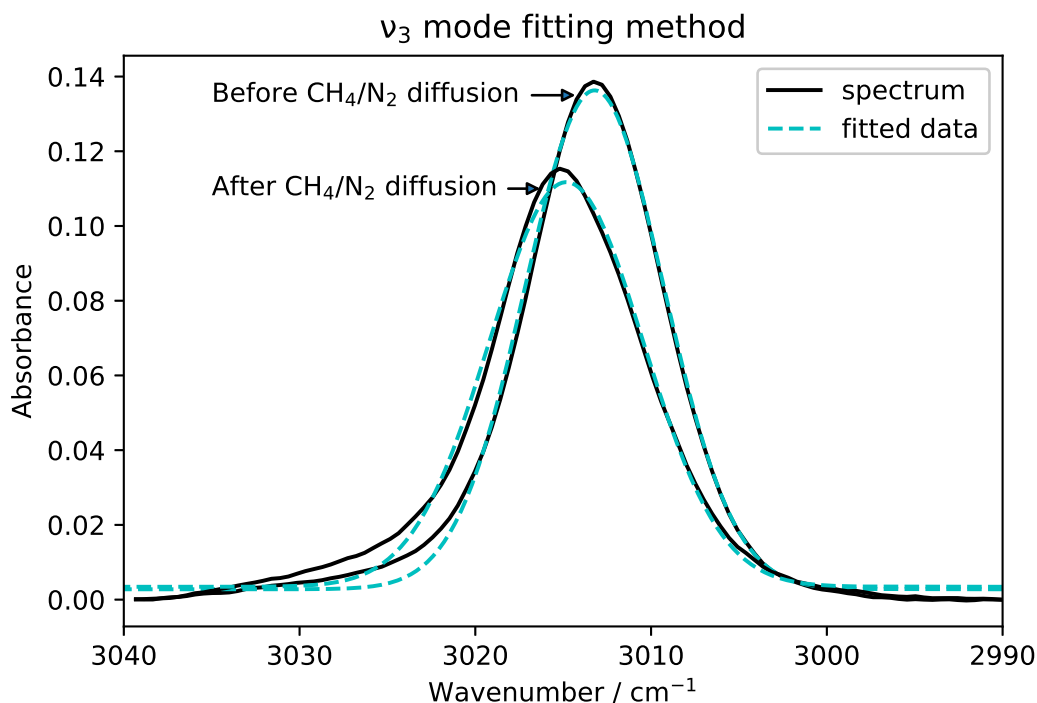


Figure 37: Fitting scheme of  $\nu_3$  mode in the isothermal experiment with a  $\text{CH}_4:\text{N}_2$  70:30 mixture.

#### 5.4.7 Activation energy of the 1<sup>st</sup> transformation

We have conducted several isothermal experiments with a  $\text{CH}_4:\text{N}_2$  70:30 mixture between 16.1 to 16.6 K to calculate the activation energy of the 1<sup>st</sup> transformation. This analysis is done in the  $\nu_3$  region, since the peak position of this mode shows a significant blue shift during the 1<sup>st</sup> transformation. To track the temporal change of  $\text{CH}_4$   $\nu_3$  mode peak position, each peak was fitted with a Gaussian spectral line shape as shown in Figure 37. An isothermal experiment with the shifted  $\nu_3$  mode peak position versus isothermal experiment time at 16.4 K is shown in Figure 38. After obtaining the activation rate values from the fitting, we use the Arrhenius expression as in Equation 5.1 to find the activation energy  $E_a$  for the 1<sup>st</sup> transformation in  $\text{CH}_4:\text{N}_2$ . In a  $\ln(\text{activation rate})$  versus  $1/T$  plot as in Equation 5.3, see Figure 39, data are fitted very well with the Arrhenius expression. The calculated activation energy for the 1<sup>st</sup> transformation is  $641 \pm 52$  K for a  $\text{CH}_4:\text{N}_2$  (70:30) mixture.

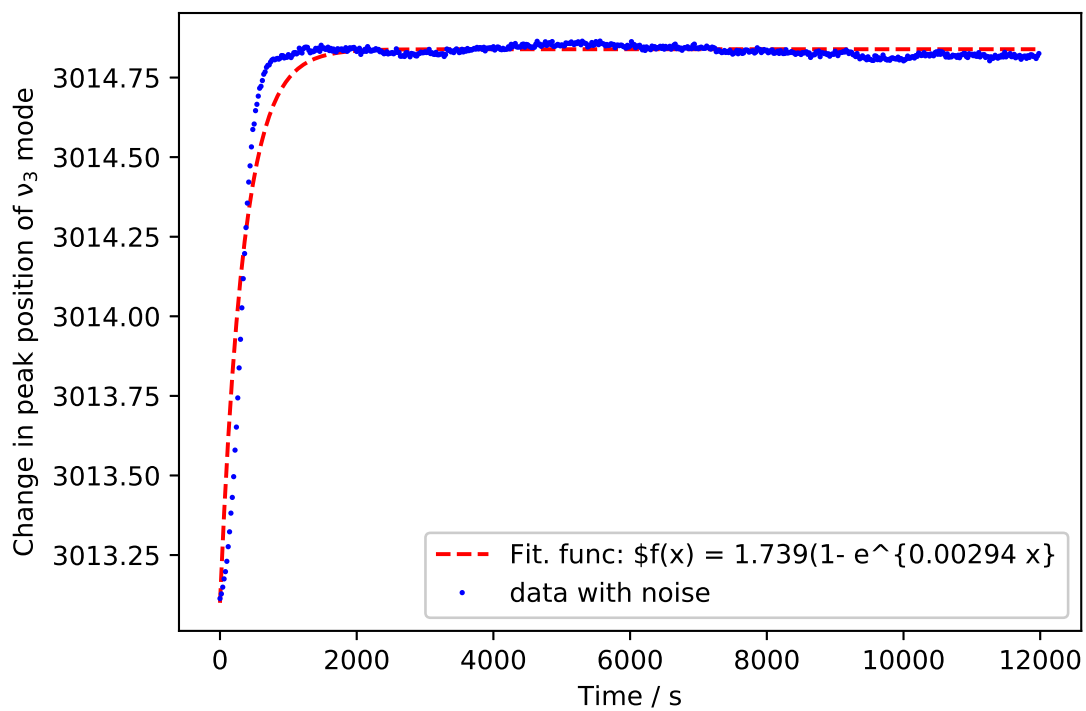


Figure 38: Temporal change of  $\nu_3$  mode peak position for 16.4 K isothermal experiment. The blue dots represent the data and the broken red line represents the fitting function.

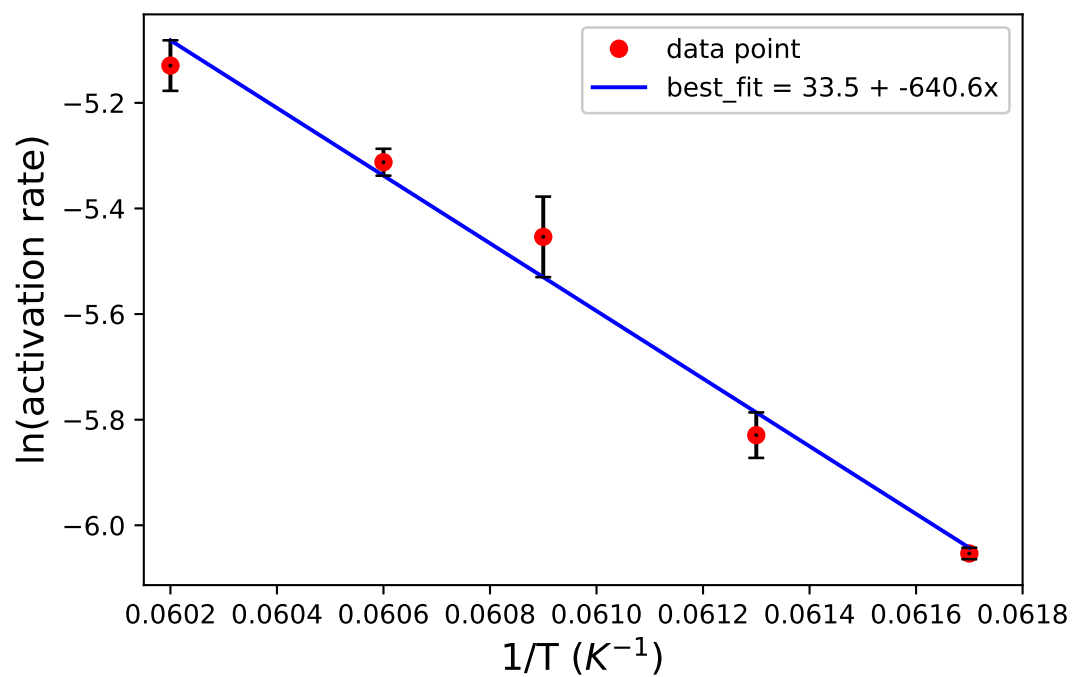


Figure 39: Arrhenius type plot for calculating the activation energy of 1<sup>st</sup> transformation of a CH<sub>4</sub> and N<sub>2</sub>= 70:30 mixture.

## 5.5 Summary

The present study shows laboratory simulations of the thermal processing of CH<sub>4</sub>:N<sub>2</sub> ice present on icy cold surfaces or inside the thick icy core of TNOs. In this study, we showed the infrared spectroscopic properties of methane and nitrogen ice mixtures at low temperatures. The study is based on the overlap of midIR and near-IR spectral range (650-5000 cm<sup>-1</sup>). The main conclusions we derive from this work are the following:

- CH<sub>4</sub>/N<sub>2</sub> ice mixture is important to probe the surface ice chemistry of TNOs. As N<sub>2</sub> is IR inactive, CH<sub>4</sub> IR profile provides the structural and morphological information of these type of mixture during thermal processing.
- The 1<sup>st</sup> transformation and 2<sup>nd</sup> transformation of CH<sub>4</sub> fundamental vibrational modes is related to the diffusion of CH<sub>4</sub>/N<sub>2</sub> in the ice matrix and N<sub>2</sub> sublimation in the ice mixture.
- The 1<sup>st</sup> transformation of CH<sub>4</sub>/N<sub>2</sub> in the ice matrix depends on the mole fraction. We observe a lower transformation temperature if the ice matrix is dominated by either CH<sub>4</sub> or N<sub>2</sub>.
- We observe a monotonic increase in 1<sup>st</sup> transformation temperature as the mole fraction of CH<sub>4</sub> and N<sub>2</sub> becomes even in the ice mixture as shown in Figure 34. We modeled this trend by fitting the temperature range of the 1<sup>st</sup> transformation with a quadratic equation.
- In N<sub>2</sub> dominated ice mixture, diffusion process is active upon deposition at 10 K. We observe the presence of the 2<sup>nd</sup> transformation as we increase the mole fraction of N<sub>2</sub> in the ice matrix.
- The effect of the film thickness of the ice mixture effects on the 1<sup>st</sup> transformation temperature is shown in Figure 35. We modeled this trend by fitting the temperature range of 1<sup>st</sup> transformation for varying thickness with an exponential decay curve.
- From the Arrhenius type plot we calculated the activation energy of the 1<sup>st</sup> transformation in the CH<sub>4</sub>:N<sub>2</sub>(70:30) mixture. The calculated activation energy is 641±52 K.

## Chapter 6

# Self-diffusion in $^{12}\text{CO}_2$ and $^{13}\text{CO}_2$ Thin Films

### 6.1 Abstract

Self-diffusion of  $\text{CO}_2$  in thin films was investigated using Infrared Spectroscopy. In our experiments, we found evidence that  $\text{CO}_2$  self-diffusion process in thin films is mostly dominated by bulk crystallization of the ice structure. We used the  $^{13}\text{CO}_2$  isotope as a probe to quantify the process. We found that diffusion of  $^{13}\text{CO}_2$  into  $^{12}\text{CO}_2$  ice is active for  $\leq 1$  ML coverage at 30 K, but not at 10K. Supporting deposition and slow heating data are presented. We found that  $\text{CO}_2$  actively diffuses in isotopically mixed and layer structured thin films in a temperature range between 30 and 50 K, depending on the mole fraction and layer formation. The morphological change during thermal processing of the asymmetrical stretching mode  $\nu_3$  of  $^{12}\text{CO}_2$  and  $^{13}\text{CO}_2$  supports this finding.

## 6.2 Introduction

Studies of molecular thin films have a wide range of applicability from fundamental physics and chemistry [74] to analyzing astrophysical ices [24]. Fourier-transform infrared (FTIR) spectroscopy is an effective tool to probe the characteristics of thin films. These process involve IR-absorption band evolution [79, 38], phase transition [25], crystallization [37, 92], diffusion [36, 39], physical change in structure [40], and chemical reactions [46] of molecules inside the thin film.

IR radiation can activate the long-range collective vibrations of optical phonons in the IR active solid. CO<sub>2</sub> thin film exhibits both transverse optical (TO) and longitudinal optical (LO) phonons in which the normal vibrations propagate through the ice lattice perpendicular and parallel to the direction of the IR field, respectively. The transverse optical ( $\nu_{TO}$ ) peaks of <sup>12</sup>CO<sub>2</sub> and <sup>13</sup>CO<sub>2</sub> thin films have been assigned at 2344 cm<sup>-1</sup> and 2281 cm<sup>-1</sup>; the longitudinal optical ( $\nu_{LO}$ ) peaks have been assigned at 2382 cm<sup>-1</sup> and 2314 cm<sup>-1</sup>, respectively [61]. When a thin film is positioned at a grazing angle to the incoming radiation, the electric field that has components both parallel and perpendicular to the film normal and longitudinal optical phonons can be excited by the parallel component of the field vector. In RAIRS experimental setup that uses grazing angle IR radiation of the thin film exhibits a strong absorption peak of LO phonon mode with a minuscule presence of TO phonon mode [8].

In this work, we describe the temperature evolution of diffusion in the <sup>12</sup>CO<sub>2</sub>-<sup>13</sup>CO<sub>2</sub> thin film for pre-mixed, sandwiched, and layered structure of ice matrix. We also show the temperature dependence for this process.

## 6.3 Background Work

The effect of isotope presence, dimer formation, and shape of molecules in the CO<sub>2</sub> particle has been shown experimentally and theoretically [77, 75, 76, 4]. Signorell and Jetzki [76] in Figure 1 shows that crystalline globular particles and elongated particles can have significant differences in IR absorption peaks, while mixed particles in the ice matrix exhibit irregular IR absorption peaks without any distinct peak. Signorell and Kunzmann [77] in Figure 1 showed the emergence of several peaks in isotopically mixed <sup>12</sup>CO<sub>2</sub>/<sup>13</sup>CO<sub>2</sub> particles. We have named the LO phonon mode 'LO' and the TO phonon mode 'TO' in further discussion of this chapter. In addition, we named the main intermediate peak 'M' and the subsidiary peak 'S' in the following Figures.

Self-diffusion of CO<sub>2</sub> has been experimentally shown in nano-particles produced in a cooling chamber at 78 K [3]. In these experiments Bauerecker [3] sent a pulse of <sup>12</sup>CO<sub>2</sub> followed by one of <sup>13</sup>CO<sub>2</sub> in a cooling cell and observed the time evolution of the nanoparticle composed of <sup>12</sup>CO<sub>2</sub>

(mantle) and  $^{13}\text{CO}_2$  (core) or vice-versa in the case the sequence of pulsed was reversed. When both pulses were sent in the cooling chamber at the same time, an uniform mix was obtained. In the case of thin films, we can expect isotopic guest molecules interact with host molecules and diffuse into each other. In IR spectroscopy, asymmetric stretching and bending modes of molecules serve as the primary indicator of the macroscopic structure of thin-film morphology while the combination band and overtones bands provide the microscopic structure information. The self-diffusion in the ice matrix is supported by the evolution of the asymmetric stretching ( $\nu_3$ ) and combination bands ( $\nu_1+\nu_3$ ).

## 6.4 Experimental Methods

A detailed description UHV apparatus is given in Chapter 2 of this thesis as well as prior published works [37]; here only the main features that are relevant to this study are summarized. In most of the cases, for deposition of  $^{12}\text{CO}_2$  and  $^{13}\text{CO}_2$ , UHV precision leak valve and molecular beam was used both for co-deposition and sequential deposition. For these experiments, the majority species of the formed  $\text{CO}_2$  ice was sent through the UHV leak valve, and minority species were sent through the molecular beamline. In all experiments, 100 monolayers or 20 monolayers (ML, defined as  $10^{15}$  molecules/cm<sup>2</sup>) of ice were grown at varying deposition rates. This deposition dose was calculated using the impingement rate, see Chapter 2 for details.

## 6.5 Results and Analysis

We carried out mainly three sets of experiments. In the first set, -the layered ice structure experiment (Figure 40) - we deposited 10 ML  $^{12}\text{CO}_2$  from the background gas using the UHV leak valve, then deposited 2 ML  $^{13}\text{CO}_2$  using the beamline, and then deposited 10 ML  $^{12}\text{CO}_2$  again using the UHV leak valve to form a sandwich structure of  $^{12}\text{CO}_2/^{13}\text{CO}_2/^{12}\text{CO}_2$  ice. In the second set, we studied the temperature dependence of IR absorption bands of co-deposited  $^{12}\text{CO}_2$  and  $^{13}\text{CO}_2$  with different mole fractions (Figure 41). In the third set (Figures 42 and 43), we first deposited 20 ML of  $^{12}\text{CO}_2$  at 10 K and 30 K, annealed the ice at 65 K for 30 min, and cooled it back down to the original deposition temperature. On top of the 20 ML  $^{12}\text{CO}_2$  surface we deposited 0.5, 1.0, and 5.0 ML  $^{13}\text{CO}_2$  and did a slow heating up experiment.

### 6.5.1 Self diffusion in layered ice

Figure 40 shows the change of the asymmetrical stretching  $\nu_3$  mode of  $\text{CO}_2$  and its isotope for the  $^{12}\text{CO}_2/^{13}\text{CO}_2/^{12}\text{CO}_2$  layered structure between 20 to 70 K while being heated from 10 to 110 K. The ice structure was prepared by depositing 10 ML  $^{12}\text{CO}_2$  using the UHV leak valve, then 2 ML  $^{13}\text{CO}_2$  using the beamline, and then 10 ML  $^{12}\text{CO}_2$  again using the UHV leak valve to form a layered/sandwich structure of  $^{12}\text{CO}_2/^{13}\text{CO}_2$  ice. In this case, the main LO peak position blue-shifts continuously from  $2376\text{ cm}^{-1}$  to  $2382\text{ cm}^{-1}$  due to bulk crystallization of the ice structure between 20 to 70 K [37]. In addition, we observe the formation of the M peak of  $^{12}\text{CO}_2$  at  $2372\text{ cm}^{-1}$  due to the interaction of  $^{13}\text{CO}_2$  and  $^{12}\text{CO}_2$  in the sandwich layer region at  $\approx 30\text{ K}$ . Between 30 and 50 K this intermediate peak sharpens; and beyond 50 K begins to broaden. In between 50 and 70 K, we also observe an intermediate shoulder S and the TO peak at  $2364\text{ cm}^{-1}$  and  $2344\text{ cm}^{-1}$ , respectively. In the case of  $^{13}\text{CO}_2$ , we observe that LO and TO peaks sharpen between 20 K and 30 K which is an indication of crystallization in the ice.

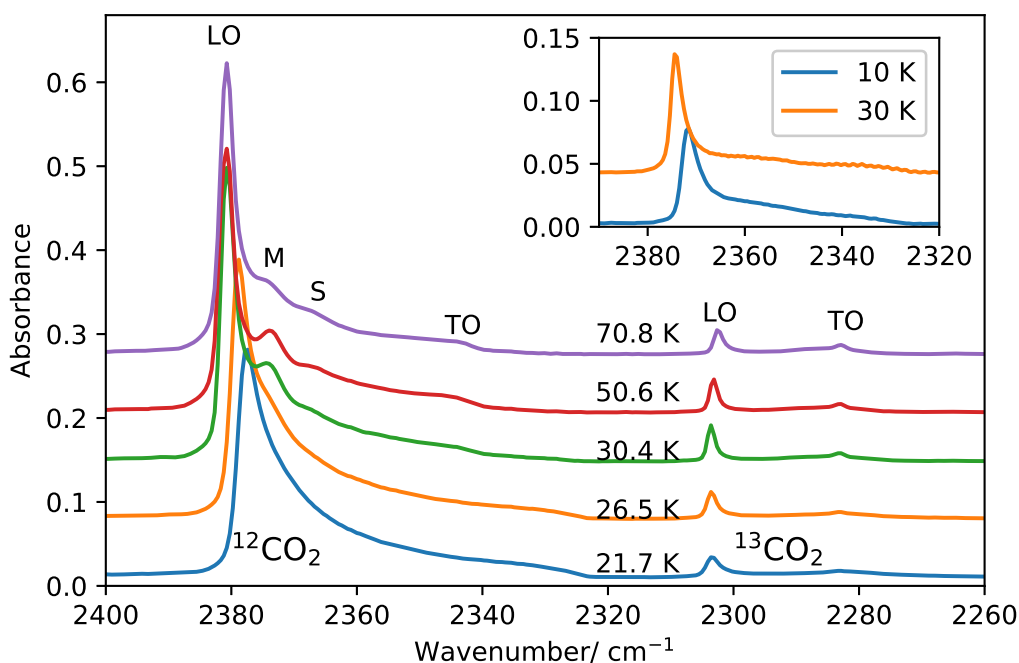


Figure 40: Slow heating up experiment of 22 ML of  $^{12}\text{CO}_2/^{13}\text{CO}_2/^{12}\text{CO}_2$  (10 ML/2 ML/10 ML) layer/sandwich structured ice deposited at 10 K. The plot shows the morphological change and formation of several peaks (LO, TO, M, and S) of  $^{12}\text{CO}_2$  and  $^{13}\text{CO}_2$ . The inset shows IR traces of 20 ML  $^{12}\text{CO}_2$  deposited at 10 K and 30 K.

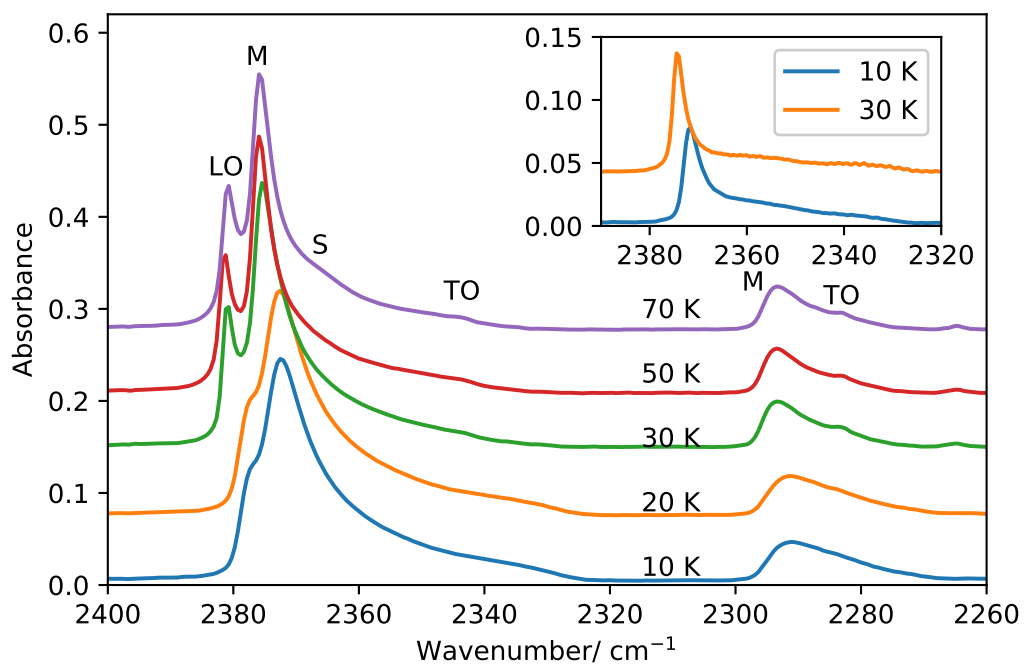


Figure 41: Slow heating up experiment of 100 ML of  $^{12}\text{CO}_2$ : $^{13}\text{CO}_2$  =95:5 mixture ice deposited at 10 K. This plot shows the change of  $^{12}\text{CO}_2$  and  $^{13}\text{CO}_2$  asymmetrical stretching  $\nu_3$  mode with rising temperature. The inset diagram shows the IR traces of 20 ML  $^{12}\text{CO}_2$  deposited at 10 K and 30 K.

### 6.5.2 Slow heating up of $^{12}\text{CO}_2$ and $^{13}\text{CO}_2$ mixture

Figure 41 shows the change of the asymmetrical stretching  $\nu_3$  mode of  $\text{CO}_2$  and its isotope in  $^{12}\text{CO}_2$ : $^{13}\text{CO}_2$  =95:5 mixture deposited at 10 K. He et al. [37] showed that bulk amorphous to crystalline transformation in  $\text{CO}_2$  thin-film happens between 20 and 30 K due to reorientation of molecules in the ice matrix. In Figure 41, we see a significant change between 20 and 30 K due to the ordering transition of  $\text{CO}_2$  molecules in  $\nu_3$  asymmetrical stretching mode. After the crystalline transformation process is completed at 30 K, the  $\nu_3$  asymmetrical stretching mode forms a double peak (M and LO) at  $2376\text{ cm}^{-1}$  and  $2381\text{ cm}^{-1}$ , respectively. In addition, we observe that a bump shows up in the 30 K IR trace at  $2344\text{ cm}^{-1}$  (TO) and at 50 K a sloping plateau appears at  $2367\text{ cm}^{-1}$  (S) in the extended tail of the main peak. In the case of the  $^{13}\text{CO}_2$  IR trace, the M peak blue-shifts from  $2292\text{ cm}^{-1}$  to  $2296\text{ cm}^{-1}$  and the TO peak ( $^{13}\text{CO}_2$ ) shows up at  $2282\text{ cm}^{-1}$  between 20 and 30 K. Bauerecker [3] showed the formation of core and mantle in  $^{12}\text{CO}_2$  and  $^{13}\text{CO}_2$  nanoparticles depending on the order that the pulses of gas are sent in the cooling chamber. In his experiment, the peak at  $2375\text{ cm}^{-1}$  is formed due to the core formation of  $^{12}\text{CO}_2$  in the  $^{12}\text{CO}_2$  and  $^{13}\text{CO}_2$  ice mixture. In this study of the temperature evolution of the thin film, we see a transformation from the blunt single peak of the  $\nu_3$  mode to the distinct double-peak feature characteristic of intermixing, see also Figure 40.

### 6.5.3 Temperature dependence of $\text{CO}_2$ diffusion

Diffusion in  $\text{CO}_2$  thin films is dependent on the deposition temperature. Figure 42 shows the comparison of a low dose of  $^{13}\text{CO}_2$  grown on top of 20 ML of  $^{12}\text{CO}_2$  surface at 10 K and 30 K. The underlying 20 ML crystalline  $^{12}\text{CO}_2$  surface was prepared either at 10 K or 30 K, heated up and annealed at 65 K for 30 min, and cooled back down 10 or 30 K before  $^{13}\text{CO}_2$  dosing. For both  $^{13}\text{CO}_2$  deposited at 10 K (left column) or 30 K (right column), we observe that the TO peak of  $^{13}\text{CO}_2$  at  $2282\text{ cm}^{-1}$  is already present due to the natural abundance of  $^{13}\text{CO}_2$  in  $^{12}\text{CO}_2$ . In the case of 10 K deposition temperature for 0.5, 1.0, and 5.0 ML, the LO peak blue-shifts to higher wavenumber which is consistent with multi-layer formation. On the other hand, we observe wide, irregular peak features in case 0.5 and 1.0 ML deposition of  $^{13}\text{CO}_2$  at 30 K due to interdiffusion between  $^{13}\text{CO}_2$  and  $^{12}\text{CO}_2$ . As we increase the coverage to 5 ML, the IR absorbance feature becomes similar to 10 K data which is typical of bulk  $\text{CO}_2$ .

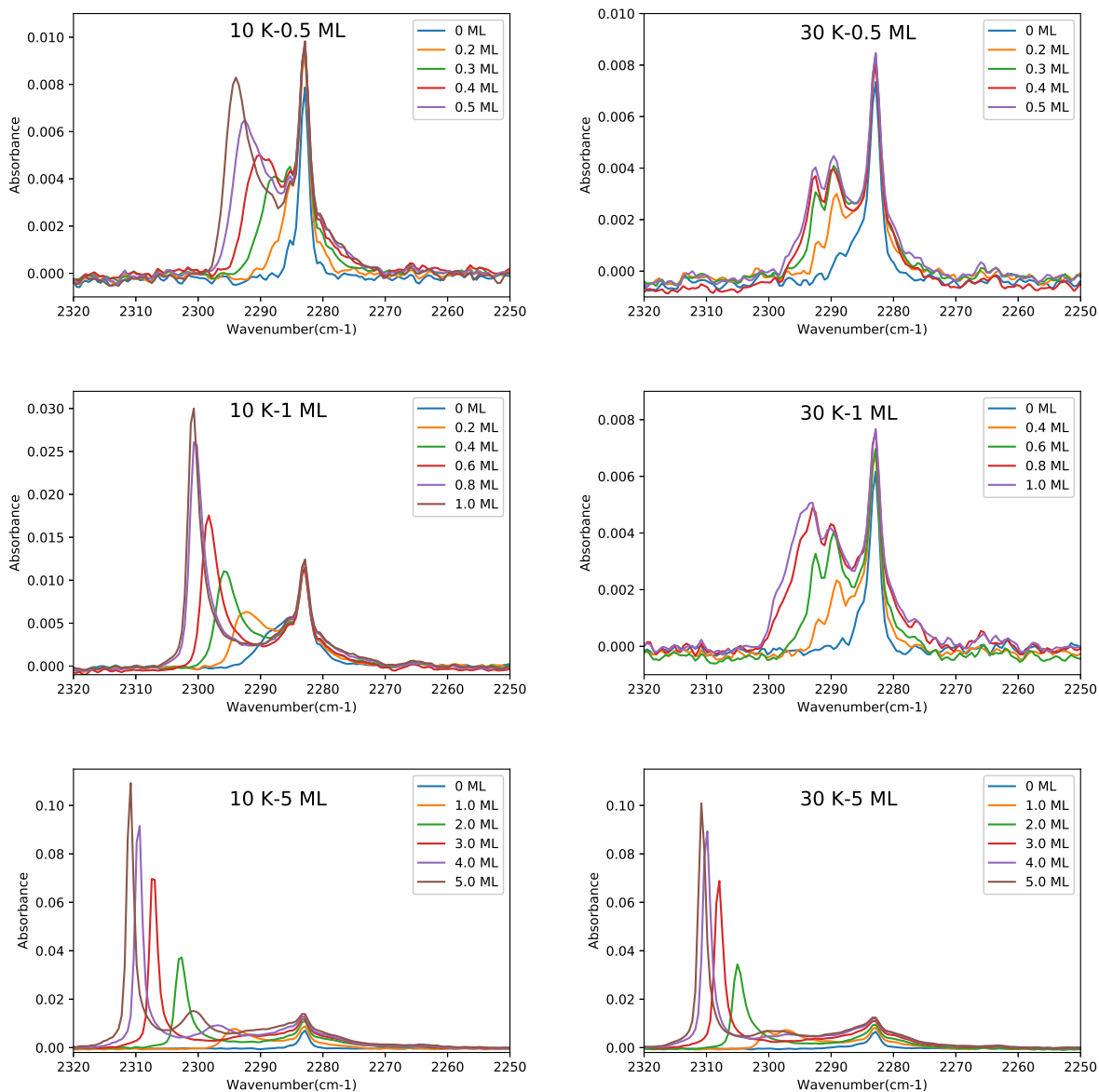


Figure 42: Comparison of slow deposition experiment for 0.5, 1.0, and 5.0 ML  $^{13}\text{CO}_2$  deposited on top of 20 ML  $^{12}\text{CO}_2$  ice at 10 K (left panels) and 30 K (right panels). In both cases 20 ML  $^{12}\text{CO}_2$  ice was deposited at 10 K, heated up and annealed at 65 K for 30 min, and cooled back down to respective temperature before  $^{13}\text{CO}_2$  deposition.

### 6.5.4 Dependence of CO<sub>2</sub> diffusion on the underlying surface

There is a correlation between surface diffusion of CO<sub>2</sub> and underlying surface morphology. Although annealing the underlying 20 ML <sup>12</sup>CO<sub>2</sub> surface at 65 K in both cases increases the degree of crystallinity [37], at 30 K surface <sup>12</sup>CO<sub>2</sub> molecules are still mobile and actively interact with the underlying <sup>13</sup>CO<sub>2</sub> molecules. Figure 43 shows the heating of 1 ML <sup>13</sup>CO<sub>2</sub> deposited on 20 ML <sup>12</sup>CO<sub>2</sub> between the deposition temperature (10 and 30 K) and 85 K. As the the underlying <sup>12</sup>CO<sub>2</sub> molecules are less mobile, for 10 K deposited 1ML <sup>13</sup>CO<sub>2</sub> more energy is required for diffusion of the top layer into the underlying ice. In the case of 1ML <sup>13</sup>CO<sub>2</sub> deposited at 30 K, a cluster forms between 50 K and 75 K, see the left panel of Figure 43. On the other hand, we don't observe any significant change in the IR band in a similar temperature range for 1ML <sup>13</sup>CO<sub>2</sub> deposited at 30 K.

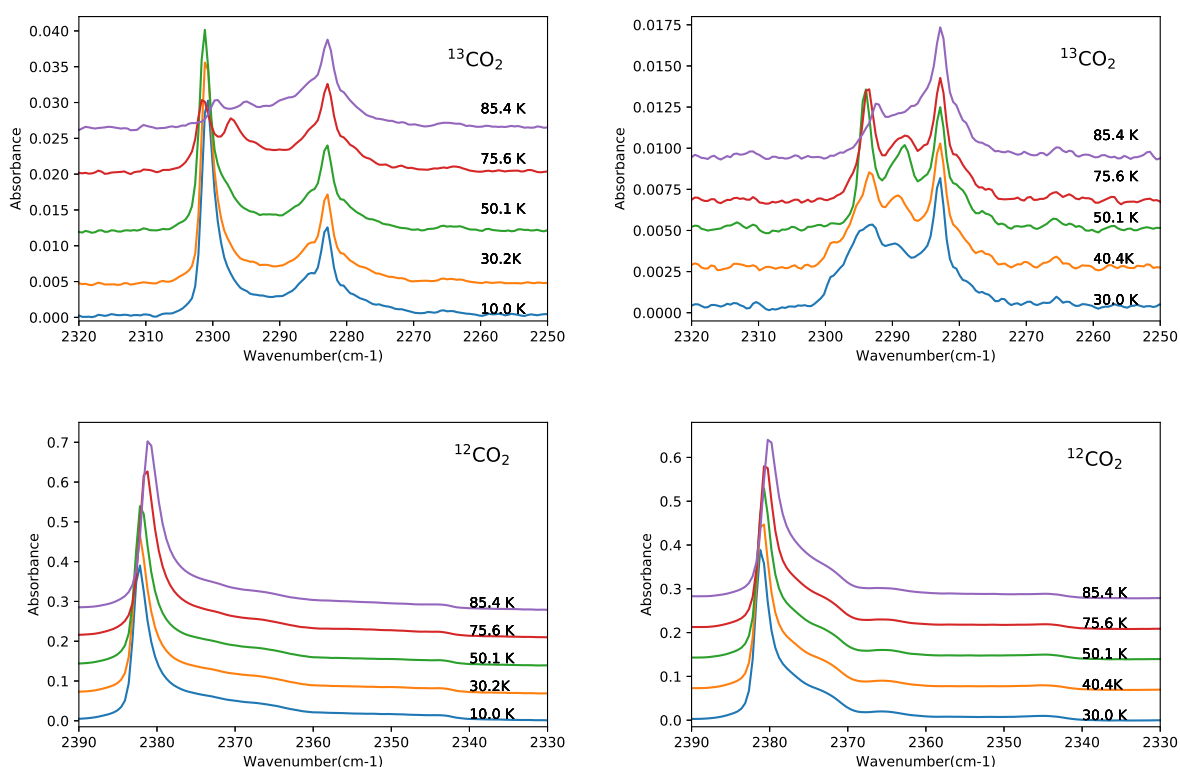


Figure 43: Comparison of slow heating up experiment for 1 ML <sup>13</sup>CO<sub>2</sub> deposited at 10 K (left) and 30 K (right) on top of 20 ML <sup>12</sup>CO<sub>2</sub> ice as shown in Figure 42. This diagram shows the change of <sup>13</sup>CO<sub>2</sub> and <sup>12</sup>CO<sub>2</sub> asymmetric stretching mode  $\nu_3$  between 10 K (or 30 K) and 85 K during the slow heating up process.

## 6.6 Discussion

The emergence of several peaks in the  $\nu_3$  band in isotopically mixed  $^{12}\text{CO}_2/^{13}\text{CO}_2$  thin films requires three conditions. First, it requires the presence of resonance enhancement or resonance coupling among molecules in neighboring unit cells in the ice matrix. For this reason, distinct peaks in evenly mixed  $^{12}\text{CO}_2/^{13}\text{CO}_2$  nano-particles are not observed [4]. Second, these intermediate peaks show up only for a certain range of sizes of the particles. These peaks are not present for bulk  $\text{CO}_2$  ice even though there is resonance coupling between nearest neighbors, see inset of Figure 40 and [77]. In our experiment, we define  $\leq 100$  ML as a thin film and all our experiments were conducted within that limit. Finally, it depends on the shape of the  $\text{CO}_2$  molecule in the thin film. The experiments in Figure 42 and Figure 43 were done with the sequential deposition of  $^{13}\text{CO}_2$  on top of 20 ML  $^{12}\text{CO}_2$ . The underlying 20 ML  $^{12}\text{CO}_2$  is already in crystalline form due to the annealing treatment (warm up to 65 K, and cool back down). The only difference is the deposition temperature of  $^{13}\text{CO}_2$  (10 K and 30 K). At 30 K the self-swapping within underlying  $^{12}\text{CO}_2$  ice is active. Upon deposition,  $^{13}\text{CO}_2$  replaces some of the  $^{12}\text{CO}_2$  molecules in the unit cells of the surface of crystalline  $^{12}\text{CO}_2$ . We observe the emergence of peaks in  $^{13}\text{CO}_2$  bands that indicates resonant coupling among surface  $^{13}\text{CO}_2$  molecules at 30 K. This formation of resonant coupling in  $^{13}\text{CO}_2$  network is the evidence of self-diffusion of  $^{13}\text{CO}_2$  into  $^{12}\text{CO}_2$  ice upon deposition at 30 K as shown in Figure 42. From the emergence of multiple peaks, we conclude that there is a swapping of  $^{13}\text{CO}_2$  surface molecules with  $^{12}\text{CO}_2$  of the underlying ice. We don't observe a significant change in the  $^{13}\text{CO}_2$  IR spectrum during the slow heating up from 30 K until the ice desorbs as shown in the right panel of Figure 43. On the other hand, at 10 K we observe ordered layer formation for  $^{12}\text{CO}_2$  at low coverage ( $\leq 1\text{ML}$ ) [36]. In this case the self-swapping between  $^{13}\text{CO}_2$  and  $^{12}\text{CO}_2$  gets activated between 51.4 K and 75.6 K as shown in the left panel of Figure 43.

The layered structure of  $^{12}\text{CO}_2/^{13}\text{CO}_2$  also hints self-diffusion due to the swapping of lattice sites while the ice is being warmed past 30 K. In this case the resonance coupling of  $^{13}\text{CO}_2$  with neighboring  $^{13}\text{CO}_2$  increases as the sandwich layer gets enough energy to replace the  $^{12}\text{CO}_2$  at lattice sites during the thermal processing experiments. The isotopic mixture of  $^{12}\text{CO}_2/^{13}\text{CO}_2$  doesn't show self-diffusion in the ice matrix if deposited at  $\leq 30$  K as the process is being shadowed by the bulk crystallization between 20 to 30 K [37].

## 6.7 Summary

This chapter presents the first investigation of the temperature evolution of self-diffusion phenomena in  $^{12}\text{CO}_2/^{13}\text{CO}_2$  thin films. It reports the physical process and temperature range for self-diffusion in  $\text{CO}_2$  layer structured thin films. In addition, self-diffusion of  $\text{CO}_2$  molecules in sequentially deposited ice has also been investigated. The main conclusions we derive from this work are the following:

- Bulk crystallization and self-diffusion in the thin film of  $\text{CO}_2$  molecules take place in different temperature ranges, depending on the thin film geometry.
- Evidence of self diffusion of  $\text{CO}_2$  in  $\text{CO}_2$  ice is obtained from the IR  $\nu_3$  band changes from a blunt single peak feature to distinct double peak feature.
- In the case of the layered structure, self-diffusion is observable at a lower temperature, between 30 to 50 K.
- Self-diffusion of  $\text{CO}_2$  molecules is temperature dependent. We observe that at 30 K the self-diffusion/swapping of  $\text{CO}_2$  molecules is active, but not at 10 K.
- The self-diffusion  $\text{CO}_2$  molecules on the surface of ice is dependent on underlying surface morphology. It takes more energy (i.e. higher temperature) to ignite the process if the underlying surface is prepared at a lower temperature (10 K vs. 30 K).

# Chapter 7

## Conclusions

### **7.1 Infrared Spectroscopic Study of Solid Methane: Nuclear Spin Conversion of Stable and Metastable Phases (Chapter 3)**

I studied thin films of CH<sub>4</sub> ice in order to characterize the change in their properties due to thermal changes and deposition methods. A new metastable phase has been identified, and the process of Nuclear Spin Conversion rates and conditions for NSC occurrence have been characterized in greater detail and under wider conditions than before.

### **7.2 Infrared Spectroscopic Study of Crystalline Methane Solid and Methane Mixture with Polar and Non-polar Molecules (Chapter 4)**

I conducted experiments to measure the characteristics and thermal evolution of pure methane ices and the influence of these properties by the addition of polar and non-polar molecules.

### **7.3 Temperature Evolution of CH<sub>4</sub>:N<sub>2</sub> Ice Mixture - an Application to trans-Neptunian Objects (Chapter 5)**

In this investigation, I extended the studies of the properties and thermal evolution of CH<sub>4</sub> ices described in the preceding chapter to ices of CH<sub>4</sub> mixed with polar (H<sub>2</sub>O) and non-polar (N<sub>2</sub>) molecules, in conditions that are relevant to interpret observations of interstellar and outer solar system ices. These results will be useful to astronomers and modelers of the evolution of space environments when data of the soon to be launched James Webb Space Telescope (JWST) will become available.

## 7.4 Self Diffusion in $^{12}\text{CO}_2$ and $^{13}\text{CO}_2$ Thin Film (Chapter 6)

I studied the process of self diffusion in thin film ices. This process is important in order to understand the thermal evolution of ices and the formation of molecules in ices via diffusion of reactants. Thin films of isotopes of  $\text{CO}_2$  (one of the major components in interstellar ices) in various geometries were studied using mid IR spectroscopy. I found that inter-diffusion of the minority isotope is promoted by both bulk diffusion as well by the preparation methods of the ice of the majority isotope. In the latter case, the lower deposition temperature (10 K vs. 30 K) yields to a different state of aggregation of the minority isotope.

# Bibliography

- [1] Matthew J. Abplanalp, Brant M. Jones, and Ralf I. Kaiser. Untangling the methane chemistry in interstellar and solar system ices toward ionizing radiation: a combined infrared and reflectron time-of-flight analysis. *Physical Chemistry Chemical Physics (Incorporating Faraday Transactions)*, 20:5435–5468, Feb 2018. doi: 10.1039/C7CP05882A.
- [2] Kinsuk Acharyya and Eric Herbst. Hot Cores in Magellanic Clouds. , 859(1):51, May 2018. doi: 10.3847/1538-4357/aabaf2.
- [3] Sigurd Bauerecker. Self-Diffusion in Core-Shell Composite  $^{12}\text{CO}_2/^{13}\text{CO}_2$  Nanoparticles. , 94(3):033404, January 2005. doi: 10.1103/PhysRevLett.94.033404.
- [4] Sigurd Bauerecker, Michael Taraschewski, Claus Weitkamp, and Heiko K. Cammenga. Liquid-helium temperature long-path infrared spectroscopy of molecular clusters and super-cooled molecules. *Review of Scientific Instruments*, 72(10):3946–3955, October 2001. doi: 10.1063/1.1400158.
- [5] Arnaud Belloche. Exploring Molecular Complexity in the Interstellar Medium with Alma. In *72nd International Symposium on Molecular Spectroscopy*, page MF02, June 2017. doi: 10.15278/isms.2017.MF02.
- [6] Max P. Bernstein, Scott A. Sandford, Louis J. Allamandola, Sherwood Chang, and Maureen A. Scharberg. Organic Compounds Produced by Photolysis of Realistic Interstellar and Cometary Ice Analogs Containing Methanol. , 454:327, November 1995. doi: 10.1086/176485.
- [7] Max P. Bernstein, Dale P. Cruikshank, and Scott A. Sandford. Near-infrared spectra of laboratory  $\text{H}_2\text{O}-\text{CH}_4$  ice mixtures. , 181(1):302–308, March 2006. doi: 10.1016/j.icarus.2005.10.021.
- [8] D. W. Berreman. Infrared Absorption at Longitudinal Optic Frequency in Cubic Crystal Films. *Physical Review*, 130(6):2193–2198, June 1963. doi: 10.1103/PhysRev.130.2193.

- [9] T. Bertrand, F. Forget, O. M. Umurhan, J. M. Moore, L. A. Young, S. Protopapa, W. M. Grundy, B. Schmitt, R. D. Dhingra, R. P. Binzel, A. M. Earle, D. P. Cruikshank, S. A. Stern, H. A. Weaver, K. Ennico, C. B. Olkin, and New Horizons Science Team. The CH<sub>4</sub> cycles on Pluto over seasonal and astronomical timescales. , 329:148–165, September 2019. doi: 10.1016/j.icarus.2019.02.007.
- [10] Geoffrey A. Blake, E. C. Sutton, C. R. Masson, and T. G. Phillips. Molecular Abundances in OMC-1: The Chemical Composition of Interstellar Molecular Clouds and the Influence of Massive Star Formation. , 315:621, April 1987. doi: 10.1086/165165.
- [11] Dominique Bockelée-Morvan, Ursina Calmonte, Steven Charnley, Jean Duprat, Cécile Engrand, Adeline Gicquel, Myrtha Hässig, Emmanuël Jehin, Hideyo Kawakita, Bernard Marty, Stefanie Milam, Andrew Morse, Philippe Rousselot, Simon Sheridan, and Eva Wirström. Cometary Isotopic Measurements. , 197(1-4):47–83, Dec 2015. doi: 10.1007/s11214-015-0156-9.
- [12] A. C. A. Boogert, W. A. Schutte, F. P. Helmich, A. G. G. M. Tielens, and D. H. Wooden. Infrared observations and laboratory simulations of interstellar CH<sub>4</sub> and SO<sub>2</sub>. , 317: 929–941, Feb 1997.
- [13] A. C. A. Boogert, G. A. Blake, and K. Öberg. Methane Abundance Variations toward the Massive Protostar NGC 7538 IRS 9. , 615(1):344–353, November 2004. doi: 10.1086/423979.
- [14] A. C. Adwin Boogert, Perry A. Gerakines, and Douglas C. B. Whittet. Observations of the icy universe. *Annu.Rev.Astron. Astrophys.*, 53:541–581, Aug 2015. doi: 10.1146/annurev-astro-082214-122348.
- [15] Saps Buchman, Donald Candela, William T. Vetterling, and R. V. Pound. Spin-species conversion rate in solid CH<sub>4</sub> in the temperature range 4-23 K. *Physical Review B*, 26(3):1459–1461, Aug 1982. doi: 10.1103/PhysRevB.26.1459.
- [16] Daren J. Burke and Wendy A. Brown. Ice in space: surface science investigations of the thermal desorption of model interstellar ices on dust grain analogue surfaces. *Physical Chemistry Chemical Physics (Incorporating Faraday Transactions)*, 12(23):5947, January 2010. doi: 10.1039/b917005g.

- [17] Patrice Cacciani, Jean Cosléou, Mohamed Khelkhal, Peter Čermák, and Cristina Puzzarini. Nuclear Spin Conversion in CH<sub>4</sub>: A Multichannel Relaxation Mechanism. *Journal of Physical Chemistry A*, 120(2):173–182, Jan 2016. doi: 10.1021/acs.jpca.5b09454.
- [18] C. Chapados and A. Cabana. Infrared spectra and structures of solid CH<sub>4</sub> and CD<sub>4</sub> in phases I and II. *Canadian Journal of Chemistry*, 50:3521–3533, Jan 1972.
- [19] P. L. Chapovsky and L. J. F. Hermans. Nuclear Spin Conversion in Polyatomic Molecules. *Annual Review of Physical Chemistry*, 50:315–345, Oct 1999. doi: 10.1146/annurev.physchem.50.1.315.
- [20] S. B. Charnley, M. E. Kress, A. G. G. M. Tielens, and T. J. Millar. Interstellar Alcohols. , 448:232, July 1995. doi: 10.1086/175955.
- [21] Roger N. Clark, Robert Carlson, Will Grundy, and Keith Noll. *Observed Ices in the Solar System*, pages 3–46. Springer New York, New York, NY, 2013. ISBN 978-1-4614-3076-6. doi: 10.1007/978-1-4614-3076-6\_1. URL [https://doi.org/10.1007/978-1-4614-3076-6\\_1](https://doi.org/10.1007/978-1-4614-3076-6_1).
- [22] E. Dartois. Dust Formation, Composition and Evolution. In C. Lidman and D. Alloin, editors, *The Cool Universe: Observing Cosmic Dawn*, volume 344 of *Astronomical Society of the Pacific Conference Series*, page 113, December 2005.
- [23] S. Douté, B. Schmitt, E. Quirico, T. C. Owen, D. P. Cruikshank, C. de Bergh, T. R. Geballe, and T. L. Roush. Evidence for Methane Segregation at the Surface of Pluto. , 142(2):421–444, December 1999. doi: 10.1006/icar.1999.6226.
- [24] P. Ehrenfreund, A. C. A. Boogert, P. A. Gerakines, A. G. G. M. Tielens, and E. F. van Dishoeck. Infrared spectroscopy of interstellar apolar ice analogs. , 328:649–669, December 1997.
- [25] Shahnewaz M. Emtiaz, Francis Toriello, Jiao He, and Gianfranco Vidali. Infrared spectroscopic study of solid methane: Nuclear spin conversion of stable and metastable phases. *Journal of Physical Chemistry A*, 124(3):552–559, January 2020. ISSN 1089-5639. doi: 10.1021/acs.jpca.9b10643.
- [26] J. H. Fillion, M. Bertin, A. Lekic, A. Moudens, L. Philippe, and X. Michaut. Understanding the relationship between gas and ice : experimental investigations on ortho-para ratios. In

- C. Stehlé, C. Joblin, and L. d'Hendecourt, editors, *EAS Publications Series*, volume 58, pages 307–314, Feb 2012. doi: 10.1051/eas/1258051.
- [27] Óscar Gálvez, Belén Maté, Víctor J. Herrero, and Rafael Escribano. Spectroscopic Effects in CH<sub>4</sub>/H<sub>2</sub>O Ices. , 703(2):2101–2107, October 2009. doi: 10.1088/0004-637X/703/2/2101.
- [28] A. Gaspar, M. Rieke, G. Rieke, J. Leisenring, M. Ygouf, C. Beichman, JWST NIRCам Group, and MIRI GTO Group. The JWST Debris Disk Spatially Resolved Imaging GTO Programs. In *American Astronomical Society Meeting Abstracts*, American Astronomical Society Meeting Abstracts, page 120.04, January 2020.
- [29] E. L. Gibb, D. C. B. Whittet, W. A. Schutte, A. C. A. Boogert, J. E. Chiar, P. Ehrenfreund, P. A. Gerakines, J. V. Keane, A. G. G. M. Tielens, E. F. van Dishoeck, and O. Kerkhof. An Inventory of Interstellar Ices toward the Embedded Protostar W33A. , 536(1):347–356, June 2000. doi: 10.1086/308940.
- [30] E. L. Gibb, D. C. B. Whittet, A. C. A. Boogert, and A. G. G. M. Tielens. Interstellar Ice: The Infrared Space Observatory Legacy. , 151(1):35–73, March 2004. doi: 10.1086/381182.
- [31] Thomas P. Greene, Douglas M. Kelly, John Stansberry, Jarron Leisenring, Eiichi Egami, Everett Schlawin, Laurie Chu, Klaus W. Hodapp, and Marcia Rieke.  $\lambda = 2.4$  to  $5 \mu\text{m}$  spectroscopy with the James Webb Space Telescope NIRCам instrument. *Journal of Astronomical Telescopes, Instruments, and Systems*, 3:035001, July 2017. doi: 10.1117/1.JATIS.3.3.035001.
- [32] S. Grieger, H. Friedrich, B. Asmussen, K. Guckelsberger, D. Nettleing, W. Press, and R. Scherm. Nuclear spin conversion of methane in pure and rare-gas mixed crystals. *Zeitschrift fur Physik B Condensed Matter*, 87(2):203–211, Jun 1992. doi: 10.1007/BF01315649.
- [33] William M. Grundy, Richard Binzel, Jason C. Cook, Dale P. Cruikshank, Cristina M. Dalle Ore, Alissa M. Earle, Kimberly Ennico, Donald Jennings, Carly Howett, Ralf-Ingo Kaiser, Ivan Linscott, A. W. Lunsford, Catherine B. Olkin, Alex Harrison Parker, Joel Wm. Parker, Sylvain Philippe, Silvia Protopapa, Eric Quirico, D. C. Reuter, Bernard Schmitt, Kelsi N. Singer, John R. Spencer, John A. Stansberry, S. Alan Stern, Constantine Tsang, Anne J. Verbiscer, Harold A. Weaver, G. E. Weigle, and Leslie Young. Pluto’s Nonvolatile Chemical Compounds. In *AAS/Division for Planetary Sciences Meeting Abstracts #48*, AAS/Division for Planetary Sciences Meeting Abstracts, page 306.07, October 2016.

- [34] Tatsuhiro I. Hasegawa, Eric Herbst, and Chun M. Leung. Models of Gas-Grain Chemistry in Dense Interstellar Clouds with Complex Organic Molecules. , 82:167, September 1992. doi: 10.1086/191713.
- [35] Jiao He, Kinsuk Acharyya, and Gianfranco Vidali. Sticking of Molecules on Nonporous Amorphous Water Ice. , 823(1):56, May 2016. doi: 10.3847/0004-637X/823/1/56.
- [36] Jiao He, Shahnewaj M. Emtiaz, and Gianfranco Vidali. Diffusion and Clustering of Carbon Dioxide on Non-porous Amorphous Solid Water. , 837(1):65, March 2017. doi: 10.3847/1538-4357/aa5f52.
- [37] Jiao He, SM Emtiaz, Adwin Boogert, and Gianfranco Vidali. The  $^{12}\text{CO}_2$  and  $^{13}\text{CO}_2$  Absorption Bands as Tracers of the Thermal History of Interstellar Icy Grain Mantles. *The Astrophysical Journal*, 869(1):41, Dec 2018. doi: 10.3847/1538-4357/aae9dc.
- [38] Jiao He, SM Emtiaz, Adwin Boogert, and Gianfranco Vidali. The  $^{12}\text{CO}_2$  and  $^{13}\text{CO}_2$  Absorption Bands as Tracers of the Thermal History of Interstellar Icy Grain Mantles. , 869(1):41, December 2018. doi: 10.3847/1538-4357/aae9dc.
- [39] Jiao He, SM Emtiaz, and Gianfranco Vidali. Measurements of Diffusion of Volatiles in Amorphous Solid Water: Application to Interstellar Medium Environments. , 863(2):156, August 2018. doi: 10.3847/1538-4357/aad227.
- [40] Jiao He, Aspen R. Clements, SM Emtiaz, Francis Toriello, Robin T. Garrod, and Gianfranco Vidali. The Effective Surface Area of Amorphous Solid Water Measured by the Infrared Absorption of Carbon Monoxide. , 878(2):94, June 2019. doi: 10.3847/1538-4357/ab1f6a.
- [41] Eric Herbst and Ewine F. van Dishoeck. Complex Organic Interstellar Molecules. , 47(1): 427–480, September 2009. doi: 10.1146/annurev-astro-082708-101654.
- [42] Robert Hodyss, Paul V. Johnson, Julie V. Stern, Jay D. Goguen, and Isik Kanik. Photochemistry of methane water ices. , 200(1):338–342, March 2009. doi: 10.1016/j.icarus.2008.10.024.
- [43] D. M. Hudgins, S. A. Sandford, L. J. Allamandola, and A. G. G. M. Tielens. Mid- and Far-Infrared Spectroscopy of Ices: Optical Constants and Integrated Absorbances. , 86:713, June 1993. doi: 10.1086/191796.
- [44] R. L. Hudson, P. A. Gerakines, and M. J. Loeffler. Activation of weak IR fundamentals of two species of astrochemical interest in the Tdpoint group - the importance of amorphous

- ices. *Physical Chemistry Chemical Physics (Incorporating Faraday Transactions)*, 17(19): 12545–12552, January 2015. doi: 10.1039/C5CP00975H.
- [45] Hubert M. James and Thomas A. Keenan. Theory of Phase Transitions in Solid Heavy Methane. *Journal of Chemical Physics*, 31(1):12–41, Jul 1959. doi: 10.1063/1.1730276.
- [46] Mindaugas Jonusas, Killian Leroux, and Lahouari Krim. N + H surface reaction under interstellar conditions: Does the NH/NH<sub>2</sub>/NH<sub>3</sub> distribution depend on N/H ratio? *Journal of Molecular Structure*, 1220:128736, November 2020. doi: 10.1016/j.molstruc.2020.128736.
- [47] Lora Jovanović, Thomas Gautier, Véronique Vuitton, Cédric Wolters, Jérémy Bourgalais, Arnaud Buch, François-Régis Orthous-Daunay, Ludovic Vettier, Laurene Flandinet, and Nathalie Carrasco. Chemical composition of Pluto aerosol analogues. , 346:113774, August 2020. doi: 10.1016/j.icarus.2020.113774.
- [48] Hideyo Kawakita, Jun-ichi Watanabe, Reiko Furusho, Tetsuharu Fuse, and Daniel C. Boice. Nuclear Spin Temperature and Deuterium-to-Hydrogen Ratio of Methane in Comet C/2001 Q4 (NEAT). *The Astrophysical Journal Letters*, 623(1):L49–L52, Apr 2005. doi: 10.1086/429872.
- [49] J. K. Kjems and G. Dolling. Crystal dynamics of nitrogen: The cubic  $\alpha$ -phase. , 11(4): 1639–1647, February 1975. doi: 10.1103/PhysRevB.11.1639.
- [50] H. M. Lee and B. T. Draine. Infrared extinction and polarization due to partially aligned spheroidal grains : models for the dust toward the BN object. , 290:211–228, March 1985. doi: 10.1086/162974.
- [51] Kathleen Mandt, Adrienn Luspay-Kuti, Kandis Lea Jessup, Vincent Hue, Josh Kammer, and Rachael Filwett. Nitrogen fractionation in the atmospheres of Pluto and Titan - implications for the origin of nitrogen in KBOs and comets. In *EGU General Assembly Conference Abstracts*, EGU General Assembly Conference Abstracts, page 5584, April 2017.
- [52] F. Merlin, M. A. Barucci, C. de Bergh, F. E. DeMeo, A. Alvarez-Candal, C. Dumas, and D. P. Cruikshank. Chemical and physical properties of the variegated Pluto and Charon surfaces. , 210(2):930–943, December 2010. doi: 10.1016/j.icarus.2010.07.028.
- [53] F. Merlin, E. Lellouch, E. Quirico, and B. Schmitt. Triton’s surface ices: Distribution, temperature and mixing state from VLT/SINFONI observations. , 314:274–293, November 2018. doi: 10.1016/j.icarus.2018.06.003.

- [54] R. S. Mikhal'Chenko, V. F. Getmanets, and V. T. Arkhipov. Peculiarities of heat transfer in porous solid nitrogen. *Journal of Engineering Physics*, 23(3):1075–1081, September 1972. doi: 10.1007/BF00832213.
- [55] M. Miki and T. Momose. Rovibrational transitions and nuclear spin conversion of methane in parahydrogen crystals. *Low Temperature Physics*, 26(9):661–668, Sep 2000. doi: 10.1063/1.1312392.
- [56] Yuki Miyamoto, Mizuho Fushitani, Daisuke Ando, and Takamasa Momose. Nuclear spin conversion of methane in solid parahydrogen. *Journal of Chemical Physics*, 128(11):114502–114502, Mar 2008. doi: 10.1063/1.2889002.
- [57] Barbara Louise Mojet, Sune Dalgaard Ebbesen, and Leon Lefferts. Light at the interface: the potential of attenuated total reflection infrared spectroscopy for understanding heterogeneous catalysis in water. *Chem. Soc. Rev.*, 39:4643–4655, 2010. doi: 10.1039/C0CS00014K. URL <http://dx.doi.org/10.1039/C0CS00014K>.
- [58] A. J. Nijman and A. John Berlinsky. Theory of Nuclear Spin Conversion in the  $\beta$  Phase of Solid Methane. , 38(8):408–411, Feb 1977. doi: 10.1103/PhysRevLett.38.408.
- [59] Karin I. Öberg, A. C. Adwin Boogert, Klaus M. Pontoppidan, Geoffrey A. Blake, Neal J. Evans, Fred Lahuis, and Ewine F. van Dishoeck. The c2d Spitzer Spectroscopic Survey of Ices around Low-Mass Young Stellar Objects. III. CH<sub>4</sub>. , 678(2):1032–1041, May 2008. doi: 10.1086/533432.
- [60] J. L. Ortiz, P. Santos-Sanz, B. Sicardy, G. Benedetti-Rossi, D. Bérard, N. Morales, R. Dufard, F. Braga-Ribas, U. Hopp, C. Ries, V. Nascimbeni, F. Marzari, V. Granata, A. Pál, C. Kiss, T. Pribulla, R. Komžík, K. Hornoch, P. Pravec, P. Bacci, M. Maestripietri, L. Nerli, L. Mazzei, M. Bachini, F. Martinelli, G. Succi, F. Ciabattari, H. Mikuz, A. Carbognani, B. Gaehrken, S. Mottola, S. Hellmich, F. L. Rommel, E. Fernández-Valenzuela, A. Campo Bagatin, S. Cikota, A. Cikota, J. Lecacheux, R. Vieira-Martins, J. I. B. Camargo, M. Assafin, F. Colas, R. Behrend, J. Desmars, E. Meza, A. Alvarez-Candal, W. Beisker, A. R. Gomes-Junior, B. E. Morgado, F. Roques, F. Vachier, J. Berthier, T. G. Mueller, J. M. Madiedo, O. Unsalan, E. Sonbas, N. Karaman, O. Erece, D. T. Koseoglu, T. Ozisik, S. Kalkan, Y. Guney, M. S. Niaei, O. Satir, C. Yesilyaprak, C. Puskullu, A. Kabas, O. Demircan, J. Alikakos, V. Charmandaris, G. Leto, J. Ohlert, J. M. Christille, R. Szakáts, A. Takácsné Farkas, E. Varga-Verebélyi, G. Marton, A. Marciniak, P. Bartczak, T. Santana-Ros,

- M. Butkiewicz-Bak, G. Dudziński, V. Alí-Lagoa, K. Gazeas, L. Tzouganatos, N. Paschalis, V. Tsamis, A. Sánchez-Lavega, S. Pérez-Hoyos, R. Hueso, J. C. Guirado, V. Peris, and R. Iglesias-Marzoa. The size, shape, density and ring of the dwarf planet Haumea from a stellar occultation. , 550(7675):219–223, October 2017. doi: 10.1038/nature24051.
- [61] Mikhail A. Ovchinnikov and Charles A. Wight. Inhomogeneous broadening of infrared and Raman spectral bands of amorphous and polycrystalline thin films. , 99(5):3374–3379, September 1993. doi: 10.1063/1.465147.
- [62] Richard J. Parker. The birth environment of planetary systems. *arXiv e-prints*, art. arXiv:2007.07890, July 2020.
- [63] C. M. Persson, A. O. H. Olofsson, R. Le Gal, E. S. Wirström, G. E. Hassel, E. Herbst, M. Olberg, A. Faure, P. Hily-Blant, J. H. Black, M. Gerin, D. Lis, and F. Wyrowski. Ortho-to-para ratio of  $\text{NH}_2$ . Herschel-HIFI observations of ortho- and para- $\text{NH}_2$  rotational transitions towards W31C, W49N, W51, and G34.3+0.1. , 586:A128, Feb 2016. doi: 10.1051/0004-6361/201526781.
- [64] Noemí Pinilla-Alonso, John Stansberry, and Bryan Holler. Surface properties of large TNOs: Expanding the study to longer wavelengths with the James Webb Space Telescope. *arXiv e-prints*, art. arXiv:1905.12320, May 2019.
- [65] Noemí Pinilla-Alonso, John A. Stansberry, and Bryan J. Holler. *Physical and Compositional Properties of Large TNOs: from Spitzer, to JWST*, pages 395–412. 2020. doi: 10.1016/B978-0-12-816490-7.00018-7.
- [66] E. Pisarska, P. Stachowiak, and A. Jeżowski. Observation of relaxation of molecular spins in  $\text{CH}_4$  and  $\text{CD}_4$  crystals in thermal conductivity experiment. *Low Temperature Physics*, 33(6): 587–589, Jun 2007. doi: 10.1063/1.2755190.
- [67] S. Protopapa, W. M. Grundy, D. C. Reuter, D. P. Hamilton, C. M. Dalle Ore, J. C. Cook, D. P. Cruikshank, B. Schmitt, S. Philippe, E. Quirico, R. P. Binzel, A. M. Earle, K. Ennico, C. J. A. Howett, A. W. Lunsford, C. B. Olkin, A. Parker, K. N. Singer, A. Stern, A. J. Verbiscer, H. A. Weaver, L. A. Young, and New Horizons Science Team. Pluto’s global surface composition through pixel-by-pixel Hapke modeling of New Horizons Ralph/LEISA data. , 287:218–228, May 2017. doi: 10.1016/j.icarus.2016.11.028.

- [68] Eric Quirico and Bernard Schmitt. Near-Infrared Spectroscopy of Simple Hydrocarbons and Carbon Oxides Diluted in Solid N<sub>2</sub> and as Pure Ices: Implications for Triton and Pluto. , 127(2):354–378, June 1997. doi: 10.1006/icar.1996.5663.
- [69] Eric Quirico, Sylvain Douté, Bernard Schmitt, Catherine de Bergh, Dale P. Cruikshank, Tobias C. Owen, Thomas R. Geballe, and Ted L. Roush. Composition, Physical State, and Distribution of Ices at the Surface of Triton. , 139(2):159–178, June 1999. doi: 10.1006/icar.1999.6111.
- [70] Carolyn D. Ruppel and John D. Kessler. The interaction of climate change and methane hydrates. *Reviews of Geophysics*, 55(1):126–168, Mar 2017. doi: 10.1002/2016RG000534.
- [71] E. L. Schaller and M. E. Brown. Volatile Loss and Retention on Kuiper Belt Objects. , 659(1):L61–L64, April 2007. doi: 10.1086/516709.
- [72] A. Schriver, L. Schriver-Mazzuoli, P. Ehrenfreund, and L. d’Hendecourt. One possible origin of ethanol in interstellar medium: Photochemistry of mixed CO<sub>2</sub>-C<sub>2</sub>H<sub>6</sub> films at 11 K. A FTIR study. *Chemical Physics*, 334(1-3):128–137, April 2007. doi: 10.1016/j.chemphys.2007.02.018.
- [73] P. L. Scott and C. D. Jeffries. Spin-Lattice Relaxation in Some Rare-Earth Salts at Helium Temperatures; Observation of the Phonon Bottleneck. *Physical Review*, 127(1):32–51, Jul 1962. doi: 10.1103/PhysRev.127.32.
- [74] R. Scott Smith, Tykhon Zubkov, and Bruce D. Kay. The effect of the incident collision energy on the phase and crystallization kinetics of vapor deposited water films. , 124(11):114710–114710, March 2006. doi: 10.1063/1.2177658.
- [75] Ruth Signorell. Verification of the vibrational exciton approach for CO<sub>2</sub> and N<sub>2</sub>O nanoparticles. , 118(6):2707–2715, February 2003. doi: 10.1063/1.1531622.
- [76] Ruth Signorell and Martin Jetzki. Vibrational exciton coupling in pure and composite sulfur dioxide aerosols. *Faraday Discussions*, 137:51, January 2008. doi: 10.1039/b700111h.
- [77] Ruth Signorell and Marc K. Kunzmann. Isotope effects on vibrational excitons in carbon dioxide particles. *Chemical Physics Letters*, 371(3):260–266, April 2003. doi: 10.1016/S0009-2614(03)00253-7.

- [78] Edward C. Sittler, John F. Cooper, Steven J. Sturmer, and Ashraf Ali. Titan's ionospheric chemistry, fullerenes, oxygen, galactic cosmic rays and the formation of exobiological molecules on and within its surfaces and lakes. , 344:113246, July 2020. doi: 10.1016/j.icarus.2019.03.023.
- [79] R. Scott Smith, Chunqing Yuan, Nikolay G. Petrik, Greg A. Kimmel, and Bruce D. Kay. Crystallization growth rates and front propagation in amorphous solid water films. , 150(21): 214703, June 2019. doi: 10.1063/1.5098481.
- [80] Takeru Sugimoto, Koichiro Yamakawa, and Ichiro Arakawa. Infrared spectroscopic investigation of nuclear spin conversion in solid CH<sub>4</sub>. *Journal of Chemical Physics*, 143(22): 224305, Dec 2015. doi: 10.1063/1.4936655.
- [81] Takeru Sugimoto, Ichiro Arakawa, and Koichiro Yamakawa. Nuclear spin relaxation of methane in solid xenon. *European Physical Journal D*, 72(3):42, Mar 2018. doi: 10.1140/epjd/e2017-80564-0.
- [82] Takeru Sugimoto, Hirokazu Nasu, Ichiro Arakawa, and Koichiro Yamakawa. Spectroscopic determination of interconversion rates among three nuclear spin isomers of methane in crystalline II. *Journal of Chemical Physics*, 150(18):184302, May 2019. doi: 10.1063/1.5091070.
- [83] Carine Manca Tanner and Martin Quack. Reinvestigation of the  $\nu_2 + 2\nu_3$  subband in the overtone icosad of <sup>12</sup>CH<sub>4</sub> using cavity ring-down (CRD) spectroscopy of a supersonic jet expansion. *Molecular Physics*, 110(17):2111–2135, Sep 2012. doi: 10.1080/00268976.2012.702934.
- [84] Matt W. Telfer, Eric J. R. Parteli, Jani Radebaugh, Ross A. Beyer, Tanguy Bertrand, François Forget, Francis Nimmo, Will M. Grundy, Jeffrey M. Moore, S. Alan Stern, John Spencer, Tod R. Lauer, Alissa M. Earle, Richard P. Binzel, Hal A. Weaver, Cathy B. Olkin, Leslie A. Young, Kimberly Ennico, Kirby Runyon, and aff12. Dunes on Pluto. *Science*, 360(6392): 992–997, Jun 2018. doi: 10.1126/science.aao2975.
- [85] A. G. G. M. Tielens and W. Hagen. Model calculations of the molecular composition of interstellar grain mantles. , 114(2):245–260, October 1982.
- [86] A. G. G. M. Tielens, A. T. Tokunaga, T. R. Geballe, and F. Baas. Interstellar Solid CO: Polar and Nonpolar Interstellar Ices. , 381:181, November 1991. doi: 10.1086/170640.

- [87] B. E. Turner. Detection of Doubly Deuterated Interstellar Formaldehyde (D<sub>2</sub>CO): an Indicator of Active Grain Surface Chemistry. , 362:L29, October 1990. doi: 10.1086/185840.
- [88] H. C. van de Hulst. The solid particles in interstellar space. *Recherches Astronomiques de l'Observatoire d'Utrecht*, 11:2.i–2, January 1946.
- [89] E. Vilenius, J. Stansberry, T. Müller, M. Mueller, C. Kiss, P. Santos-Sanz, M. Mommert, A. Pál, E. Lellouch, J. L. Ortiz, N. Peixinho, A. Thirouin, P. S. Lykawka, J. Horner, R. Dufard, S. Fornasier, and A. Delsanti. “TNOs are Cool”: A survey of the trans-Neptunian region. XIV. Size/albedo characterization of the Haumea family observed with Herschel and Spitzer. , 618:A136, October 2018. doi: 10.1051/0004-6361/201732564.
- [90] Tsunenobu Yamamoto, Yosuke Kataoka, and Kenkichi Okada. Theory of phase transitions in solid methanes. X. Centering around Phase II in solid CH<sub>4</sub>. *Journal of Chemical Physics*, 66(6):2701–2730, Mar 1977. doi: 10.1063/1.434218.
- [91] Leslie A. Young, Felipe Braga-Ribas, and Robert E. Johnson. *Volatiles evolution and atmospheres of Trans-Neptunian objects*, pages 127–151. 2020. doi: 10.1016/B978-0-12-816490-7.00006-0.
- [92] Chunqing Yuan, R. Scott Smith, and Bruce D. Kay. Surface and bulk crystallization of amorphous solid water films: Confirmation of “top-down” crystallization. *Surface Science*, 652:350–354, October 2016. doi: 10.1016/j.susc.2015.12.037.

**Shahnewaz M. Emtiaz****Personal details**

*Address* 1396 Alder Lake Ct., San Jose, CA 95131  
*Phone* (315) 925-8424  
*Mail* [shahnewaz.emtiaz@asml.com](mailto:shahnewaz.emtiaz@asml.com)

**Education**

**Syracuse University** **Aug 2014- Dec 2020**  
*Doctor of Philosophy in Physics*  
Advisor: Prof. Gianfranco Vidali.

**Dhaka University** **Mar 2009- Feb 2011**  
*Masters of Science in Physics*

**Dhaka University** **Apr 2004-Mar 2009**  
*Bachelor of Science in Physics*

**Employment**

**Sr. Design Engineer** **Oct 2020 - Present**  
*Advanced Semiconductor Material Limited (ASML)*

**Graduate Research Assistant** **Aug 2015 - July 2020**  
*Syracuse University, Advisor: Prof. Gianfranco Vidali*

**Graduate Teaching Assistant** **Aug 2014 - Aug 2015**  
*Syracuse University*

**Senior Officer** **Oct 2012 - July 2014**  
*Investment Corporation of Bangladesh*

Senior Officer

Dec 2011 - Sep 2012

Sonali Bank, Bangladesh

## Research Publications

**Shahnewaz M. Emtiaz**, F. Toriello, J. He, G. Vidali; "Infrared Spectroscopic Study of Solid methane: nuclear Spin Conversion of Stable and Metastable Phases". In: *J. Phys. Chem* 124.3 (2019), p. 552. DOI: 10.1021/acs.jpca.9b10643.

Jiao He, Aspen R Clements, **SM Emtiaz**, Francis Toriello, Robin T Garrod, Gianfranco Vidali; "The Effective Surface Area of Amorphous Solid Water Measured by the Infrared Absorption of Carbon Monoxide". In: *Astrophys J.* 124.3 (2019), p. 94. DOI: 10.3847/1538-4357/ab1f6a.

Jiao He, **SM Emtiaz**, and Gianfranco Vidali; "Measurements of Diffusion of Volatiles in Amorphous Solid Water: Application to Interstellar Medium Environments". In: *Astrophys J.* 863.2 (2018), p. 156. DOI: 10.3847/1538-4357/aad227.

Jiao He, **SM Emtiaz**, Adwin Boogert, Gianfranco Vidali; "The  $^{12}\text{CO}_2$  and  $^{13}\text{CO}_2$  Absorption Bands as Tracers of the Thermal History of Interstellar Icy Grain Mantles". In: *Astrophys J.* 869.1 (2018), p. 41. DOI: 10.3847/1538-4357/aae9dc.

Jiao He, **SM Emtiaz**, Adwin Boogert, Gianfranco Vidali; "Diffusion and Clustering of Carbon Dioxide on Non-porous Amorphous Solid Water". In: *Astrophys J.* 837.1 (2018), p. 65. DOI: 10.3847/1538-4357/aa5f52.

Jiao He, **Shahnewaj M. Emtiaz**, and Gianfranco Vidali; "Mechanism of Atomic Hydrogen Addition Reactions on np-ASW". In: *Astrophys J.* 851.2 (2017), p. 104. DOI: 10.3847/1538-4357/aa5f52.